AFGL-TR-88-0135

AD-A208 525

Modeling Regional Seismic Waves From Underground Nuclear Explosion

Robert W. Clayton
David G. Harkrider
Donald V. Helmberger

California Institute of Technology
Seismological Laboratory
Pasadena, CA 91125

9 May 1988

Scientific Report No. 1

APPROVED FOR PUBLIC RELEASE; DISTRIBUTION UNLIMITED

DTIC
ELECTE
JUN 06 1989
S D
H

AIR FORCE GEOPHYSICS LABORATORY
AIR FORCE SYSTEMS COMMAND
UNITED STATES AIR FORCE
HANSCOM AIR FORCE BASE, MASSACHUSETTS 01731-5000

89 6 05 174

Name of Contractor:	California Inst of Technology
Effective Date of Contract:	14 March 1987
Contract Expiration Date:	31 March 1988
Contract Number:	F19628-87-K-0028
Principal Investigators:	Robert W. Clayton (818-356-6909) David G. Harkrider(818-356-6910) Donald V. Helmberger(818-356-6998)
Program Manager:	James Lewkowicz (617-377-3028)
Short Title of Work:	Modeling Regional Seismic Waves From Underground Nuclear Explosions

The views and conclusions contained in this document are those of the authors and should not be interpreted as necessarily representing the official policies, either expressed or implied, of the Defense Advanced Research Projects Agency of the US Government.

Sponsored by: Defense Advanced Research Projects Agency
Defense Sciences Office
Geophysical Sciences Division
DARPA/DSO Physical Characterization of Seismic Sources

"This technical report has been reviewed and is approved for publication."

JAMES F. LEWKOWICZ
Contract Manager

HENRY A. OSSING
Chief, Solid Earth Geophysics Branch

FOR THE COMMANDER

DONALD H. ECKHARDT
Director
Earth Sciences Division

This report has been reviewed by the ESD Public Affairs Office (PA) and is releasable to the National Technical Information Service (NTIS).

Qualified requestors may obtain additional copies from the Defense Technical Information Center. All others should apply to the National Technical Information Service.

If your address has changed, or if you wish to be removed from the mailing list, or if the addressee is no longer employed by your organization, please notify AFGL/DAA, Hanscom AFB, MA 01731. This will assist us in maintaining a current mailing list.

Do not return copies of this report unless contractual obligations or notices on a specific document requires that it be returned.

Unclassified

SECURITY CLASSIFICATION OF THIS PAGE

REPORT DOCUMENTATION PAGE

1a. REPORT SECURITY CLASSIFICATION: UNCLASSIFIED	1b. RESTRICTIVE MARKINGS
2a. SECURITY CLASSIFICATION AUTHORITY	3. DISTRIBUTION/AVAILABILITY OF REPORT: Approved for public release; distribution unlimited
2b. DECLASSIFICATION/DOWNGRADING SCHEDULE	
4. PERFORMING ORGANIZATION REPORT NUMBER(S)	5. MONITORING ORGANIZATION REPORT NUMBER(S): AFGL-TR-88-0135
6a. NAME OF PERFORMING ORGANIZATION: California Institute of Tech. Seismological Laboratory; 6b. OFFICE SYMBOL (If applicable)	7a. NAME OF MONITORING ORGANIZATION: Air Force Geophysics Laboratory
6c. ADDRESS (City, State and ZIP Code): Pasadena, California 91125	7b. ADDRESS (City, State and ZIP Code): Hanscom Air Force Base, Massachusetts 01731
8a. NAME OF FUNDING/SPONSORING ORGANIZATION: Advanced Research Projects Agency (DOD); 8b. OFFICE SYMBOL (If applicable)	9. PROCUREMENT INSTRUMENT IDENTIFICATION NUMBER: F19628-87-K-0028
8c. ADDRESS (City, State and ZIP Code): 1400 Wilson Boulevard, Arlington, Virginia 22209	10. SOURCE OF FUNDING NOS.

PROGRAM ELEMENT NO.	PROJECT NO.	TASK NO.	WORK UNIT NO.
61101E	7A10	DA	CA

11. TITLE (Include Security Classification): Modeling Regional Seismic Waves From Underground Nuclear Explosion

12. PERSONAL AUTHOR(S): Robert W. Clayton, David G. Harkrider and Donald V. Helmberger

13a. TYPE OF REPORT	13b. TIME COVERED	14. DATE OF REPORT (Yr., Mo., Day)	15. PAGE COUN
SCIENTIFIC NO. 1	FROM 3/17/87 TO 3/31/88	5/9/1988	94

16 SUPPLEMENTARY NOTATION

17. COSATI CODES		
FIELD	GROUP	SUB. GR.

18. SUBJECT TERMS (Continue on reverse if necessary and identify by block number): SH Lg propagation near and in continued margins; regional Love waves, source phenomena versus path effects

19. ABSTRACT (Continue on reverse if necessary and identify by block number)

The research performed under the contract, during the period 17 March 1987 through 31 March 1988, can be divided into two main topics; the effects of ocean continent transition zones on $L - g$ waves, and modeling regional Love waves with 2-D velocity structures.

In section II, we produced hybrid regional and teleseismic SH mode sum seismograms after propagation through a regional transition zone or other heterogeneity that exists as part of a longer, mostly plane-layered, path. In particular the effects of ocean continent transition regions of varying lengths on the propagation of Lg waves are examined. The total attenuation of Lg due to geometry for propagation along a partially oceanic path is at most a factor of four. Extending the oceanic path length changes this factor to at most 6. This is inadequate to explain the observed attenuation of Lg. Thus, additional effects, must be considered to provide a complete explanation of the attenuation of Lg.

20. DISTRIBUTION/AVAILABILITY OF ABSTRACT	21. ABSTRACT SECURITY CLASSIFICATION
☐ CLASSIFIED/UNLIMITED ☐ SAME AS RPT. ☐ DTIC USERS ☐	UNCLASSIFIED

22a. NAME OF RESPONSIBLE INDIVIDUAL	22b. TELEPHONE NUMBER (Include Area Code)	22c. OFFICE SYMBOL
James Lewkowicz	(617)377-3028	AFGL/LWH

DD FORM 1473, 83 APR EDITION OF 1 JAN 73 IS OBSOLETE.

UNCLASSIFIED

SECURITY CLASSIFICATION OF THIS PAGE

In section III, long period seismograms recorded at Pasadena of earthquakes occurring along a profile to Imperial Valley are studied in terms of source phenomena versus path effects. Some of the events have known source parameters, determined by teleseismic or near-field studies, and are used as master events in a forward modeling exercise to derive the Green's functions that describe the propagation effects along the profile. Both timing and waveforms of records are matched by synthetics calculated from 2-dimensional velocity models. The best 2-dimensional section begins at Imperial Valley with a thin crust containing the basin structure and thickens towards Pasadena. The detailed nature of the transition zone at the base of the crust controls the early arriving shorter periods while the edge of the basin controls the scattered longer period surface waves. Shallow events in the basin are easily distinguished from deep events as well as the amount of strike-slip versus dip-slip motions involved from the waveform characteristics alone. Those events rupturing the sediments, such as the 1979 Imperial Valley earthquake, can be recognized easily by a late arriving scattered Love wave which has been delayed by the very slow path across the shallow structure.

TABLE OF CONTENTS

Summary V

Numerical modeling of SH L_g waves in and near continental margins 1

Modeling regional Love waves: Imperial Valley to Pasadena 49

DTIC COPY INSPECTED 6

Accession For
NTIS GRA&I ☑
DTIC TAB ☐
Unannounced ☐
Justification
By
Distribution/
Availability Codes
Dist | Avail and/or Special
A-1

Summary

The research performed under the contract, during the period 17 March 1987 through 31 March 1988, can be divided into two main topics; the effects of ocean continent transition zones on $L - g$ waves, and modeling regional Love waves with 2-D velocity structures.

In section II, we produced hybrid regional and teleseismic SH mode sum seismograms after propagation through a regional transition zone or other heterogeneity that exists as part of a longer, mostly plane-layered, path. In particular the effects of ocean continent transition regions of varying lengths on the propagation of Lg waves are examined. The total attenuation of Lg due to geometry for propagation along a partially oceanic path is at most a factor of four. Extending the oceanic path length changes this factor to at most 6. This is inadequate to explain the observed attenuation of Lg. Thus, additional effects, must be considered to provide a complete explanation of the attenuation of Lg.

In section III, long period seismograms recorded at Pasadena of earthquakes occurring along a profile to Imperial Valley are studied in terms of source phenomena versus path effects. Some of the events have known source parameters, determined by teleseismic or near-field studies, and are used as master events in a forward modeling exercise to derive the Green's functions that describe the propagation effects along the profile. Both timing and waveforms of records are matched by synthetics calculated from 2-dimensional velocity models. The best 2-dimensional section begins at Imperial Valley with a thin crust containing the basin structure and thickens towards Pasadena. The detailed nature of the transition zone at the base of the crust controls the early arriving shorter periods while the edge of the basin controls the scattered longer period surface waves. Shallow events in the basin are easily distinguished from deep events as well as the amount of strike-slip versus dip-slip motions involved from the waveform characteristics alone. Those events rupturing the sediments, such as the 1979 Imperial Valley earthquake, can be recognized easily by a late arriving scattered Love wave which has been delayed by the very slow path across the shallow structure.

NUMERICAL MODELLING OF SH L_G WAVES IN AND NEAR CONTINENTAL MARGINS

Janice Regan and David G. Harkrider

Summary

The effect of transition regions between continental and oceanic structures on the propagation of L_g waves from continental sources is examined. In particular, the attenuation due to variations in layer thickness in such transition regions is calculated and explained for a suite of simple models. The measured attenuation along partially oceanic paths beginning and ending in a continental structure is at most a factor of four. This is inadequate to explain the observed extinction of L_g along such paths.

The method used to calculate the results presented in this study is developed and its validity and accuracy are demonstrated. Propagator matrix seismograms are coupled into a Finite Element calculation to produce hybrid teleseismic SH mode sum seismograms. These hybrid synthetics can be determined for paths including any regional transition zone or other heterogeneity that exists as part of a longer, mostly plane-layered, path.

Numerical results presented for a suite of continent ocean and ocean continent transition models show several trends. Passage through a continent ocean transition, increases the amplitude and coda length of the L_g wave at the surface, and allows much of the modal L_g energy trapped in the crust to escape into the subcrustal layers as body waves. The magnitude of both these effects increases as the length of the transition region increases. When the wavefront passes through the oceanic structure following the continent to ocean transition region further energy escapes from the crustal layer, and produces a decrease in L_g amplitude at the surface. The rate of amplitude decrease is maximum near the transition region and decreases with distance from it. Passage through an ocean continent transition region causes a rapid decrease in the L_g amplitude at the surface of the crust. The energy previously trapped in the oceanic crustal layer spreads throughout the thickening crustal layer. The body wave phases which are incident on the continental crust in the ocean continent transition region are predominantly transmitted back into the crust. The other body wave phases reach depths below the depth of the base of the continental crust before reaching the ocean continent transition and thus, escape from the system.

Introduction

This paper presents a study of the propagation of L_g waves across ocean continent transition regions. The transition regions are represented by simplified models each consisting of a crustal layer with a smoothly varying thickness above a half-space. The changes to a L_g

wavefield, as it travels across such a transition region, are modelled using a hybrid method which combines the FE method and the Propagator Matrix technique (PM) (Harkrider, 1964, 1970, 1981) PM seismograms for L_g waves from a continental source are coupled into a FE calculation which propagates the L_g wavefield across the continent ocean boundary. Results from the Finite Element (FE) calculation are then coupled into a second FE calculation which propagates the L_g wavefield through an ocean to continent transition region. The results of either FE calculation may be propagated through a region of horizontally uniform waveguide by coupling them back into a PM calculation using the Seismic Representation Theorem (RT) (de Hoop, 1958). The FE to PM coupling can be used to economically investigate the effects of long ocean path lengths between regions and is the subject of later papers. Here we restrict ourselves to regions in and near transition zones separated by short ($\leq 150km$) ocean paths.

In remainder of this introduction the importance of this work to major areas of study such as tectonic mapping and nuclear discrimination will be explained, the modal interpretation of L_g on which the calculation of synthetic seismograms is based will be justified, and the new results this method will make possible will be discussed and related to previous work.

One of the important types of observational studies of L_g has been to distinguish regions with oceanic crustal structures from those with continental crustal structures. Press and Ewing (1952) and Bath (1954) observed extinction of L_g when the propagation path included an oceanic portion of length greater than 200 km, and high attenuation or extinction when the oceanic path length was as short as 100 km. This lead to the commonly used approach of defining paths which pass under oceans but do not attenuate L_g as continental. The results of the present paper seriously challenge the interpretation that paths with short oceanic portions which show little or no L_g attenuation are necessarily continental. They may necessitate the reassessment of some of the results of studies of L_g in many regions of the world. (Press *et al.*, 1956; Press, 1956; Savarensky and Valdner, 1960; Bolt, 1957; Lehmann, 1952, 1957; Oliver *et al.*, 1955; Herrin and Minton, 1960; Wetmiller, 1974; Gregersen, 1984; Kennett and Mykkeltveit, 1984)

Another major use of L_g waves is the determination of magnitudes, m_{bL_g}, of explosions and earthquakes. Different types of magnitudes, including m_{bL_g}, are compared to discriminate between the two types of sources (Blandford, 1982; Pomeroy et al., 1982). γ, the coefficient of anelastic attenuation, which is derived from L_g wave amplitudes, is important in studies of m_{bL_g} and can be employed to assess the possible destructiveness of earthquakes. It is

important to understand if reflections, refractions, or diffractions from changes in crustal thickness , generally ignored in studies measuring m_{bL_g} or γ will produce significant effects not accounted for in the interpretations given (Nuttli 1973, 1978, 1981; Herrmann and Nuttli, 1982, 1975; Street, 1976, 1984; Street et al., 1975; Street and Turcotte, 1977; Jones et al., 1977; Bollinger, 1979; Barker et al., 1981; Nicolas et al., 1982; Dwyer et al., 1983; Chung and Bernreuter, 1981; Singh and Herrmann, 1983; Campillo et al., 1984; Herrmann and Kijko, 1983).

The wavefields transmitted through the transition region models are calculated to model L_g. The preferred interpretation of L_g is in terms of a superposition of higher mode surface waves. The higher mode surface wave interpretation was initially unpopular because, in its earliest forms, based on fundamental mode Love waves alone, it did not explain the vertical and longitudinal components and the long coda. However, it subsequently superceded the alternate explanation in terms of channel waves trapped in the crust above a low velocity layer for the following reasons. Oliver and Ewing (1957, 1958), Oliver *et al.* (1959), and Kovach and Anderson (1964) showed that all components of L_g could be interpreted by considering both higher mode Rayleigh and Love waves. Knopoff *et al.* (1975), and Panza and Calcagnile (1974, 1975), Bouchon (1981, 1982) used the higher mode interpretation of L_g to calculate synthetic seismograms without including a low velocity channel below the crustal waveguide. Other phases previously defined in terms of the channel model have been successfully modelled using the higher mode surface wave model. Schwab *et al.* (1974), and Mantovani *et al.* (1977), considered S_n, Panza and Calcagnile (1975) considered R_g and L_g, and Stephens and Isacks (1977) considered the transverse component of S_n. Clearly, the multimode surface wave explanation of L_g is valid and useful. However, the long L_g coda observed is still not completely understood for phase velocities less than 2.8 km/sec. The attribution of this long coda to diffraction and reflection from crustal structure is supported by the results presented in this study.

A simple parallel of the multimode surface wave interpretation, which is a very useful aid in the interpretation of the wavefields presented in this study, is the representation of the multimode L_g arrivals as superpostions of multiply reflected post-critical SH and SV rays trapped in the crustal layer. Bouchon (1982) used this type of interpretation for L_g arrivals for group velocities between 3.5 and 2.8 km/sec. Pec (1967) and Kennett (1986) also used the ray approach to address properties of L_g. This type of interpretation can also be used to explain where structure causes conversions from L_g to distinct body waves or from

one SH mode to another. Gregersen (1978) discusses conversion between different modes of Love waves and between Love and Rayleigh waves at an ocean continent boundaries. Understanding conversion between modes of L_g and between L_g and other phases is an important part of understanding the mechanisms of attenuation of L_g along mixed paths.

Many attempts to understand the propagation of seismic disturbances across regions of varying structure such as transition zones have been made. First, simple models were used and analytic solutions were derived for soluble special cases, then increasingly complicated models were considered as available computational power increased. The types of models that have been used to approximate transition regions can be separated into several types which are illustrated in Figure 1. Sato (1961a) derives analytic results for models of type 1a (Figure 1a) with L=0 and L>0. Kennett (1973) has considered the problem of seismic waves interacting with a layer or layers in which properties change across a surface perpendicular to or at a specified angle from the layering. Several types of solutions for models of type 1b (Figure 1b) have been derived. Sato (1961b) obtained approximate analytic reflection and transmission coefficients, for $h << \lambda$, the incident wavelength. Hudson and Knopoff (1964), Knopoff and Hudson (1964), Hudson (1977), and Bose (1975) derived similar solutions without applying the $h << \lambda$ constraint. Alsop (1966) developed an approximate solution for these coefficients applicable when all energy remains in Love waves. Gregersen and Alsop (1974, 1976) extended this method to the case of non-normally incident Love waves. They found that for oblique incidence at angles less than forty degrees normal incidence is a good approximation. Kazi (1978a, 1978b) derives solutions that account for and demonstrate the importance of the Love waves converted to scattered body waves at the surface step. Martel (1980) used a FE technique and spatial filtering to isolate the diffracted body wave component. Many workers have studied models of type 1c (Figure 1c). Knopoff and Mal (1967), and Knopoff *et al.* (1970) derived an analytic solution usable when the slope of the surface (or Moho) in the transition region is small. Pec (1967) calculated the dispersion of Love waves propagating in a wedge shaped layer and found that the largest changes in phase velocity and amplitudes at short periods. Boore(1970) studied the propagation of a simple Love wave ($T > 20sec$), modelled as a Ricker wavelet, using the Finite Difference (FD) method. He noted that in the region of the transition that mode conversions and conversion to other types of waves seemed to be important. Lysmer and Drake (1971, 1972) and Drake (1972) use a FE method based on Zienkiewicz and Cheung (1967). This formulation requires that the incident modal energy is exactly equal to the sum of the reflected and transmitted

modal energy. The body waves present in the system produce distortions to the elastic layer over a half-space eigenfunctions, which increase for higher modes. Drake and Bolt (1980) used the same method with a model of type 1d (Figure 1d) to study a more realistic model fitting fundamental mode phase velocity data for events normally incident on the California continental margin at periods between 4.4 and 60 seconds.

All the studies discussed in the previous paragraph used periods much longer than those that will be considered in the following discussions. The shorter periods used in this study allow the examination of the effects of transition regions with L many times λ. The energy escaping from the crustal waveguide is shown in this study to be an important component of the explanation of the attenuation of the L_g phase travelling on partially oceanic paths. Previous studies considered mainly fundamental mode Love wave input sampled at a selection of discrete frequencies, while the forcing functions used in this study are a sum over a range of frequencies on the fundamental and first five higher branches. Of the previous studies, only Kennett and Mykkeltveit (1984) have generated realistic seismograms similar to those used in this study, instead other studies concentrated on measuring phase velocities and transmission and reflection coefficients.

Propagator to Finite Element Coupling

Within a layered medium the "trapped" wavefield can be mathematically constructed at any point receiver using the PM technique and an appropriate form of a source representation. The resulting far-field seismogram will include not only a direct arrival but also the superposition of many multiple critical and post-critical reflections which produce the surface waves in the wavetrain. To simplify the graphical representation of the hybrid method, shown in Figure 2, each such seismogram is represented by a single solid line from the source to the receiver. Coupling a wavefield defined by the discrete sampling of such seismograms, along the leftmost edge of a FE grid, into that FE grid is straightforward. The seismograms, for a specified source function, are generated at a group of receivers equally spaced in z located a horizontal distance, X, from the source. The depth spacing between the receivers is the node spacing in the FE grid into which the wavefield is to be coupled. These seismograms are applied as displacement time history constraints on the leftmost column of nodes in the FE grid, thus, completely specifying the subsequent motion at all points in that FE grid.

The seismograms used as forcing functions can be generated using more than one type of source. For a line source, in a homogeneous half-space or a layered half-space the applied

forcing functions are $u_y(x,y,z)$. For a double couple point source the PM solutions can be expressed in a simple form when only variations in the r coordinate are being discussed. This form is

$$\{\overline{v}(r,\phi,z)\} = \overline{v}_\nu(\phi,z)\frac{\partial H_\nu^{(2)}(k_L r)}{\partial r}$$

where $\nu = 2$ for a strike slip source and $\nu = 1$ for dip-slip. The displacements are expressed in cylindrical coordinates rather than in the Cartesian coordinates appropriate to the RT integral or the Cartesian FE representation. When these displacement seismograms are used as input forcing functions then they are assumed to be in Cartesian coordinates ($\overline{u}_y(x,y,z)$). The following discussion explains why the hybrid seismograms produced using the cylindrical forcing functions to approximate the desired cartesian forcing functions approximate the cylindrical solution $\{\overline{v}(r,\phi,z)\}$ at the receiver.

Consider a FE grid with its leftmost edge a distance $X = r_1$ from a source, and a receiver, where hybrid and analytic synthetic results are recorded, a distance $X2 = r_2$ from the source. Define the distance propagated within the FE grid as $\Delta r = r_2 - r_1$. Since we are considering the case of r large, $k_L >> \frac{\nu}{r}$ $\{\overline{v}(r_2,\phi,z)\}$ can be expressed in terms of ϕ, z, r_1, and Δr as

$$\{\overline{v}(r_2,\phi,z)\} = \{\overline{v}(r_1,\phi,z)\}\sqrt{\frac{r_1+\Delta r}{r_1}}\,e^{-ik_L\Delta r}$$

$$\approx \{\overline{v}(r_1,\phi,z)\}\,e^{-ik_L\Delta r} \quad \Delta r << r_1 \quad k_L r_1 >> 1$$

Now, for a line source the analogous modal continuation relation is,

$$u_\phi(x_2,z) = u_\phi(x_1,z)\,e^{-ik_L(x_2-x_1)} = u_\phi(x_1,z)\,e^{-ik_L\Delta x}$$

Comparing, we see that both expressions have the same form. In each case the displacement at r_2 can be expressed as the displacement at r_1 multiplied by a propagation factor. A 2-D FE or RT calculation will give the same propagation factor for each mode as the analytic expression above. If the displacements at r_1, $v(r_1,\phi,z)$ or $u_y(x,z)$, and the propagation factors, $e^{-ik_L\Delta r}$ or $e^{-ik_L\Delta x}$, are correlated by considering $x_1 = r_1$ and $\Delta x = \Delta r$, then $\overline{v}(r_2,\phi,z)$, the 3-D solution, will be given by $u_y(x_2,z)$, the result of the 2-D FE or RT calculation. The source

must be many λ's, $k_L r$, from the boundary and r must be normal to the FE grid edge and in the plane of the FE grid.

The PM seismograms $\{\bar{v}(r,\phi,z)\}$ used as forcing functions in the tests discussed below show the overall character of the arrivals seen in data in the L_g group velocity range of between 2.8 and 3.5 km/sec (Figure 3). The seismograms are complete to a period of 1.9 sec and contain most of the energy for periods down to 0.5 sec. The heavy rectangle in Figure 3 labeled input window delimits the time window used to select the portions of the seismograms used as displacement time history forcing functions. The forcing functions used in subsequent calculations differ from the seismogram shown in Figure 3 in that no instrument has been applied. The instrument is applied to the FE result.

Designing FE Grids

A study of the effects of the length of simple transition regions on the attenuation of SH type L_g mode sum seismograms passing through them has yielded some interesting results. The two classes of transition models considered are illustrated in Figure 4. Calculations were performed for four individual models from each class, for a continental reference model, and for an oceanic reference model. The difference between individual transition models was L, the length of the transition region. Real ocean to continent type transitions occur over lengths of 50 to 300 km (Keen and Hyndman, 1979; Hinz *et al.*, 1979; Eittreim and Grantz, 1979; Le Douaran *et al.*, 1984). However, an upper limit on L of 100 km was imposed by computation limits. Thus, the lengths used for this investigation were a step transition (0 km), 25, 50, and 100 km. In order to discuss the results of the FE calculations using these models one must first describe the models. Also, the methods used to obtain and display the results of the calculations using those models must be considered.

The first class of models are used to describe continent to ocean transition regions. In further discussions these models will be referred to as C/O models, and the transitions they represent as C/O transitions. Similarly, the second class of models, used to describe ocean to continent transition regions, will be referred to as O/C models and the transitions they represent as O/C transitions. The continental reference model consists of a 32 km thick crustal layer over a half-space. The oceanic reference model consists of two 5 km layers, one water and one crust, over a half-space. Each C/O or O/C transition region is characterized by a continuous rate of thinning or thickening of the crustal layer. In all models the crustal layer has a SH wave velocity, of 3.5 km/sec and a density of 2.7 g/cc, while the half-space has an SH wave velocity of 4.5 km/sec and a density of 3.4 g/cc. Each class of transition models

has the same BC's applied to each of its members. The forcing functions used to drive the C/O transition and continental reference FE calculations are a vertical section of sixty mode sum seismograms, calculated at depth intervals of 0.5 km beginning at the surface, for a strike slip source at 8 km depth at a distance X = 1500 km. The forcing functions for the O/C transition and oceanic reference tests are recorded during the 50 km C/O transition calculation. They consist of a depth section of hybrid seismograms recorded 25 km past the oceanic end of the 50 km C/O transition region, 1755 km from the source. The vertical spacing within the depth section is 0.5 km. All other BC's are identical for all models. The transmitting BC is applied to all edge nodes of the grid, excluding only the free surface and the nodes to which forcing functions are applied.

The first step in designing a grid for FE calculations is to determine grid spacing, dx, and the time step duration, dt. It is important to maximize dx and dt. At least six nodes per wavelength are needed to avoid numerical dispersion problems. To maintain numerical stability, the wavefront can travel no more that half the grid spacing per time step. Thus, dx and dt must be chosen to satisfy

$$dx \leq \frac{V_{min}}{6f} \qquad dt \leq \frac{dx}{2V_{max}}$$

where f is the highest frequency in the waveform to be modelled and V_{min} and V_{max} are the minimum and maximum S velocities respectively in the dominant part of the model. In this study, we are considering L_g waves with a predominant period of approximately 1 sec. in a medium with V_{min} = 3.5 km/s and V_{max} = 4.5 km/s. Thus, we have chosen dx=.5 km and dt=.05 sec.

The next step in designing the grid is determining the dimensions of the grid, nx and ny, the duration of the input forcing functions, T_{mi}, the duration of the calculated time series, T_{mcalc}, and the location of the transition region within the grid. The location of the transition region within the grid is defined in terms of the distances from the leftmost grid edge to positions A, B, C, D, E, in Figure 4. The values of these parameters were chosen to satisfy two criteria.

(A) a seismogram of duration D_s seconds can be recorded at A (Figure 4) before the multiple reflection of the input wave from the beginning of the transition, B, to the leftmost grid boundary and back again reaches A.

(B) a seismogram uncontaminated by the multiple reflection with duration D_s seconds can be recorded at the receiver closest to the rightmost edge of the grid. This receiver is defined to be at a distance x_f from the leftmost grid edge.

Criteria A and B concern themselves only with reflections from the leftmost edge of the grid. Nonphysical reflections from the bottom and the rightmost edge of the grid are removed using transparent BC's which will be discussed later. The duration D_s was chosen to be 55 seconds, the observed coda length for a SH L_g mode sum seismogram at a distance of 1000 km from the source. For all the models used in this study the values of parameters defining the size of the grid and the location of the transition region within it are given in table 1. Distances are given as the number of nodes in the horizontal direction from the left edge of the grid to the depth section or boundary indicated. The model names indicate L, then the model type (f=C/O, r=O/C, ref=reference).

Sampling FE Solutions

Analysis of the effects of various transitions on the waveforms and amplitudes of L_g waves using FE techniques requires that the motions of the nodes of the FE grid be sampled so that the progress of the L_g waves across the transition can be observed. Two methods of sampling are used in this study. Complete displacement time histories are recorded for selected nodes, and the displacements of all nodes in the grid are recorded at given time intervals. The first approach produces seismograms which can be used to illustrate variations of amplitude and waveform with distance or depth, the second approach produces time slices and is a clear way to illustrate the propagation and distortion of wavefronts caused by passage through the inhomogeneous structure.

For each model time slices were recorded every 250 or 400 time steps. Displacements are graphically represented by symbols plotted at an array of points depicting the nodes in the FE grid. The size of the symbol plotted at the node is increased as the absolute value of the displacement increases, producing darker areas where larger displacements are occurring. Each of the time slices is self scaled, that is the largest value of the absolute value of amplitude in the grid is set to the largest symbol size. At all other nodes the ratio of the nodal amplitude to the maximum amplitude is used as a factor to scale the symbol size. A minimum amplitude cutoff is defined below which no symbol is plotted. For the time slices displayed in this paper the cutoff is 2% of the maximum amplitude. Thus, the smallest symbols cover a range of amplitudes between 1% and 10% of the maximum amplitude. The self scaling of the time slices means that successive time slices may show the same absolute

amplitude as a different symbol size. Thus, the same region of the waveform will appear darker on a time slice with a given maximum amplitude than on another time slice with a larger maximum amplitude. This difference must be remembered when interpreting the time slices.

For each model one surface section and several depth sections of seismograms were recorded. Each surface section contains seimograms recorded at intervals of 5 km along the solid surface. Each depth section contains a set of seismograms recorded in the same column of the FE grid, starting in the upper row of the grid and equally spaced in depth below it. Depth sections with a vertical spacing of 2.5 km, were recorded at distances including those corresponding to positions A through E (Figure 4) for each model. For the each reference model, depth sections were recorded at the distances, X2, used for each corresponding transition model.

The amplitude of the first large positive and negative peaks in L_g mode sum seismograms (figure 3) are extremely sensitive to distance from the source, and to the time spacing and starting time chosen when calculating the synthetics. It is not unusual for very small changes in these parameters to produces variations in amplitude of several percent . An improved filtering technique would reduce the variation slightly by removing more of the sampling effects due to the non-zero spectral amplitude at the nyquist frequency. However, a significant portion of the variation is apparently due to changes in the patterns of interference between multiple arrivals. In addition, the direct S pulse and the end of the S_n wavetrain arrive at the same time as the initial pulses in the L_g wavetrain. The longer period portions of the S and S_n arrivals have been removed by the band pass filter. However, some non L_g energy will be present in the first few cycles of the trace. Unfortunately, the initial high frequency peaks, which are effected by the problems discussed above, yield the maximum peak to peak amplitude. This indicates that peak to peak amplitude will be a poor measure of the L_g amplitude. A more stable measure of amplitude correspondence between seismograms of this type is the RMS amplitude calculated over some time window appropriate to the seismograms being compared.

$$RMS = \sqrt{\frac{\sum_{n=1}^{m} [amp(n)^2]}{m}} \qquad m = \frac{T_{RMS}}{\Delta t}$$

where m is the number of points in a sampling window of duration T_{RMS} seconds. Such an RMS amplitude measure will reduce the effects of S or S_n contamination and of any other instabilities effecting the initial arrivals.

The evaluation of RMS amplitudes is straightforward once the sampling window has been chosen. The location of the sampling window with respect to the arrivals of maximum amplitude, and the duration of the trace contained within the sampling window, have a significant effect on the value of the RMS amplitude. Care must be taken to choose windows for two sets of results that produce meaningful comparisons. When results of two separate FE calculations are being compared, at corresponding nodes, both seismograms begin at the same absolute time. When successive seismograms in a depth or distance section, from a single calculation, are being compared, the duration of the sampled portion of the trace with negligible amplitude that occurs before the first arrival must be constant. A general approach which does not require the use of theoretical travel times was chosen to determine windows in the latter case. Two different methods of selecting the first and last point in the sampling window have been used. The first method selects by bracketing the portion of the seismogram with significant amplitude according to the following algorithm,

(1) Set a cutoff value for the amplitude at some fraction of the maximum absolute value of amplitude in the seismogram (usually .01 or .05)

(2) Let the sample at the location of the maximum absolute value be the first sample in each of two series. One series proceeds forward in time, the other backward. Scan each series until a subseries of samples n seconds in duration, all with amplitudes smaller than the cutoff amplitude, is found. The first point in each of these subseries defines an endpoint of the longest possible sampling window.

(3) Calculate the RMS amplitude for sampling windows with durations 15, 20, 25, .., 85 sec. If the duration of a sampling window exceeds the duration of the seismogram then the longest sampling window used is the duration of the seismogram.

This algorithm fails when a period of sustained low amplitude ($> nsec$) occurs within the desired trace, or when small arrivals precede the main arrival on only a subset of the traces. The second algorithm selects the point in the time series for a time ten seconds before the peak maximum absolute amplitude as the first point in the window. The end of the seismogram is defined by the first point in a five second sample of sustained low amplitude. The combination of these two methods gives stable RMS amplitudes in all cases considered.

These algorithms yield a series of RMS amplitude values that can be used to compare results derived using different methods. If RMS amplitudes agree within all period ranges, and waveforms are similar the fit is considered to be excellent. Examining the behavior of the RMS amplitude as a function of sample window length can give insight into the nature of and the underlying reasons for misfit between methods.

Tests of Accuracy: SH L_g Mode Sum Input

A series of tests were conducted to verify the accuracy of the coupling method and the efficiency of the absorbing BC's. The tests used the continental reference model and a set of ninety forcing functions calculated for a strike slip point double couple source at a depth of 8 km and a distance X=1500 km. Transparent BC's were applied when necessary, as explained in the discussion of the test results. The BC's are discussed below before the test results are presented.

The BC's are introduced to remove the nonphysical reflections created by the artificial grid boundaries at the ends and bottom of the grid. Removing these reflections by extending the grid requires an increase in execution time of between 30% and 500%. As a comparison the approximate BC used in this study increases execution time by 3-5%. The BC used here, suggested by Frazier, Alexander, and Petersen (1973), calculates the average of the rigid boundary and the free boundary displacements for each edge node at each time step. For a normally incident plane wave this average exactly represents the transparent boundary. However in practice the incident wavefront is neither normally incident nor a plane wave. This means that the actual value at the transmitting boundary is a linear combination of the rigid boundary and free boundary solutions whose coefficients depend upon the angle of incidence of the energy. The boundary condition used here assumes that the average of the two solutions will in most cases be the best approximation to the transparent boundary that can be simply implemented.

The results of the accuracy and BC tests presented below are illustrated in Figure 5. A continental reference structure is used for both the FE and PM portions of the path. This allows the direct comparison of the hybrid solutions, those solutions propagated from the source to the receiver using a combination of methods, to direct analytic synthetics, those calculated entirely with the PM technique. Four separate calculations were performed. Results, from each of these calculations, were recorded at 20 and 40 km into the grid. First, L_g mode sum direct analytic seismograms for the same source used to generate the C/O transition forcing functions were calculated. Next, seismograms were generated using

the hybrid method in a grid long enough (100X50 km) to prevent contamination from end reflections. Third, seismograms were generated using the hybrid method and a short (50X50 km) grid with the transparent BC applied at each node on it's rightmost edge. Finally, the previous FE calculation was repeated without the transparent BC's. The excellent agreement between the analytic and hybrid synthetics verifies the validity of the coupling method applied to a layered half-space. Small discrepancies are seen in the higher frequency component, particularly in the first twenty seconds of the trace. In the last trace in each group in Figure 5 the single and multiple reflections from the grid edge are clear. Comparison of the long grid and the short grid with and without BC's shows that most of the reflected amplitude has been removed by the BC's. The misfit is lower for the longer period component of the traces. The significant misfit is coincident with reflections, and is largest for the multiple reflections. Despite visible differences in waveform the seismograms shown in Figure 5 have RMS amplitudes that agree to within less than 2% for all RMS window lengths. This indicates that small changes in waveform may be expected but the RMS amplitudes of the seismograms should be stable and not significantly contaminated by incompletely removed reflections from the grid edges. The increased discrepancies in both waveform and amplitude introduced by the multiple reflections will be avoided in the transition FE grids described below. This reduces the discrepancies in RMS amplitude to less than 1%.

Reflections from the bottom edge of the grid should also be considered. The transparent BC can be very inefficient for the small angles of incidence seen at the grid bottom when a distant source is considered (Regan, 1987). Fortunately, in a layered half-space, where L_g waves can be modelled as the superposition of multiply reflected post-critical SH waves in the crust, most of the energy in the SH type L_g waves should be trapped in the crustal layer. The time slices discussed later (Figures 6, 12) show that the SH type L_g waves propagating in a layer over a half-space are, in the most part, confined within the layer. RMS amplitudes agree to within less than 0.1% with and without the BC's (Regan 1987). However, the purpose of the present study is to examine the effects of continental oceanic boundaries on the transmission of L_g mode sum seismograms. When the crustal layer is thinned or thickened with distance, the modes are no longer completely trapped within the layer. Energy can be converted to modes compatible with the local layer thickness and to other forms including body waves that can propagate into the half-space. When the wavefield reaches the second layered structure, modes not trapped within the new crustal layer will leak out of the layer, rapidly at first, then at a steadily decreasing rate. This implies that wide angle reflections

of energy escaping from the crustal layer towards the bottom boundary of the grid could possibly contaminate transition calculation results. However, the model grids do not extend far enough, in the x direction, beyond the transition, for this to be a problem. The energy will encounter the rightmost end of the grid, either on the downgoing or the upgoing portion of its path, rather than reaching a receiver at or near the surface as a wide angle reflection. Since a wavefront which has a small angle of incidence with the bottom boundary has a large angle of incidence with respect to the end boundary, most of the amplitude of the wavefront incident on the rightmost end boundary, will be transmitted rather than reflected. Therefore, it is removed from the grid. Careful grid design will prevent significant contamination from wide angle bottom reflections.

Changes to L_g Wavetrains on Passage through a C/O Transition and Their Dependence on L

When a wavefield consisting of SH L_g mode sum energy passes through a C/O transition region such as that illustrated in figure 4a) several important things happen. In order to clearly explain these effects and their variation with L one must think of the wavefield in terms of several components. The wavefield may be divided into an incident wavefield, a reflected wavefield, and a transmitted wavefield. The incident wavefield is composed of the trapped modal SH L_g energy arriving from the source, and is present and complete only in the region of continental structure. In the transition region some components of the incident wavefield are present, but as the wavefield travels through the transition region more of these components are converted to reflected and transmitted wavefield components. The reflected wavefield is composed of trapped and leaking modes which have been reflected from the boundaries in the transition region when the incident wavefield interacts with them. The reflected wavefield travels sourceward through the crustal layer, of the transition region, and of the region of continental structure. The transmitted wavefield is composed of all the energy transmitted through the transition region into the crustal layer of the region of oceanic structure, and all the energy transmitted into the mantle layer. The transmitted wavefield is divided into four components, two in the mantle layer, two in the crustal layer. The forward transmitted wavefield is the portion of the incident energy which crosses the crust mantle boundary (CMB) into the mantle layer when the incident wavefield interacts with the CMB. The reverse transmitted wavefield is the portion of the reflected energy which crosses the CMB into the mantle layer when the reflected wavefield interacts with the CMB. The forward transmitted wavefield is present in the transition region and the region

of oceanic structure. The reverse transmitted wavefield is present in the transition region and the region of continental structure. The directly transmitted wavefield is the portion of the energy in the incident wavefield that passes through the crustal layer of the transition region and into the crustal layer of the region of oceanic structure without modal conversion. The transformed transmitted wavefield is the component of the incident wavefield which is converted into a new set of trapped and leaking modes as it passes through the crustal layer of the transition region into the crustal layer or the region of oceanic structure.

Each of the components of the wavefield discussed above will be illustrated in the time slices or seismograms for the 25 km C/O transition region. These time slices and seismograms are presented as an example of the general transmission properties of simple transition regions. The variation of such transmission properties with L will also be illustrated. The observed properties and their variations with L will then be explained.

A series of time slices for the 25 km C/O transition is shown in Figure 6. In the first time slice the displacements entering the grid as dark, almost vertical bars are those which produce the largest peak to peak amplitudes in the seismograms. The third time slice shows the same high frequency arrivals after they have propagated about halfway through the transition region. The maximum amplitudes seen within the transition region of the third time slice are almost twice those seen in the unperturbed layer over a half-space wavefield seen in the first two time slices. So, the plotted amplitudes of all the displacements in the third time slice have been significantly reduced by scaling, making the same disturbances appear smaller. In the fourth time slice the highest amplitude regions of the wavefield have propagated past the rightmost edge of the grid. The maximum amplitude is much smaller so the same disturbances appear to have much larger amplitudes. The fifth time slice shows a further amplification of the amplitude of the disturbances due to scaling. The amplification helps make the highest amplitude portion of the reflected wavefield ($< 5\%$ of incident amplitude) visible as a series of broken vertical bars near the leftmost end of the grid. All sections of the incident wavefield show triangular regions of maximum amplitude. The extent of each triangular region, in the x direction, increases for regions of the wavefield incident on the left end of the grid at a later time. The end of the incident wavefield is seen, in the fifth time slice, about midway between the left grid edge and the arrow, to the right of the visible reflected component. The C/O transmitted wavefield is visible in the last three time slices as disturbances travelling through the half-space from the CMB towards the rightmost edge of the grid. The reverse transmitted wavefield is clearly visible in the fifth time slice.

and present in the last three time slices, as disturbances travelling through the half-space from the CMB towards the grid bottom and the source. For the earliest disturbances in the half-space the forward transmitted wavefield propagates along a path approximately parallel to the crust mantle interface in the oceanic region, and the reverse transmitted wavefield propagates along paths nearly parallel to the CMB. As time progresses the propagation paths of both the forward and reverse transmitted wavefields approach the normal to the CMB. Energy escaping from the transformed transmitted wavefield as it propagates through the oceanic crustal layer forms a forward bending arc of higher amplitudes in the mantle half-space. As the high amplitude regions of the forward transmitted wavefield propagate longer distances or propagate along paths with larger vertical components the tails forming due to leakage from the oceanic crustal layer detach from the from the forward transmitted wavefield.

Figure 7 shows seismograms recorded at the receivers along a surface section. These seismograms illustrate the magnitude of the concentration of amplitude at the surface of the crust seen in the time slices, and the change in the waveforms as the wavefield passes through the transition. Figure 8a shows the variation of 50 second RMS amplitude with distance, X2, from the source for each of the C/O transition FE calculations. Since the relative amplitudes produced using the different C/O transition lengths are being compared the absolute values of the amplitudes, which are dependent on source magnitude, are not shown. The amplitudes recorded at nodes along the surface of the crustal layer within each transition region show a general increase as one moves from B towards D. The length of the coda with amplitudes above one third of the maximum peak to peak amplitude is also increasing. The size of the increase in RMS amplitude is smallest for the step transition and increases as L increases. Superimposed on the general increase is an oscillatory term. The method of scaling the distance coordinate within the transition region, in Figure 8, makes the coincidence of maxima and minima at approximately the same fraction of the transition length for all L's considered very clear. Increases in amplitude before reaching distance B are due to energy reflected from the transition boundaries back towards the source. The amplitude increase near B is largest for a step transition and decreases as L increases. The fluctuations in amplitude following the transition region show that the wavefield has not stabilized in the few kilometers beyond the transition regions illustrated in this figure.

Figure 9 shows seismograms recorded on depth sections at distances B and D. Figure 10 shows the variation of 50 second RMS amplitude with depth at several distances. The

seismograms at the depth of the surface of the oceanic crustal layer show a 50% increase in amplitude as the energy travels from B to D. They also show that the amplitude of the coda becomes a larger portion of the maximum peak to peak amplitude. The nodes at the depth of the bottom of the oceanic crustal layer show a small decrease in RMS amplitude across the transition. Examination of the nodes at B and D with depths between these pairs (not illustrated) shows that the increase in amplitude is largest at the surface of the crust and decreases rapidly toward the base of the crust. The amplitudes of the seismograms transmitted across the CMB are decreased by passage through the transition region. The transmitted waveforms are similar to the incident waveforms and show an increasing reduction in transmitted amplitude as depth increases. Amplitude is seen at depths below the depth of the bottom of the continental crustal layer. The amplitudes in the mantle layer within the transition region are maximum immediately below the CMB, and decay nearly exponentially with depth below that boundary. The amplitude of the transmitted seismograms recorded at nodes below the oceanic crustal layer and above the base of the continental crustal layer, at D, decreases as L increases. Below this depth the trend reverses. At distances E and F, further from the transition region, the magnitudes of these trends decrease. These observations are further support that as L increases larger energies are transmitted across the CMB and that these energies propagate downward more rapidly.

The triangular pattern of maximum amplitudes in the wavefields (figure 6) can easily be explained. Consider the SH L_g energy in the crustal layer a superposition of of post-critically reflected multiple SH wave reflections. The critical angle is about 51°. Since the wavefront is perpendicular to the ray, the wavefronts that are visible as the triangular regions of maximum amplitudes should show the observed angles of incidence with the boundary of between 0° and 39°. The increase in width of the triangular maxima corresponds to an decrease in group velocity which can be translated to a decrease in period and/or a larger contribution from higher modes. The later parts of the seismogram are predominantly higher mode energy.

Figure 11 illustrates two pairs of ray diagrams, one for a 25 km C/O transition region, the other for a 100 km C/O transition. These diagrams are useful when explaining the trends observed in the results presented above, and their dependence on L. To clearly explain some trends multiple reflections within the transition region need to be considered. In this paragraph the notation and relations needed in such explanations will be defined. For the

case of multiple reflections, the labeled incident angle j, will become j_1, and the incident angle for subsequent reflections within the transition will be denoted j_n, where n denotes the n^{th} reflection of the ray after it enters the transition region. Similarly, the transmitted rays for the n^{th} reflection of a ray after entering the transition region, will be denoted j'_n. The upper transition in each pair shows ray paths when the rays encounter the CMB of the transition before the COB. When these rays reach the CMB their incident angles, i, are reduced by the angle, ϕ_{cm}, so that, $j_1 = i - \phi_{cm}$. As long as the ray remains in the transition region, $j_n = i - n(\phi_{cm} + \phi_{co}) + \phi_{co}$. The lower transition in each pair shows the ray paths when the rays encounter the COB before they encounter the CMB. For this case ϕ_{oc}, and, ϕ_{cm} are interchanged in the expression for j_n. The energy transmitted across the CMB, with $j_n > 0$, forms the forward transmitted wavefield. If the value of j_n becomes negative before it reaches the end of the transition then the ray has been reflected, and successive values of j_n will become more negative until the reflected wavefront reaches the continental structure. The energy transmitted across the CMB, with $j_n < 0$, forms the reverse transmitted wavefield. The angle of incidence is j_{oc}, in the oceanic crustal layer, and j_{con} for the reflected wave in the continental crustal layer. When the first reflection of the ray exiting the transition region, from the upper or lower boundary of either the continental or oceanic crustal layer, is the n^{th} reflection then $j_{con} = j_{oc} = j_n + \phi_{oc}$, or $j_{con} = j_{oc} = j_n + \phi_{cm}$, respectively. Also useful in the following discussions is the transmission coefficient as a function of the incident angle, j_n. For the examples discussed here the displacement transmission coefficient, $T_n(j_n) = \frac{2\cos(j_n)}{\cos(j_n)+1.62\cos(j'_n)}$, varies monotonically between zero for the critical angle $j_n = 51°$, and .76 for normal incidence, $j_n = 0$.

The growth in amplitude for seismograms at crustal surface nodes as distances range from B to D can be explained in terms of energy concentrated in the thinning crustal layer of the transition region. As j_n decreases toward zero for successive n's, the reflection points at the boundaries in a transition region are separated by smaller horizontal distances. This implies that the density of rays will increase as the crustal layer thins, thereby producing higher amplitudes. An equal concentration would be expected at the CMB if no energy was transmitted across that boundary. In fact, for a model with the same geometry but with the mantle half-space replaced by water to disallow transmission across the CMB, an amplification of 75% is observed at both boundaries. However for continent ocean boundary models, as j_n and thus, j'_n, decrease the transmission coefficient, T_n, increases. When more energy is concentrated at the CMB more energy is transmitted across it. The escape of energy

from the crustal layer to form the transmitted wavefield also explains the distribution of amplitude with depth within the crustal layer of the transition. The amount of concentration of amplitude increases as the distance from the CMB increases and the effects of the energy escaping across it become weaker.

Extending the above arguments explains the increase in the amount of concentrated energy, the increase in the magnitude of the transmitted wavefield, and the decrease in the amplitude of the reflected wavefield as L increases. As L increases the angles ϕ_{cm} and ϕ_{co} decrease causing j_n to decrease more slowly and allowing the number of reflections, m, within a transition to increase. When L increases, the increase in m causes an increase in ray density and explains the increase in concentrated amplitude at the COB. When L increases the amount of energy concentrated at the CMB also increases. The transmission of this energy across the CMB causes the amplitude of the transmitted wavefield to increase as L increases. Since the amount of amplitude concentrated at the COB and thus transmitted into the oceanic crustal layer, and the amount of energy concentrated at the CMB and thus transmitted across the CMB both increase as L increases the amplitude of the reflected wavefield must decreases as L increases. Let seismogram A be a hybrid seismogram recorded on depth section A (Figure 4) in a C/O transition calculation. Let seismogram B be the hybrid seismogram, recorded during the continental reference calculation, at the same depth and distance from the source as seismogram A. The reflected component of is measured by analyzing the component which remains when seismogram B is subtracted from seismogram A. Reflected amplitudes measured in this manner show a clear decrease as L increases.

Figure 11 can be used to explain how and why the direction of propagation of the forward and reverse transmitted wavefields varies as time progresses. When the arrivals of the highest group velocity reach the CMB the resulting forward transmitted wavefield travels along a path approximately parallel to the crust half-space interface in the oceanic structure, and the resulting reverse transmitted wavefield travels along a path almost parallel to CMB. The incident angles j_n are maximum. As $|j_n|$ for a given n, and the group velocity, decrease the values of j'_n decrease. Thus, the propagation direction of both transmitted wavefields approach the normal to the CMB. As L increases larger values of n are possible within the transition region. For each value of n a transmitted wavefield is created at the CMB. Therefore, the range of propagation directions seen at a given time increases as L increases.

The directly transmitted wavefield and the transformed transmitted wavefield can also be easily explained. For reflections points immediately preceding the beginning of the transition

region some rays ($i > 90 - arctan(27/L)$) can propagate through the transition region without interacting with either the CMB or the COB. These rays, which form the directly transmitted wavefield, continue to bounce with the same post-critical angles of incidence at the crust mantle interface and the free surface as they did in the continental structure. They represent the energy transmitted through the transition directly, without changes in period or phase velocity. For these rays no mode conversion has occurred and no energy has been converted to other phases. These rays form the unchanged components of the eigenfunctions defining each mode. The range of angles, i, over which the direct transmission occurs decreases as L increases. Thus, more unconverted energy is transmitted through shorter transitions. In contrast, the transformed transmitted wavefield is composed of rays which interact with the CMB or COB before being transmitted into the oceanic crustal layer. Such rays show changes in group velocity that indicate modal conversions are occurring. Energy is also converted into other phases as it escapes across the CMB. As discussed above, the energies transmitted into the oceanic crustal layer and across the CMB both increase as L increases. As L increases, this increased transmitted energy is partially counteracted by the effects of decreased transmission of unconverted energy. This helps explain why the differences due to L are small. It should be noted that increasing L reduces the rate at which the crustal thickness changes, so at a given distance from the beginning of a transition region the change in amplitude transmitted across the CMB per unit horizontal distance becomes smaller as L increases. However, integrated over the entire length of the transition region the amount of energy transmitted across the CMB increases.

The diagrams in Figure 11 demonstrate why energy crosses the crust mantle interface in the oceanic structure following the transition, why this transmitted energy is maximum near the transition and decreases as the distance from the transition increases, and why this transmitted energy increases as L decreases. The paths illustrated in the second 25 km transition outline show one way modes which are not of appropriate frequencies to be trapped within the oceanic crustal layer, enter that layer. Analogous paths for rays which interact first with the CMB or rays which interact multiple times with the crustal boundaries in the transition region also exist. All such rays produce rays at pre-critical, $j_{oc} < 51°$, angles within the oceanic crust. For any such ray, the transmission coefficient at each successive reflection from the crust mantle interface is $T(j_{oc})$. Thus, the proportion of reflected amplitude remaining in the crust after the n^{th} bounce is $A_n = (1 - T(j_{oc}))^n A$, where A is the original amplitude. Clearly, the amount of escaping energy decreases with distance.

For a shorter transition j_n, for a given i, is smaller. Thus, a larger range of angles $j_{oc} < 51°$ are produced for each path through the shorter transition. This means a higher density of pre-critical rays and higher amplitudes in and escaping from the oceanic crustal layer of shorter transitions.

The use of the interpretation of L_g waves in terms of multiply reflected SH rays to the interpret the FE results has been instructive. However, the many interacting effects involved in determining the properties of the reflected, converted, and transmitted wavefields would be extremely difficult to predict using this approach. Thus, the FE method is necessary to determine which effects are important and which need not be considered.

Changes to L_g Wavetrains on Passage through a O/C Transit ion Region and Their Dependence on L

The passage of a wavefield consisting of SH type L_g mode sum energy for a continental layer over a half-spac · model, which has passed through a C/O transition of 50 km length. through a O/C transition such as that illustrated in Figure 4b) has several effects on the wavefield. Results of the calculations for propagation through a 50 km O/C transition will be presented in detail as to illustrate these effects. The O/C transition tests using a variety of L's will be summarized to illustrate how these effects depend on L. The noted effects and their variations with L will be explained. Before proceeding to these discussions the errors introduced due to the truncation inherent in coupling the C/O transition FE results into the O/C transition grid should be mentioned. The finite vertical extent of nodes driven by forcing functions at the leftmost edge of the O/C transition grid will cause a vertical truncation of the incoming wavefield. Also, any reflections included in the seismograms recorded to use as forcing functions will be added to the forward propagating wavefield in the O/C calculation. These effects tend to increase the amplitudes at the surface of the oceanic layer near the left end of the grid. The uncertainties introduced by the coupling process appear to increase the amplitudes in the second grid by as much as 3%. Therefore, they could possibly lead to a slight underestimate of the magnitude of the attenuation effect, but should not lead to an overestimate.

A series of time slices, shown in Figure 12, illustrate the FE calculation results for the 50 km long O/C transition. The highest amplitude concentrations visible in first four slices correspond to the maximum amplitudes in the seismograms. The first two time slices illustrate the wavefield travelling through the oceanic structure. The third time slice illustrates the passage of the highest amplitude portions of the wavefield through the transition region.

In the fourth time slice these highest amplitude regions appear at the rightmost end of the grid. In the fifth time slice they have exited the grid. The maximum amplitude in a given time slice decreases with time in the third to fifth time slice. The maximum amplitudes in the transition region decrease as the wavefront proceeds through the transition region. Thus, normalizing by the largest amplitude in each slice causes identical disturbances to increase in extent and intensity in successive slices. Triangular regions of maxima can be seen in the oceanic crust but they are not nearly so clear as those seen in the continental crust of the C/O transition. The third and fourth time slices clearly show that the energy which was previously trapped in the oceanic crustal layer distributes itself throughout the crustal layer as it passes through the transition region and the region of continental structure. The amplitudes remain much larger near the surface, and decay rapidly with depth. The fifth time slice shows triangular regions maximum amplitude are beginning to appear in the continental structure. Additional calculations show further propagation in x is necessary to stabilize the wavefield in the region of continental structure .

The disturbances seen in the half-space of the oceanic region of the O/C transition grid contain significant energy. Examining the time slices shows that for a subset of these disturbances, equivalent to the forward transmitted wavefield discussed earlier, the z component of translation in the half-space is increasing for successive groups of disturbances. This is due to the interactions at the CMB in the C/O transition as explained earlier. It is more visible in these time slices than the C/O transition time slices due to the increased distance from the CMB. It is clear that these packets of amplitude are translated rapidly enough in z that some will pass into the half-space below the continental crustal layer before they reach the O/C transition region. Thus, the energy contained within them escapes the system and is not reconverted to L_g energy when the wavefield passes through the O/C transition. The amount of energy escaping from the system in this manner increases as L, or the length of the intermediate oceanic path, increases.

Figure 13 shows a surface section of seismograms for a 50 km O/C transition. Figure 8b shows the variation of 50 second RMS amplitude with distance, X2, from the source for each of the O/C transition FE calculations. A decrease in RMS amplitudes is seen as one moves along the surface of the oceanic crustal layer approaching the transition region. This decrease is clear for short RMS windows and almost vanishes for window length of 65 sec or more. This indicates that the portion of the coda with amplitudes comparable to the maximum amplitude is decreasing in length. Superimposed on this slow decrease in amplitude is an

oscillatory term with amplitude approximately 15% of the mean amplitude at the surface in the oceanic structure. The RMS amplitudes recorded at nodes along the surface of the crustal layer within each O/C transition region decrease as one moves from B towards D. The size of this decrease is smallest for the step transition and increases as L increases. The rate of decay shows some tendency to become smaller towards the end of the transition. The superimposed oscillations seen in the O/C transition results are much smaller than those seen in the C/O transition results. They appear to be confined near the beginning of the transition region. The oscillation in amplitude following the transition region shows that the wavefield has not stabilized in the few kilometers beyond the transition regions illustrated in figure 8b. Additional results which are not illustrated show the RMS amplitude continues to decrease slowly until the wavefield readjusts to the new continental structure.

Figure 14 shows the variation of 50 second RMS amplitude with depth. At the depth of the surface of the oceanic crustal layer propagation through the transition reduces the RMS amplitude by more than a factor of two, and the peak to peak amplitude by 25%. This indicates that the length and amplitude of the coda are decreasing more rapidly than the amplitude of the largest arrival. At depths between the surface of the continental crust and the surface of the oceanic crust amplitude decreases with depth. Then energy incident on the MCB is largely transmitted across the MCB into the crustal layer. Some of this energy eventually escapes across the CMB in the region of continental structure. The amplitudes below the crustal layer of the transition region decrease slowly with depth or even increase with depth. An increase of amplitude with depth below the crustal layer indicates that energy is travelling down toward the grid bottom and out of the system being considered.

Most of the energy incident on the MCB is transmitted across it. Thus, in the last four time slices, the reflections from the MCB are not easily separated from the later portions of the incident wavefield. The pattern of displacements seen in the oceanic half-space is distorted when the energy producing it is transmitted across the MCB. The uppermost portion of a disturbance crosses the boundary first and begins to move more slowly. The remainder of the disturbance, still in the mantle layer continues to move with the mantle's faster velocity. As the disturbance moves through the length of the transition, an increasing section of it moves into the crustal layer. This results in a slope being superimposed on the portion of the disturbance which has propagated back into the crustal layer. The slope, $Slope = [\frac{L(v_M - v_c)}{v_M}]$, is dependent on L, the velocity in the crustal layer, v_c, and the velocity in the mantle, v_M. This slope, in this case about $\tan 52°$, is observed easily in both the second

and third time slices. It is also seen in the fourth and fifth time slices. However, in these time slices the amplitude incident from the oceanic crustal layer dominates that transmitted from the oceanic mantle layer making observation of the slope more difficult.

The effect of the O/C transition region on the energy previously travelling in the oceanic crustal layer will now be discussed. Concentrations of amplitude incident from the oceanic crustal layer travel up the surface of the OCB. As they propagate up the OCB the lower edge of the amplitude concentrations are no longer constrained by the lower edge of the oceanic crustal layer. Consequently the energy can migrate downwards towards the depth of the base of the continental crustal layer. This diffusion of energy can be explained using a mechanism which is the converse of that used to explain the concentration of energy in the C/O transition. The incident angle for the ray perpendicular to each wavefront, j_n, increases as n increases. Subsequent reflection points are separated by larger horizontal distances producing a dilution in ray density and thus a decrease in amplitude. However, there is an important difference that simplifies the analysis of the O/C transition. Incident angles, j_1, for all rays trapped in and travelling through the oceanic crustal layer are greater than 51°. For $n > 1$ these angles increase. Therefore, no energy originally trapped in the oceanic crust is transmitted across the MCB, or reflected back toward the source.

Observations indicate that the length of the intermediate oceanic path between the C/O and O/C transitions is important. The results of this study suggest some reasons why this is so. For short paths energy transmitted in to the mantle layer has little time to travel towards the bottom of the grid and thus out of the region of consideration before much of it passes back into the crustal layer in the O/C transition region. This implies that there may be a critical length of intermediate oceanic path beyond which enough of the energy has escaped from the region of interest that amplitudes of the attenuated L_g recorded after the O/C transition would be reduced sufficiently to explain the observed data. To completely analyze this assertion requires the use of the RT coupling method for continuing FE calculations through a plane layered structure using RT integration and PM Green's functions. The accuracy of the numerical implementation of this method must be established before such calculations can be presented. Therefore, the discussion of the numerical implementation of this method and of the results examining the effects of the intermediate path length in the oceanic structure will be left for other papers.

Conclusions

The effects produced when a SH L_g mode sum wavefield is propagated through a C/O transition region, and their dependence on L, will now be summarized. Amplitudes at the surface of and in the crust are amplified by as much as 50% as the wavefield passes through the transition region. These amplitude increases in the crustal layer have been explained by the increased ray density in the thinning crustal layer. The amount of amplification increases as L increases. Increased numbers of reflections within a longer transition region, cause an increase in ray density, explaining the increase in energy as L increases. Amplification is maximum at the surface and decreases with depth until the base of the oceanic crust is reached. Amplitude is transmitted across the CMB and but not across the COB. Thus, the amplification is maximum at the COB and decays as the CMB is approached and the effects of energy transmitted across the CMB increase. The amount of energy transmitted across the CMB increases as L increases. The translation direction of the forward transmitted wavefield has a larger vertical component later in the seismogram when it approaches the normal to the CMB. Thus, for a longer transition, with a smaller ϕ_{cm} and thus a more horizontal CMB, the path length in the oceanic structure will have a larger vertical component. This will allow the transmitted energy to escape the system more readily as L increases.

After the wavefield has travelled through the transition region additional energy escapes from the crustal layer in the oceanic structure. This leakage is largest near the end of the transition region and decreases with distance away from it. The size of the decrease in amplitude is controlled by the energy in wavefronts propagating through the oceanic crustal layer with pre-critical angles of incidence. At each successive reflection of such a wavefront at the crust half-space interface in the oceanic structure, a fraction of the total amplitude remaining, $T(j_{oc})$ is transmitted across the interface. Thus, the total amplitude of this component decays most rapidly in the first kilometers of the oceanic structure while the incident wave still has significant amplitudes.

Next, a summary of the important observations for the O/C transition will be given. As the wavefield travels through the O/C transition region the surface amplitude decreases rapidly. The energy forming the concentrations of amplitude previously trapped in the oceanic crustal layer travels up the OCB while spreading itself throughout the crustal layer. The maxima in these regions remain at the surface. The amplitude decreases rapidly with depth down to the crust mantle interface. The amplitude incident upon the MCB from the oceanic half-space is transmitted across it with a resulting distortion in the wavefield.

The form of this distortion is the superposition of a slope, Slope = $\tan^{-1}\left[\frac{v_M - v_c}{v_M}\right]$, onto the disturbance incident at the MCB after it has passed into the continental crustal layer.

Finally, attenuation of L_g propagating along a mixed path with simple transition regions and an oceanic path length of 147 km, is not sufficient to explain the observed values. The highest attenuations observed produced a reduction of a factor of two to three in amplitude. Observations of the trends due to varying L indicate that a longer C/O transition could increase the attenuation. But, even using the optimal L attenuation of more than a factor of four would not be expected. Thus, other factors and/or more complex structures must be considered to explain the observed attenuation of L_g along mixed paths.

Acknowledgments

J. Regan conducted part of this research while a Canadian Government Laboratory Visiting Fellow at Geophysics Division, Geological Survey of Canada, Ottawa. This research was supported in part by the Advanced Research Projects Agency of the U. S. Department of Defense and was monitored the U. S. Air Force Geophysics Laboratory under Contract F19628-87-K-0028. Division Of Geological Sciences Contribution No. 4623. Geological Survey of Canada Contribution No.

References

Alsop, L. E., (1966). Transmission and Reflection of Love Waves at a Vertical Discontinuity, *J. Geophys. Res.*, **71**, 3969–3984.

Barker, B. W., Der, Z. A., Mrazek, C. P., (1981). The Effect of Crustal Structure on the Regional Phases P_g and L_g at the Nevada Test Site, *J. Geophys. Res.*, **86**, 1686–1700.

Bath, M., (1954). The Elastic Waves L_g and R_g along Euroasiatic Paths, *Arkiv for Geofysik*, **2**, 295–342.

Blandford, R., (1982). Seismic Event Discrimination, *Bull. Seismol. Soc. Am.*, **72**, s69–s87.

Bolt, B. A., (1957). Velocity of the Seismic Waves L_g and R_g across Australia, *Nature*, **180**, 495.

Bollinger, G. A., (1979). Attenuation of the L_g Phases and Determination of m_b in the Southeastern United States, *Bull. Seismol. Soc. Am.*, **69**, 45–63.

Boore, D., (1970). Love Waves in Nonuniform Wave Guides: Finite Difference Calculations, *J. Geophys. Res.*, **75**, 1512–1527.

Bose, S. K., (1975). Transmission of SH Waves across a Rectangular Step, *Bull. Seismol. Soc. Am.*, **65**, 1779–1786.

Bouchon, M., (1981). A Simple Method to Calculate Green's Functions for Elastic Layered Media, *Bull. Seismol. Soc. Am.*, **71**, 959–971.

Bouchon, M., (1982). The Complete Synthesis of Seismic Crustal Phases at Regional Distances, *J. Geophys. Res.*, **87**, 1735–1741.

Campillo, M., Bouchon, M., Massinon, B., (1984). Theoretical Study of the Excitation, Spectral Characteristics, and Geometrical Attenuation of Regional Seismic Phases, *Bull. Seismol. Soc. Am.*, **74**, 79–90.

Chung, D. H, Bernreuter, D. L., (1981). Regional Relationships among Earthquake Magnitude Scales, *Reviews of Geophys. Space Phys.*, **19**, 649–663.

de Hoop, A.,T., (1958). Representation Theorems for the Displacement in an Elastic Solid and Their Application to Elastodynamic Diffraction Theory, Sc. D. Thesis. Technische Hogeschool, Delft.

Drake, L. A., (1972). Love and Rayleigh Waves in Nonhorizontally Layered Media, *Bull. Seismol. Soc. Am.*, **62**, 1241–1258.

Drake, L. A., Bolt, B. A., (1980). Love Waves Normally Incident at a Continental Boundary, *Bull. Seismol. Soc. Am.*, **70**, 1103–1123.

Dwyer, J. J., Herrmann, R. B., Nuttli, O. W., (1983). Spatial Attenuation of the L_g Wave in the Central United States, *Bull. Seismol. Soc. Am.*, **73**, 781–796.

Eittreim, S., Grantz, A., (1979). CDP Seismic Sections of the Western Beaufort Continental Margin, *Tectonophysics*, **59**, 251–262.

Frazier, G. A., Alexander, J. H., Petersen, C. M., (1973). 3-D Seismic code for the ILLIAC IV. *Systems, Science and Software Report SSS-R-73-1506.*

Gregersen, S., (1978). Possible Mode Conversion between Love and Rayleigh Waves at a Continental Margin, *Geophys. J. R. Astr. Soc.*, **54**, 121–127.

Gregersen, S., (1984). L_g Wave Propagation and Crustal Structure Differences near Denmark and the North Sea, *Geophys. J. R. Astr. Soc., vol. 79*, 217–234.

Gregersen, S., Alsop, L. E., (1974). Amplitudes of Horizontally Refracted Love Waves. *Bull. Seismol. Soc. Am.*, **64**, 535–553.

Gregersen, S., Alsop, L. E., (1976). Mode Conversion of Love Waves at a Continental Margin, *Bull. Seismol. Soc. Am.*, **66**, 1855–1872.

Harkrider, D. G., (1964). Surface Waves in Multilayered Media I, Rayleigh and Love Waves from Buried Sources in a Multilayered Elastic Half-Space, *Bull. Seismol. Soc. Am.*, **54**, 627–679.

Harkrider, D. G., (1970). Surface Waves in Multilayered Elastic Media, Part II. Higher Mode Spectra and Spectral Ratios from Point Sources in Plane Layered Earth Models. *Bull. Seismol. Soc. Am.*, **60**, 1937–1987.

Harkrider, D. G., (1981). Coupling Near Source Phenomena into Surface Wave Generation, 277-326 in *Identification of Seismic Sources- Earthquake or Underground Explosion*, ed. Husebye, E. S., Mykkeltveit, S., eds, Reidel.

Herrin, E., Minton, P. D.,(1960). The Velocity of L_g in the Southwestern United States and Mexico, *Bull. Seismol. Soc. Am.*, **50**, 35–44.

Herrmann, R. B., Kijko, A., (1983). Short Period L_g Magnitudes: Instrument. Attenuation, and Source Effects, *Bull. Seismol. Soc. Am., vol. 73*, 1835–1850.

Herrmann, R. B., Nuttli, O. W., (1975). Ground Motion Modelling at Regional Distances for Earthquakes in a Continental Interior, II. Effect of Focal Depth, Azimuth. and Attenuation, *Int. J. Earthq. Engng. Struct. Dyn.*, **4**, 59–77.

Herrmann, R. B., Nuttli, O. W., (1982.) Magnitude: the Relation of M_L to m_{bL_g}. *Bull. Seismol. Soc. Am.*, **72**, 389–397.

Hinz, K., Schluter, H.-U., Grant, A. C., Srivastava, S. P., Unpleby, D., Woodside. J., (1979). Geophysical Transects of the Labrador Sea: Labrador to Southwest Greenland, *Tectonophysics*, **59**, 151–183.

Hudson, J. A., (1977). The Passage of Elastic Waves through an Anomalous Region-IV. Transmission of Love Waves through a Laterally Varying Structure, *Geophys. J.*, **49**, 645–654.

Hudson, J. A., Knopoff, L., (1964). Transmission and Reflection of Surface Waves at a Corner: I. Love Waves, *J. Geophys. Res.*, **69**, 275–280.

Jones, F. B., Long, L. T., McKee, J. H., (1977). Study of the Attenuation and Azimuthal Dependence of Seismic Wave Propagation in the Southeastern United States, *Bull. Seismol. Soc. Am.*, **67**, 1503–1513.

Kazi, M. H., (1978a). The Love Wave Scattering Matrix for a Continental Margin (Theoretical), *Geophys. J. R. Astr. Soc.*, **52**, 25–44.

Kazi, M. H., (1978b). The Love Wave Scattering Matrix for a Continental Margin (Numerical), *Geophys. J. R. Astr. Soc.*, **53**, 227–243.

Keen, C. E., Hyndman, R. D., (1979). Geophysical Review of the Continental Margins of Eastern and Western Canada, *Can. J. Earth Sci.*, **16**, 712–747.

Kennett, B. L. N., (1973). The Interaction of Seismic Waves with Horizontal Velocity Contrasts, *Geophys. J. R. Astr. Soc.*, **33**, 431–450.

Kennett, B. L. N., Mykkeltveit, S., (1984). Guided Wave Propagation in Laterally Varying Media-II. L_g-Waves in North-Western Europe, *Geophys. J. R. Astr. Soc.*, **79**, 257–267.

Kennett, B. L. N., (1986). L_g Waves and Structural Boundaries, *Bull. Seismol. Soc. Am.*, **76**, 1133–1142.

Knopoff, L., Hudson, J. A., (1964). Transmission of Love Waves Past a Continental Margin, *J. Geophys. Res.*, **69**, 1649–1653.

Knopoff, L., Mal, A. K., (1967). Phase Velocities of Surface Waves in the Transition Zone of Continental Margins-I. Love Waves, *J. Geophys. Res.*, **72**, 1769–1776.

Knopoff, L., Mal, A. K., Alsop, L. E., Phinney, R. A., (1970). A Property of Long-Period Love Waves, *J. Geophys. Res.*, **75**, 4084–4086.

Knopoff, L., Schwab, F., Nakanishi, K., Chang, F., (1975). Evaluation of L_g as a Discriminant among Different Continental Crustal Structures, *Geophys. J. R. Astr. Soc.*, **39**, 41–70.

Knopoff, L., Schwab, F., Kausel, E., (1973). Interpretation of L_g, *Geophys. J. R. Astr. Soc.*, **33**, 389–404.

Kovach, R. L., Anderson, D. L., (1964). Higher Mode Surface Waves and Their Bearing on the Structure of the Earth's Mantle, *Bull. Seismol. Soc. Am.*, **54**, 161–182.

Le Douaran, S., Burrus, J., Avedik, F., (1984). Deep Structure of the North-Western Mediterranean Basin: Results of a Two-Ship Survey, *Marine Geology*, **55**, 325–345.

Lehmann, I., (1952). On Short Period Surface Wave L_g and Crustal Structures. *Bull. D'information L'UGGI 2e Aneé*, 248–251.

Lehmann, I., (1957). On L_g as read in North American Records, *Annali di Geofisica*. **10**, 1–28.

Lysmer, J., Drake, L. A., (1971). The Propagation of Love Waves across Nonhorizontally Layered Structures, *Bull. Seismol. Soc. Am.*, **61**, 1233—1251.

Lysmer, J., Drake, L. A., (1972). A Finite Element Method for Seismology, Ch. 6 in *Methods in Computational Physics 11, Seismology*, Alder, B., Fernbach, S., Bolt, B. A., editors, Academic Press.

Martel, L., (1980). Love Wave Propagation Across a Step by Finite Elements and Spatial Filtering, *Geophys. J. R. Astr. Soc.*, **61**, 639–677.

Mantovani, E., Schwab, F., Liao, H., Knopoff, L., (1977). Generation of Complete Theoretical Seismograms for SH-II, *Geophys. J. R. Astr. Soc.*, **48**, 531–535.

Nicolas, M., Massinon, B., Mechler, P., Bouchon, M., (1982). Attenuation of Regional Phases in Western Europe, *Bull. Seismol. Soc. Am.*, **72**, 2089–2106.

Nuttli, O. W., (1973). Seismic Wave Attenuation and Magnitude Relations for Eastern North America, *J. Geophys. Res.*, **78**, 876–885.

Nuttli, O. W., (1978). A Time Domain Study of the Attenuation of 10-Hz Waves in the New Madrid Seismic Zone, *Bull. Seismol. Soc. Am.*, **68**, 343–355.

Nuttli, O. W., (1981). On the Attenuation of L_g Waves in Western and Central Asia and Their Use as a Discriminant between Earthquakes and Explosions, *Bull. Seismol. Soc. Am.*, **71**, 249–261.

Oliver, J., Dorman, J., Sutton, G., (1959). The Second Shear Mode of Continental Rayleigh Waves, *Bull. Seismol. Soc. Am.*, **49**, 379–389.

Oliver, J., Ewing, M., Press, F., (1955). Crustal Structure of the Arctic Regions from the L_g Phase, *Bull. Seismol. Soc. Am.*, **66**, 1063–1074.

Oliver, J., Ewing, M., (1957). Higher Modes of Continental Rayleigh Waves, *Bull. Seismol. Soc. Am.*, **47**, 187–204.

Oliver, J., Ewing, M., (1958). Normal Modes of Continental Surface Waves, *Bull. Seismol. Soc. Am.*, **48**, 33–49.

Panza, G. F., Calcagnile, G., (1974). Comparison of Multimode Surface Wave Response in Structures With and Without a Low Velocity Channel (Part I: Dip Slip Sources on a vertical Fault Plane), *Pure Appl. Geophys.*, **112**, 583–596.

Panza, G. F., Calcagnile, G., (1975). L_g, L_i and R_g from Rayleigh Modes. *Geophys. J. R. Astr. Soc.*, **40**, 475–487.

Pec, K., (1967). Theoretical Dispersion Tables for Love Waves Propagating in a Wedge and in a Single Nonhomogeneous Layer with a Linear Velocity Gradient. *Pub. of Dominion Obs. Ottawa*, **35**.

Pomeroy, P. W., Best, W. J., McKevilly, T. V., (1982). Test Ban Treaty verification with Regional Data: A Review, *Bull. Seismol. Soc. Am.*, **72**, s89–s129.

Press, F., (1956). Velocity of L_g Waves in California, *Trans. A. G. U.*, **37**, 615–618.

Press, F., Ewing, M., (1952). Two Slow Surface Waves across North America. *Bull. Seismol. Soc. Am.*, **42**, 219–228.

Press, F., Ewing, M., Oliver, J., (1956). Crustal Structure and Surface-Wave Dispersion in Africa, *Bull. Seismol. Soc. Am.*, **46**, 97–103.

Regan, J., (1987). Numerical Studies of Propagation of L_g Waves across Ocean Continent Boundaries Using the Representation Theorem, *Ph. D. Thesis, California Institute of Technology, Pasadena, Ca.*

Sato, R., (1961a). Love Waves Propagated across Transitional Zone, *Japan J. Geophys., vol. 2*, 117–134.

Sato, R., (1961b). Love Waves in Case the Surface Layer is Variable in Thickness. *J. Phys. Earth.*, **9**, 19–36.

Savarensky, E., Valdner, N., (1960). Observations of L_g and R_g Waves from the Black Sea Basin Earthquakes, *Annali di Geofisica*, **13**, pp. 129–134.

Schwab, F., Kausel, E., Knopoff, L., (1974). Interpretation of S_a for a Shield Structure. *Geophys. J. R. Astr. Soc.*, **36**, 737–742.

Singh, S., Herrmann, R. B., (1983). Regionalization of Crustal Coda Q in the Continental United States, *J. Geophys. Res.*, **88**, 527–538.

Stephens, C., Isacks, B. L., (1977). Toward an Understanding of S_n: Normal Modes of Love Waves in an Oceanic Structure, *Bull. Seismol. Soc. Am.*, **67**, 69–78.

Street, R., (1976). Scaling Northeastern United States/Southeastern Canadian Earthquakes by Their L_g Waves, *Bull. Seismol. Soc. Am.*, **66**, 1525–1537.

Street, R., (1984). Some Recent L_g Phase Displacement Spectral Densities and Their Implications with Respect to the Prediction of Ground Motions in Eastern North America, *Bull. Seismol. Soc. Am.*, **74**, 757–762.

Street, R., Herrmann, R. B., Nuttli, O. W., (1975). Spectral Characteristics of the L_g Wave Generated by Central United States Earthquakes *Geophys. J. R. Astr. Soc.*, **41**, 51–63.

Street, R., Turcotte, F. T., (1977). A Study of Northeastern North American Spectral Moments, Magnitudes, and Intensities, *Bull. Seismol. Soc. Am.*, **67**, 599–614.

Wetmiller, R. J., (1974). Crustal Structure of Baffin Bay from Earthquake Generated L_g Phases, *Can. J. Earth Sci.*, **11**, 123–130.

Zienkiewicz, O. C., Cheung, ., (1967). *The Finite Element Method in Structural and Continuum Mechanics*, McGraw-Hill.

TABLE 1
GRID CHARACTERISTICS FOR TRANSITION MODELS

	nx	nz	nt	T_{mcalc}	A	B	C	D	E
model	# nodes		$\#\Delta t$	s	# nodes				
0f	310	90	1921	96	230	240	240	240	250
25f	365	90	2101	105	240	250	275	300	310
50f	525	90	3101	155	350	360	410	460	470
100f	500	90	2441	122	250	260	360	460	470
0r	350	90	2561	128	275	285	285	285	295
25r	400	90	2501	125	275	285	310	335	345
50r	450	90	2601	130	275	285	335	385	395
100r	525	90	2941	147	275	285	385	485	495
fref	530	90	3201	160					
rref	525	90	3201	160					

Figure 1: Types of models used in studies of propagation of Love waves across continent ocean boundaries, in order of increasing complexity. a) shows two homogeneous layered regions, 1 and 3, separated by an intermediate region, 2, in which elastic properties vary smoothly between their values in regions 1 and 2. b) shows a layer over a half-space with a step change in the thickness of the layer. c) shows a model with a smooth change in thickness, either at the surface or the Moho. d) shows a model with a smooth change in thickness both at the surface and the Moho. The variations in a), c), and d) occur in a transition region of length L.

Figure 2: Geometry used to explain the coupling of PM seimograms from a source outside a FE grid into a FE grid. The two long horizontal lines show the free surface and the boundary between the layer and the half-space. The source is shown as an asterisk. Two columns of FE nodes are shown as dots. The vertical line connecting the dots and the short horizontal line perpendicular to it are grid edges. The heavy solid line from the source to the surface receiver in the grid denotes the direct analytic seismogram, the solid lines between the source and the grid edge nodes denote the direct forcing functions, and the dotted lines indicate the source to receiver paths, for the sources created by the application of the forcing functions at the grid edge. Integration over all dashed paths gives the hybrid seismogram

Figure 3: Sample PM mode sum synthetic seismogram for SH L_g 1500 km from the source. The seismogram includes modes with periods between 0.5 sec and 100 sec. The fundamental and the first five higher modes are used. The seismogram has been band pass filtered between 0.01 and 1 hz, and has the WWSSN short period instrument has been convolved with it. The box labeled input window shows the time window used to select the forcing function. The numbers along the axis indicate the group velocities of the arrivals.

Figure 4: Explanation of terms and illustration of the model classes used to describe the behavior on passage through a transition region. The heavy line between the water layer and the crustal layer is the surface. The sloping portion of this surface is the continent to ocean boundary (COB) for the C/O transition model and the ocean to continent boundary (OCB) for the O/C transition model. Similarly, the sloping dashed line between the crust and mantle layers is the crust to mantle boundary (CMB) for the C/O transition and the mantle to crust boundary (MCB) for the O/C case. The length of the transition, L, is the distance from B to D, B is referred to as the beginning of the transition, D as the end of the transition, C as the center of the transition. A is 5 km from B, E is 5 km from D.

Figure 5: Seismograms recorded at the surface for X2=1520 and 1540 km. The first seismogram in each group is a direct synthetic, the second is a hybrid synthetic determined using the long grid (200x100), the third and fourth are hybrid synthetics determined using a short (100x100) grid with and without the BC respectively. The number beside each of the hybrid synthetics is the RMS amplitude ratio between that hybrid seismogram and the direct synthetic. Seismograms have been band pass filtered between .01 and 1 Hz and have been convolved with the short period WWSSN instrument. Arrival times of the single and multiple reflections are indicated by the arrows below each group of seismograms.

Figure 6: Time slices recorded during the 25 km C/O transition calculation. The crustal layer and the ends and bottom of the FE grid which contain it are outlined. A larger displacement produces a larger point. Thus, high displacement areas appear darker. Sixty forcing functions were used. The time since the initiation of the FE calculation is shown above the right end of each grid. The arrow above a time slice shows the location to which the disturbances moving at 3.5 km/sec, seen at the left end of the previous time slice, have moved in the intervening duration.

Figure 7: Surface section of seismograms recorded for a 25 km C/O transition calculation. The numbers to the left of each seismogram indicate the location of the node at which that seismogram is recorded. Seismogram 1 was recorded at B, seismogram 11 at D. The numbers increase as one moves farther from the source. The spacing between receivers in the transition zone is uniform. The numbers above the right end of each seismogram give the 60s RMS amplitude of that seismogram.

Figure 8: Variation in RMS surface amplitude with distance, X2, from the source for each C/O transition calculation (upper sketch, 60 second RMS), and for each O/C transition calculation (lower sketch, 50 second RMS). RMS amplitude is the y coordinate. The two vertical lines, labeled B and D, indicate the limits of the transition region. Outside the transition region the scale is uniform. The distance scale (x coordinate) in the transition region is different for each L. Within the transition region all distances are plotted with respect to an origin at B, as fractions of L. Each line, labelled with the L it represents, was generated using RMS measurements at intervals of 5 km along the crustal surface.

Figure 9: Depth sections of seismograms recorded at B and D for a 25 km C/O transition calculation. The numbers above the right end of each seismogram show the 60s RMS amplitude. Successive rows show pairs of receivers at increasing depths. The first row of seismograms shows receivers at the depth of the surface of the continental crust, the second row receivers at the depth of the surface of the oceanic crust, the third row receivers at the depth of the base of the oceanic crust, the fifth row receivers at the depth of the base of the continental crust, and the fourth row receivers midway between the third row and the fifth row.

Figure 10: Variation of 55 second RMS amplitude with depth on depth sections A, B, C, D, E, of Figure 4, and F, located 10 km beyond E, for each C/O transition model. Each plot illustrates results for one depth section. The letter at the upper left of each plot identifies the location of the depth section. Amplitudes for the surface node and nodes equally spaced down the depth section (Δz = 2.5 km) are shown. The three solid horizontal lines are, from top to bottom, the surface and base of the oceanic crustal layer, and the base of the continental crustal layer. The dashed horizontal line shows the depth of the base of the crustal layer in depth section C, at the center of the transition region.

Figure 11: Illustration of ray paths within a 25 km and a 100 km C/O transition structure. Diagrams are drawn to scale. Each diagram shows rays with angles of incidence, i, 55°, 65°, and 75°, at the free surface and crust mantle interface in the continental portion of the model. These angle sample the possible range of post-critical incident angles (> 51/*circ*). The incident angle, j_n, and the transmission angle, j'_n, at the crustal boundaries in the transition regions are labeled. The upper diagram in each pair shows propagation paths for rays that encounter the CMB before the COB. The lower diagram shows propagation paths for rays that encounter the COB before the CMB. The arrows indicate the direction of propagation of the wavefront along the ray.

Figure 12: Time slices recorded during the 50 km O/C transition calculation. Details are identical to Figure 7. 40s RMS amplitudes are shown.

Figure 13: Surface section of seismograms recorded for a 50 km O/C transition calculation. Details explained in Figure 8.

Figure 14: Variation of 55 second RMS amplitude with depth. Details are as explained in Figure 10.

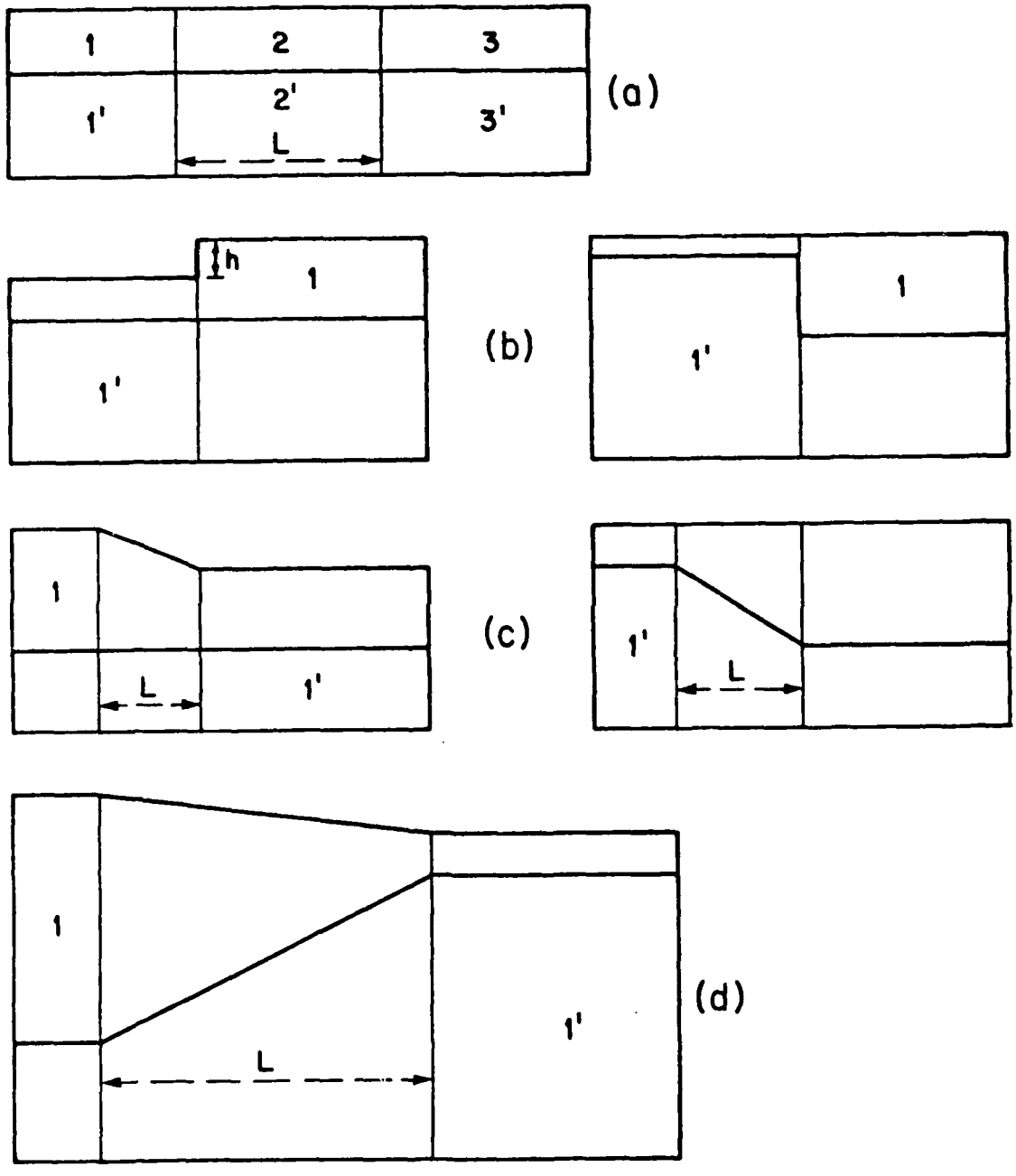

Figure 1

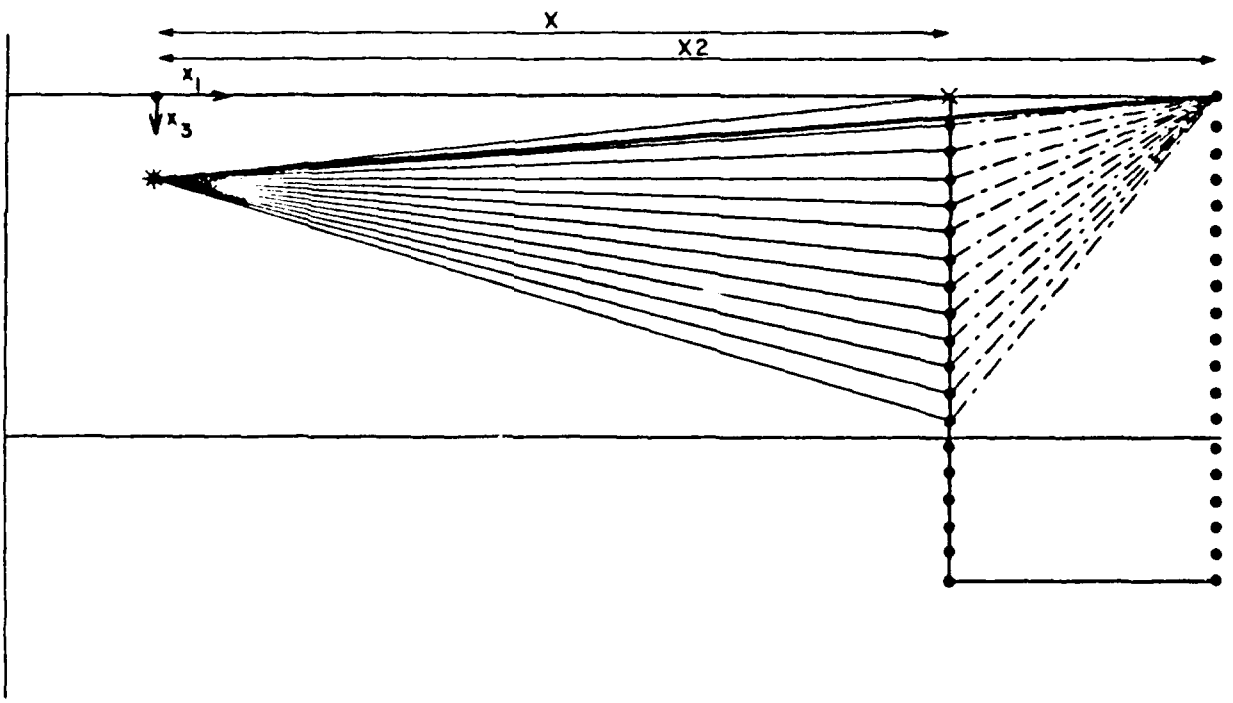

Figure 2

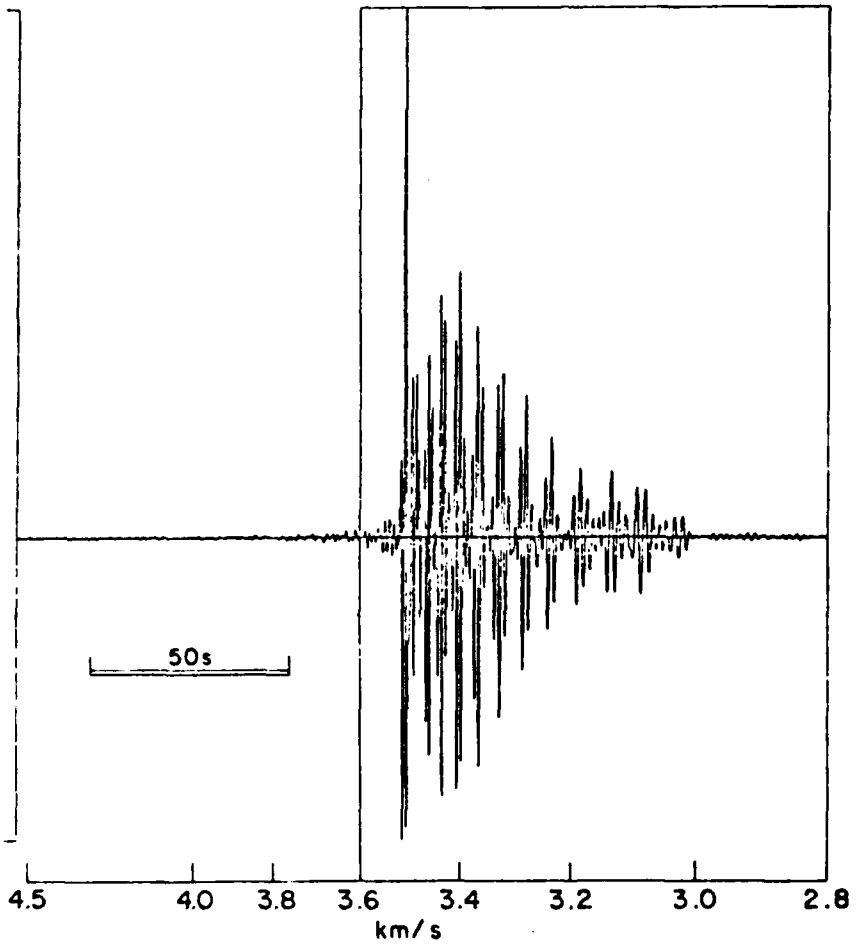

Figure 3

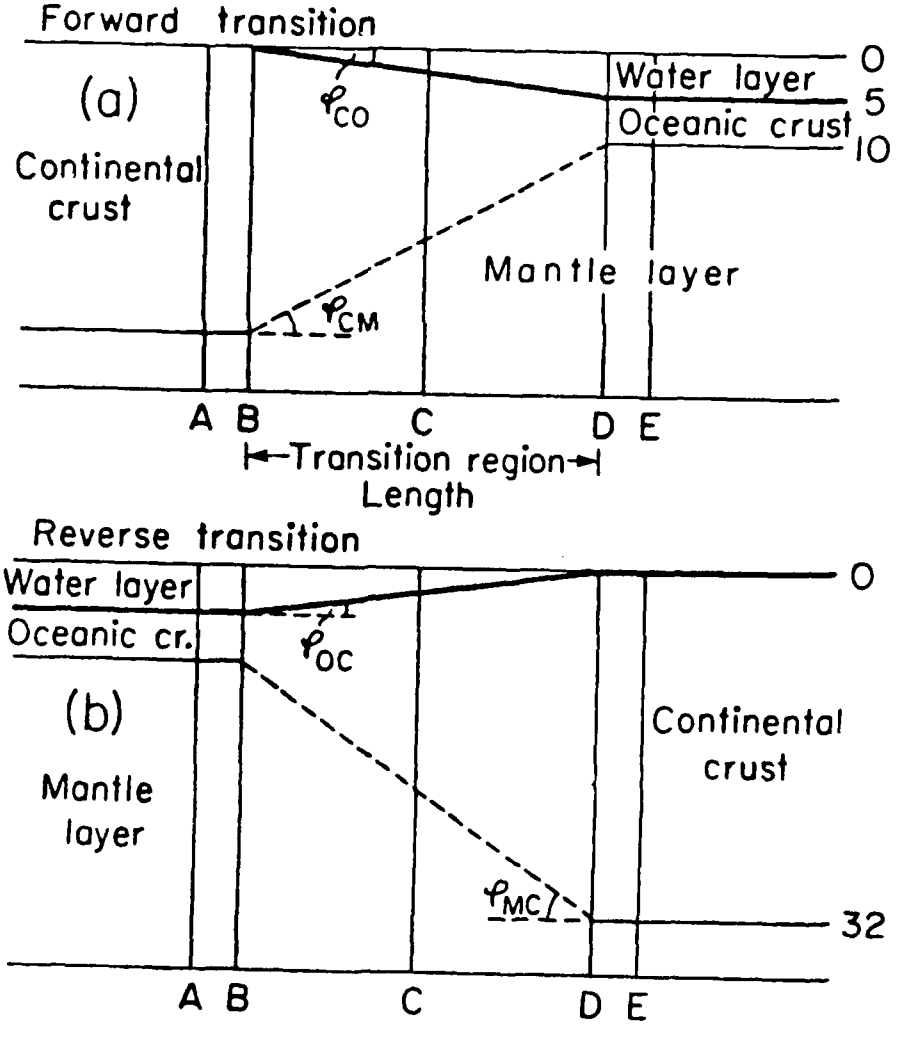
Forward transition
(a)
Continental crust
φ_{CO}
Water layer
Oceanic crust
0
5
10
Mantle layer
φ_{CM}
A B C D E
Transition region
Length
Reverse transition
Water layer
Oceanic cr.
φ_{OC}
(b)
Mantle layer
Continental crust
φ_{MC}
0
32
A B C D E

Figure 4

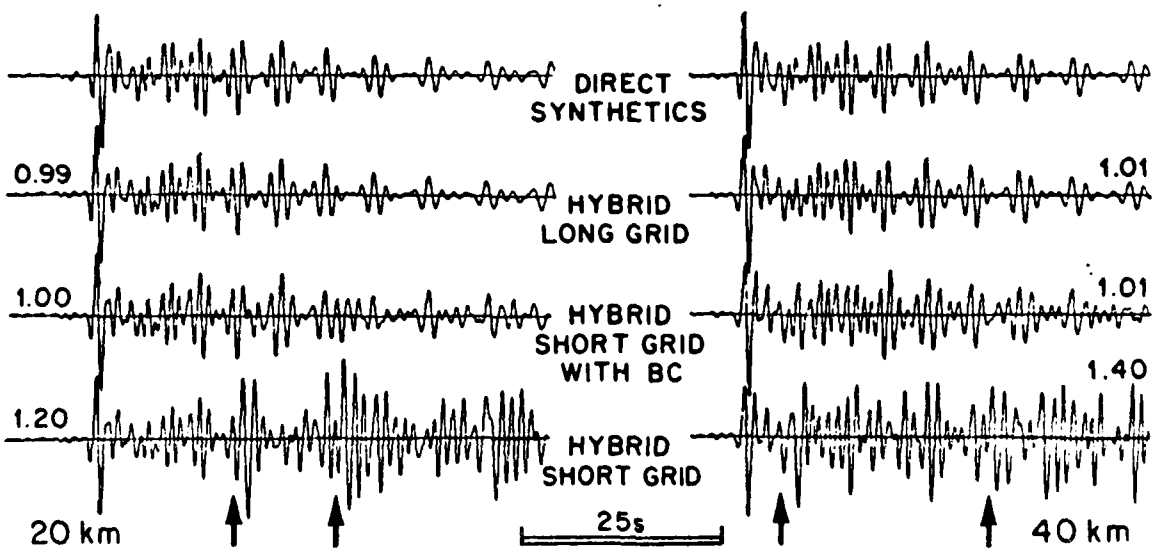
DIRECT
SYNTHETICS
0.99
HYBRID
LONG GRID
1.01
1.00
HYBRID
SHORT GRID
WITH BC
1.01
1.20
HYBRID
SHORT GRID
1.40
20 km
25s
40 km

Figure 5

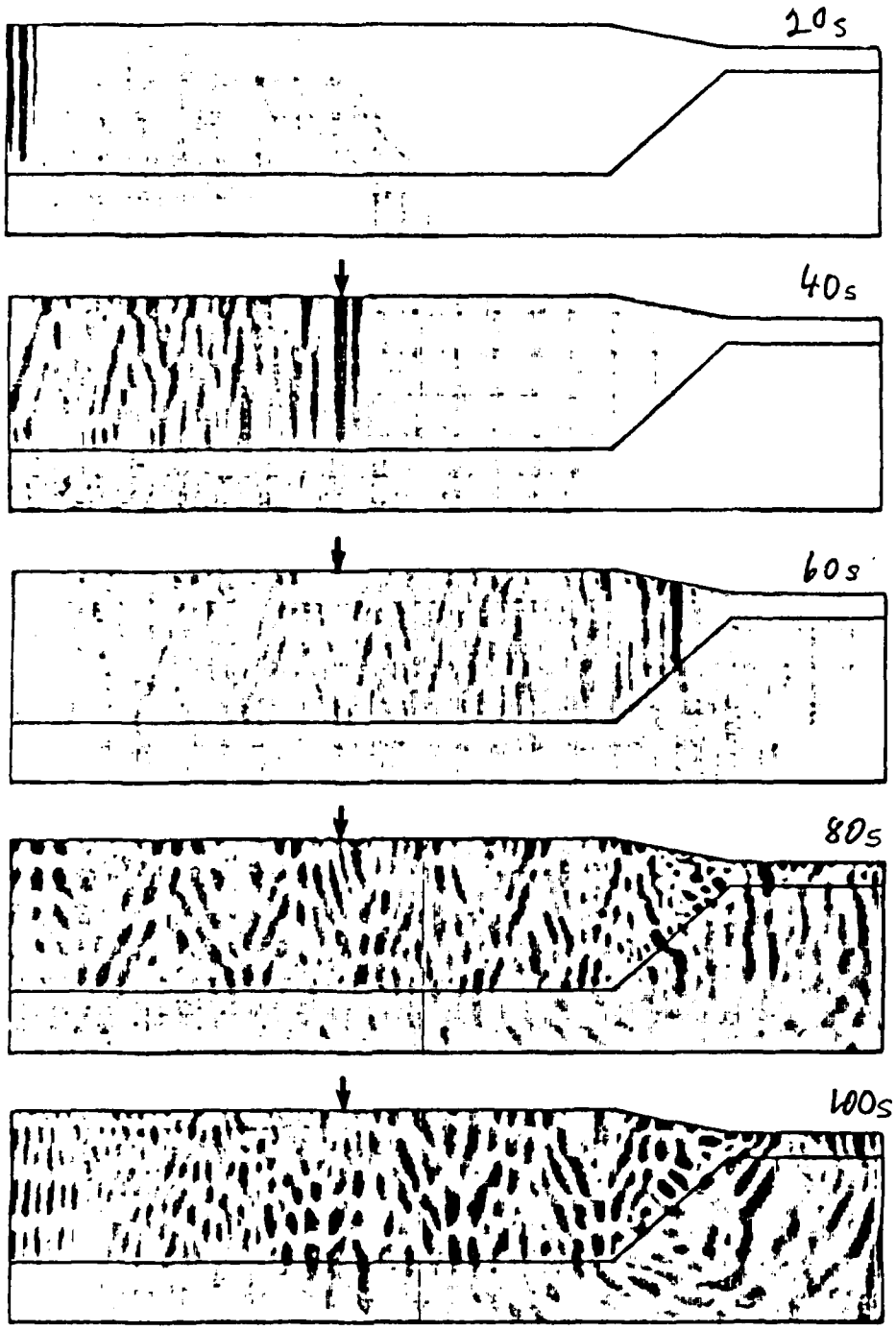

Figure 6

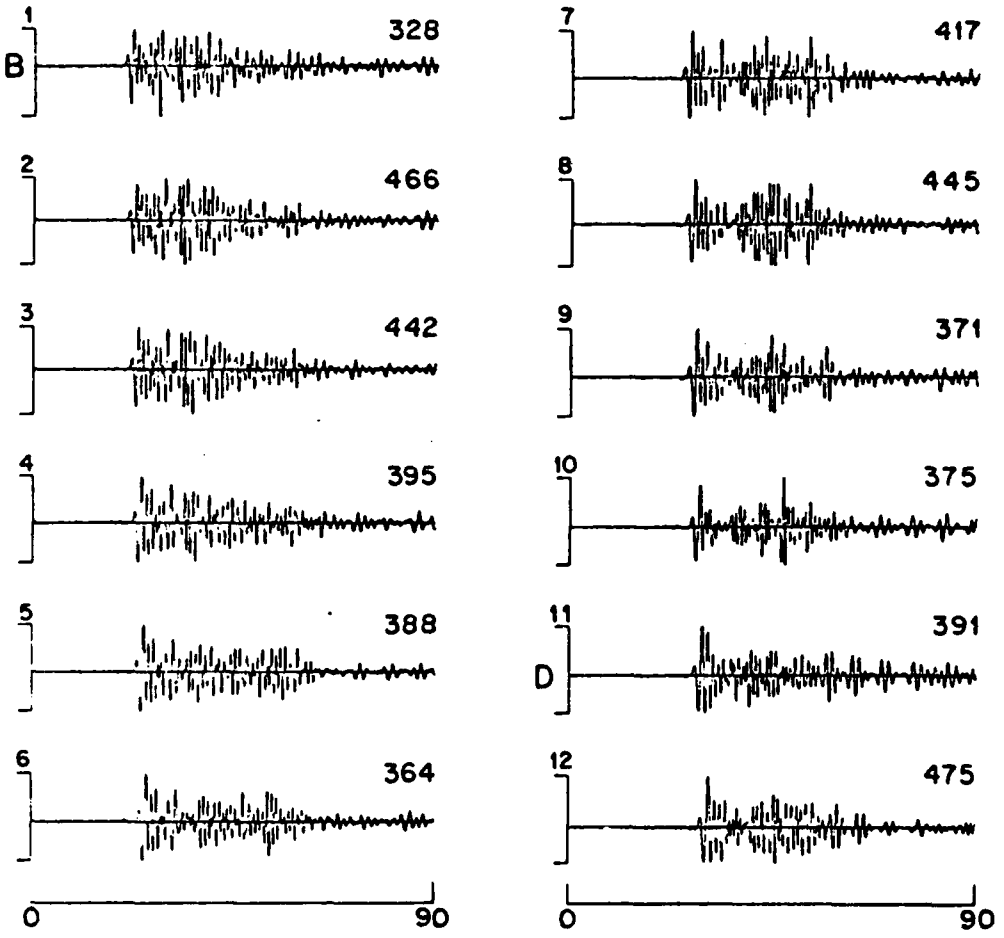
1
B
328
2
466
3
442
4
395
5
388
6
364
0
90
7
417
8
445
9
371
10
375
11
D
391
12
475
0
90

Figure 7

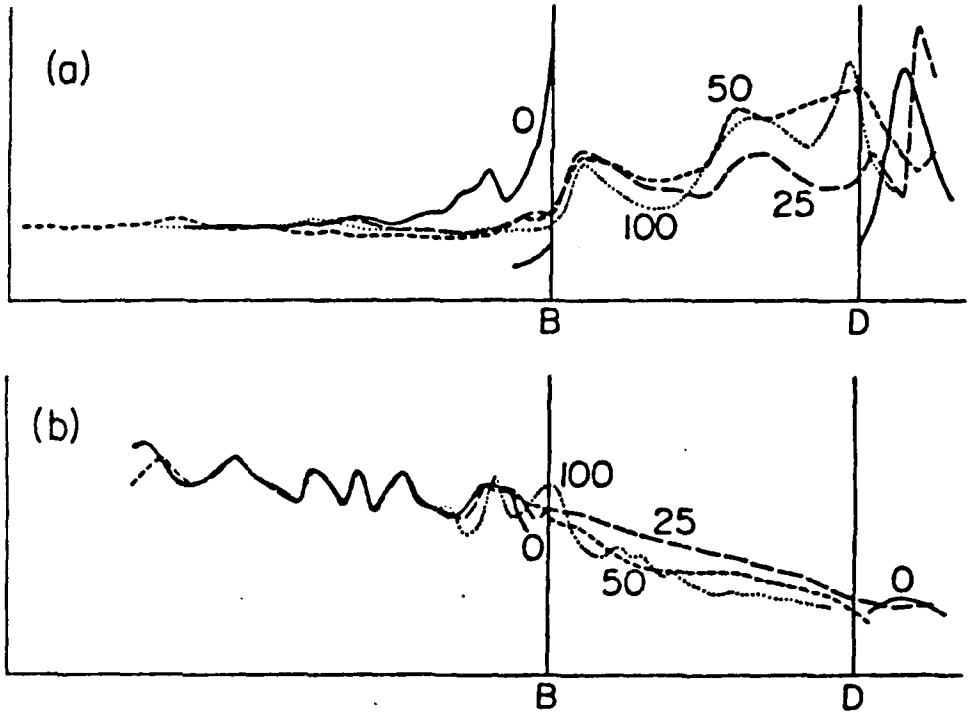

Figure 8

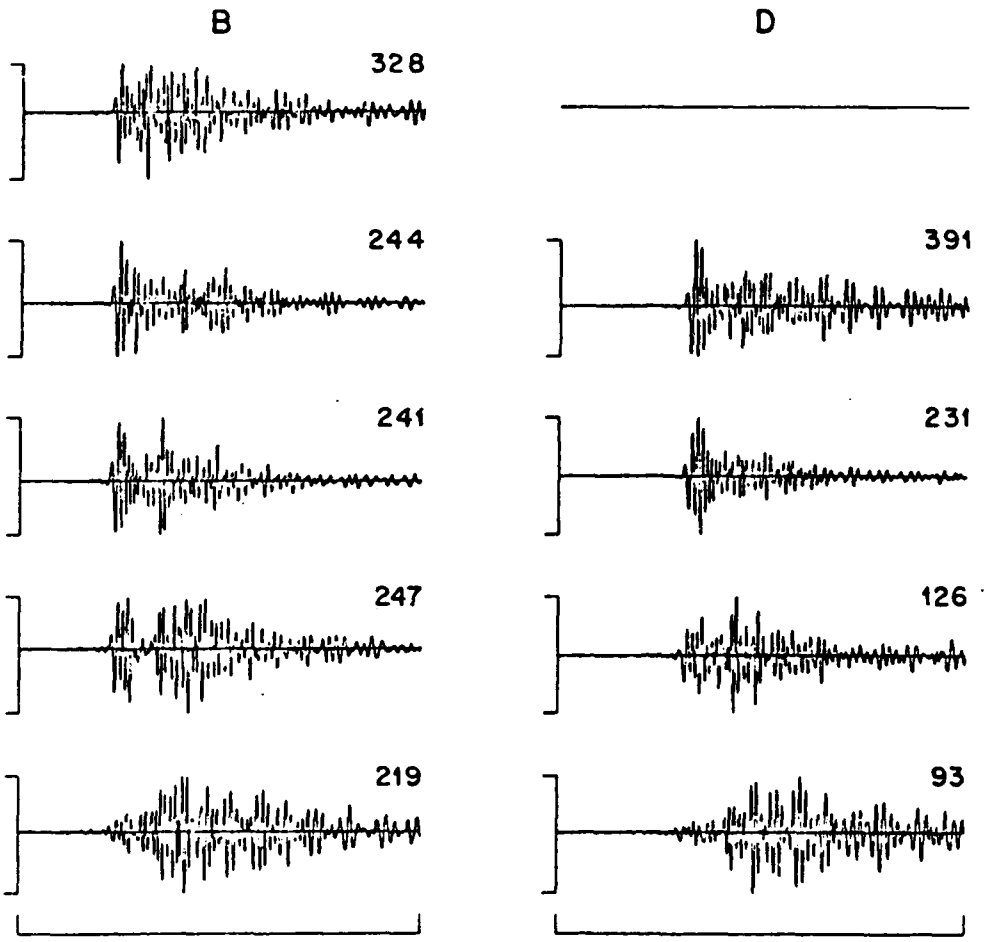

Figure 9

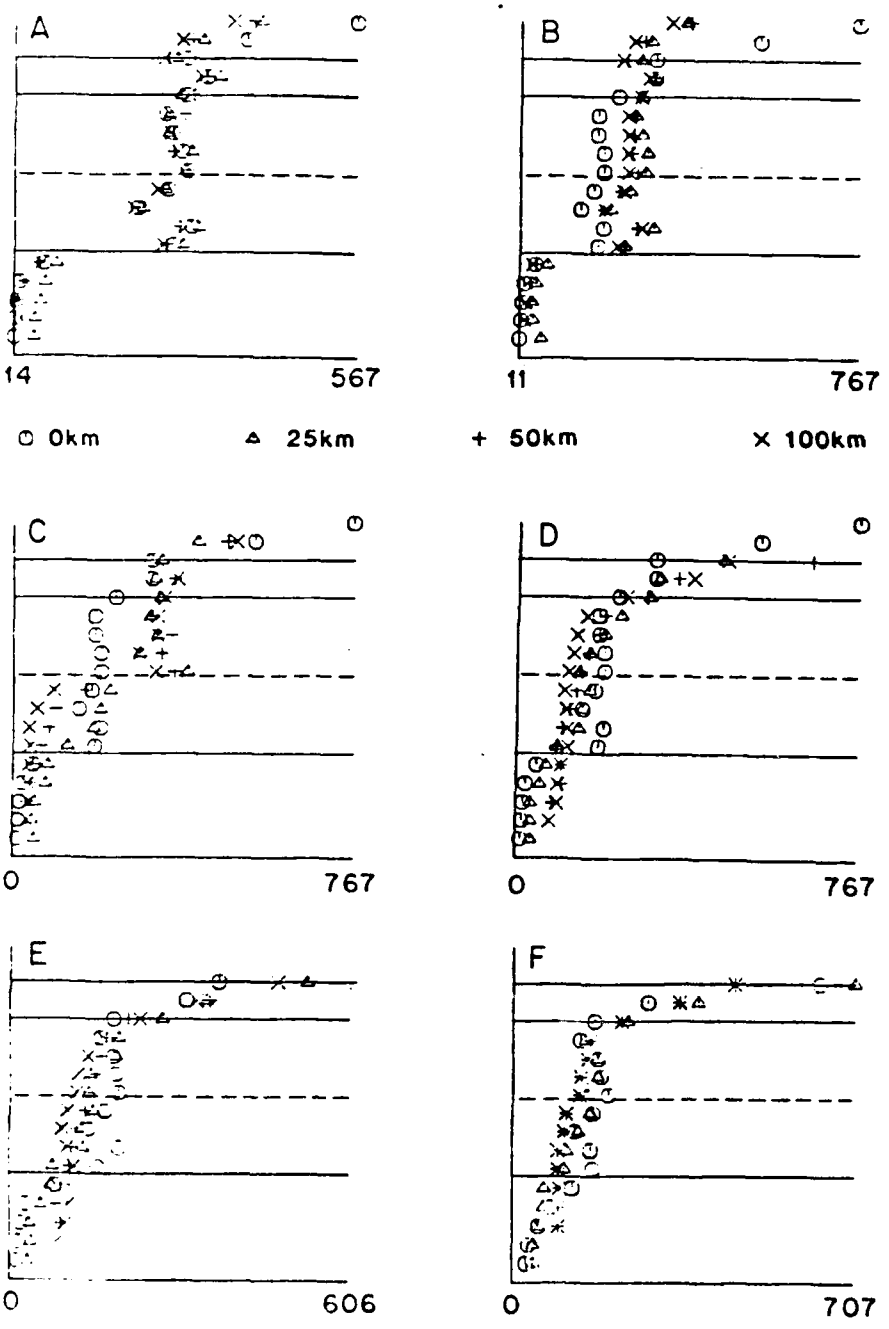
A
B
14
567
11
767
0 0km
Δ 25km
+ 50km
× 100km
C
D
0
767
0
767
E
F
0
606
0
707

Figure 10

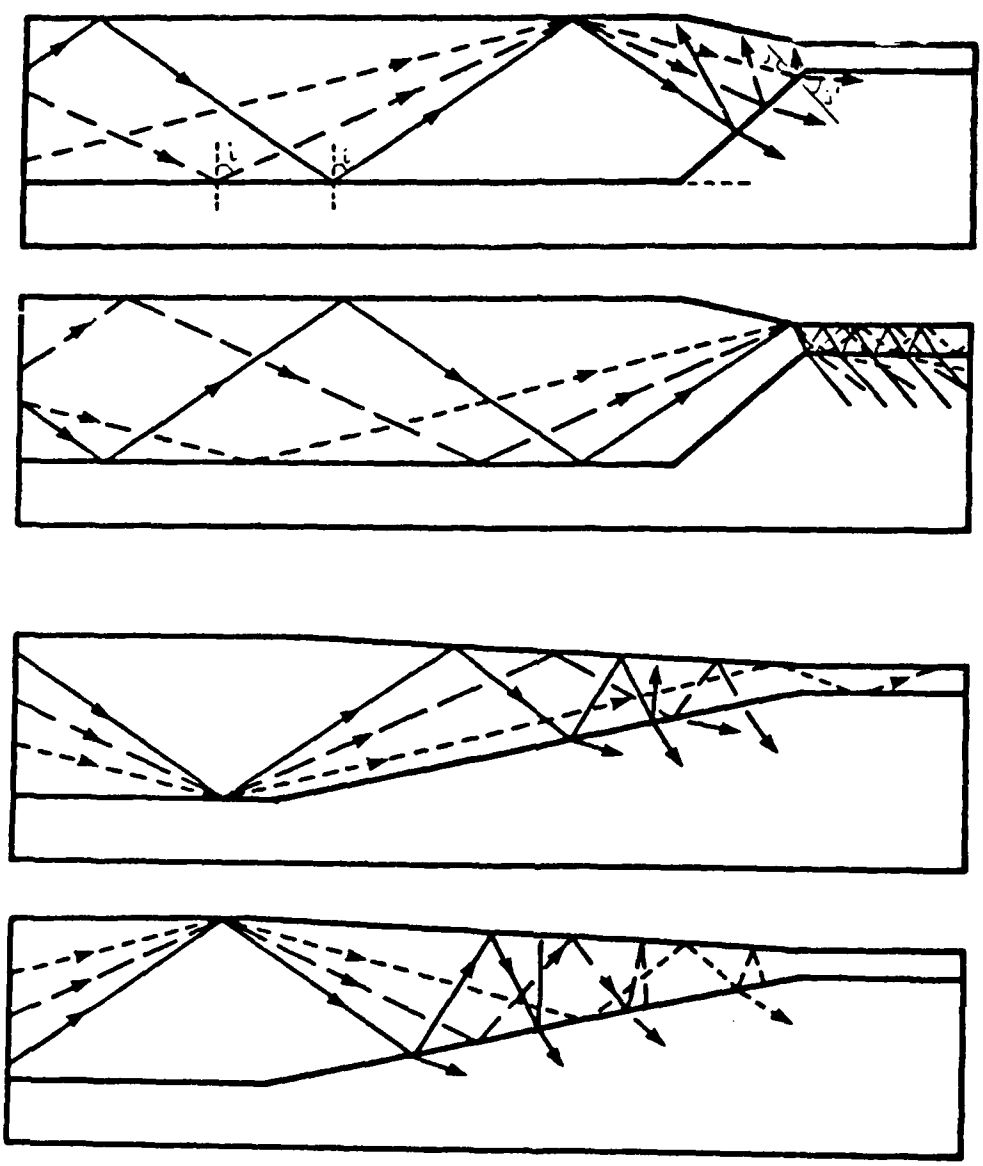

Figure 11

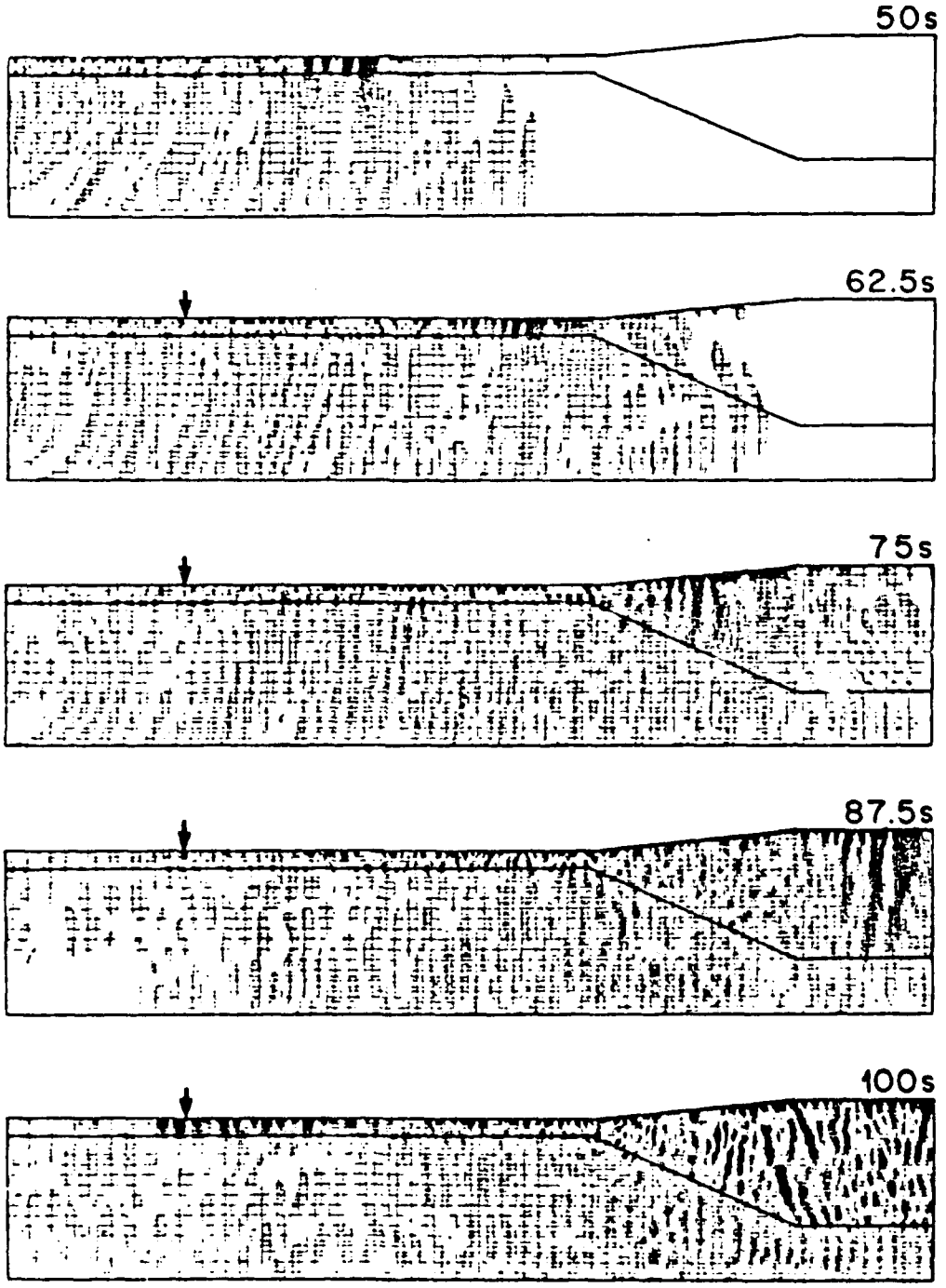

Figure 12

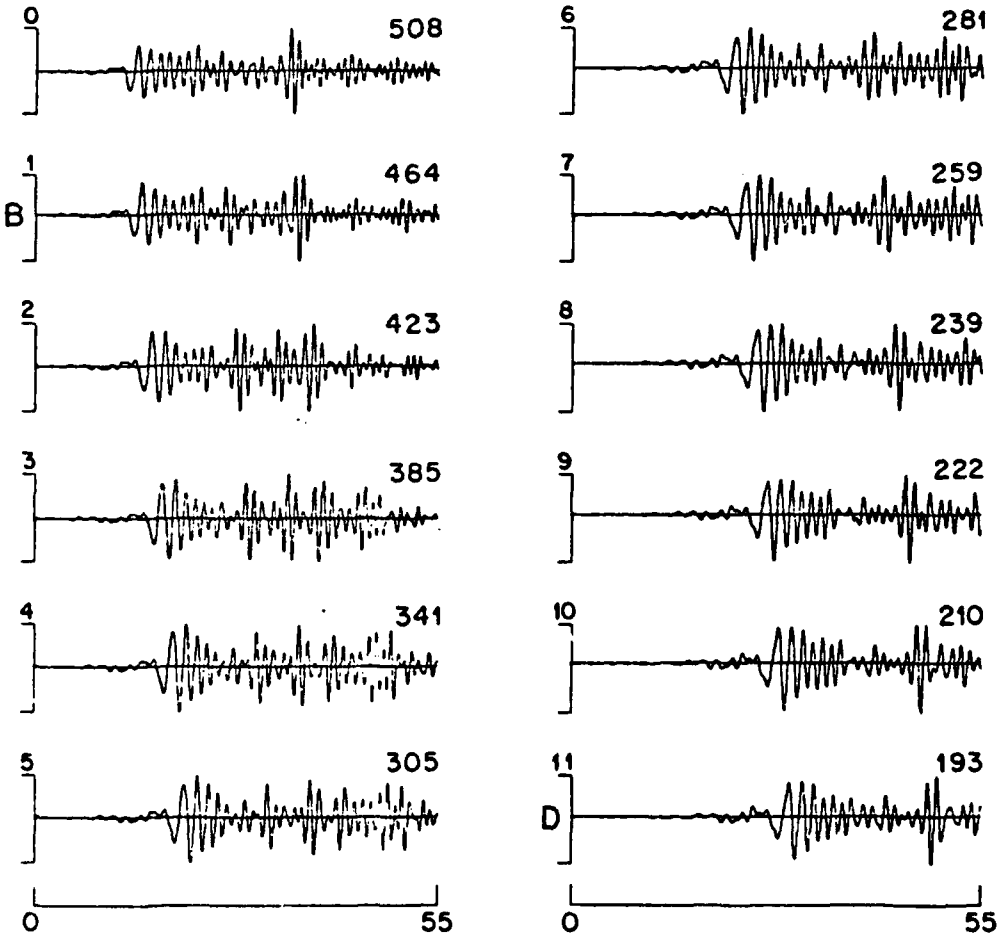
0
508
6
281
1
B
464
7
259
2
423
8
239
3
385
9
222
4
341
10
210
5
305
11
D
193
0
55
0
55

Figure 13

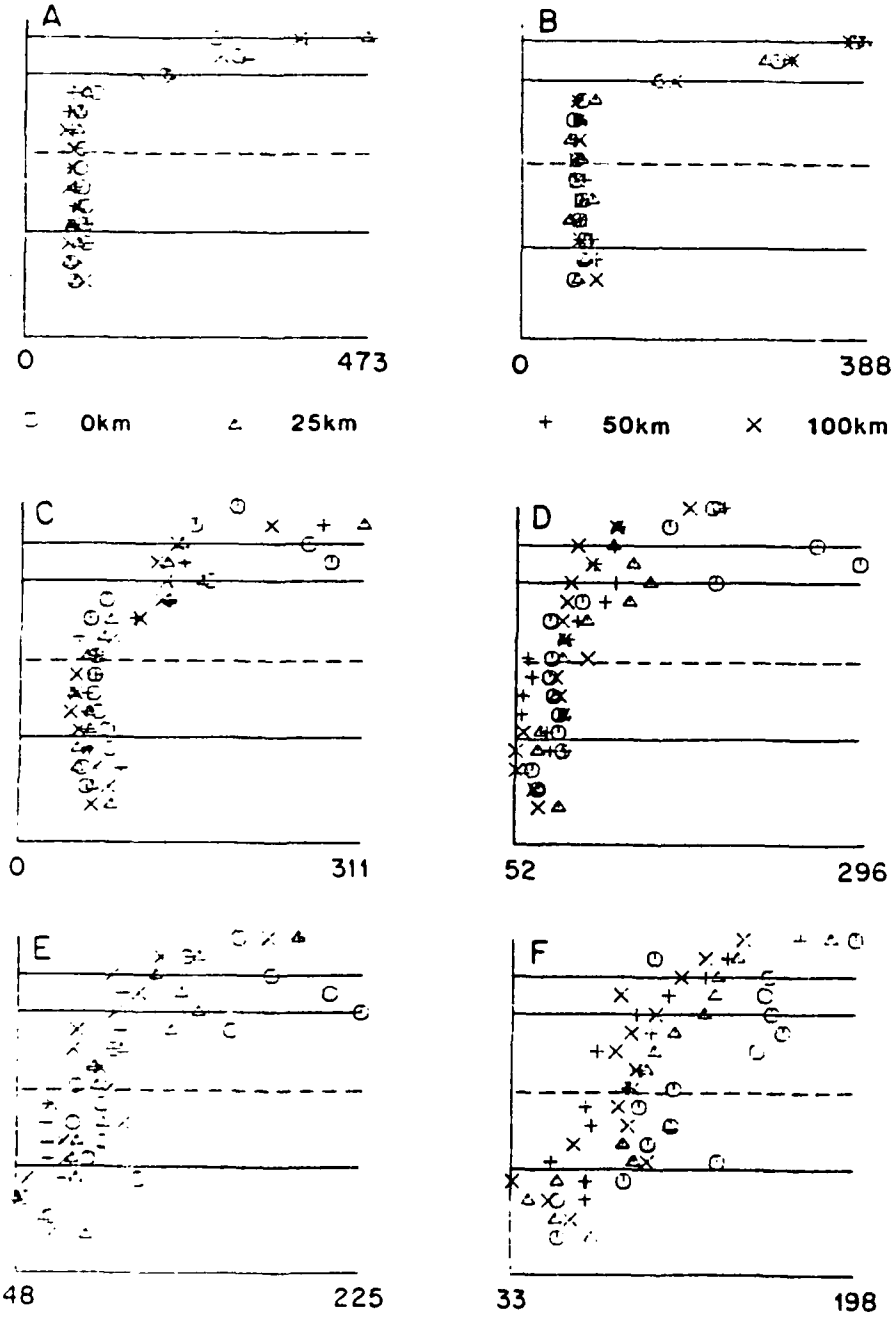

Figure 14

Modeling regional Love Waves: Imperial Valley to Pasadena

Phyllis Ho-Liu and Donald V. Helmberger

Abstract

Long period seismograms recorded at Pasadena of earthquakes occurring along a profile to Imperial Valley are studied in terms of source phenomena versus path effects. Some of the events have known source parameters, determined by teleseismic or near-field studies, and are used as master events in a forward modeling exercise to derive the Green's functions (SH displacements at Pasadena due to a pure strike-slip or dip-slip mechanism) that describe the propagation effects along the profile. Both timing and waveforms of records are matched by synthetics calculated from 2-dimensional velocity models. The best 2-dimensional section begins at Imperial Valley with a thin crust containing the basin structure and thickens towards Pasadena. The detailed nature of the transition zone at the base of the crust controls the early arriving shorter periods (strong motions) while the edge of the basin controls the scattered longer period surface waves. Shallow events in the basin are easily distinguished from deep events as well as the amount of strike-slip versus dip-slip motions involved from the waveform characteristics alone. Those events rupturing the sediments, such as the 1979 Imperial Valley earthquake, can be recognized easily by a late arriving scattered Love wave which has been delayed by the very slow path across the shallow valley structure.

Introduction

The major objectives of this paper are to initiate a field of study which will allow for the investigation of regional events at wavelengths shorter than their characteristic dimension and to provide a basis for source retrieval from sparsely recorded historic events. Thus, we will begin with a brief review of the types of seismograms available at the Seismological Laboratoryat Caltech for the last 50 years of recording and how they could be used to full advantage.

Presently, there are very few on-scale recordings of major earthquakes (magnitude > 5.8) at near-regional ranges of 10 to 500 km except for a small number of low-gain (gain = 100) Wood-Anderson (WA) type seismograms. Moderate earthquakes in southern California with magnitudes between 4 to 5.5 are usually recorded on one or more of the following instruments in Pasadena: 1. The normal WA instrument (T_o =0.8 sec.) with a gain of 2800. WA seismograms provide the basis for the Richter scale and the local magnitude, M_L; 2. The long-period (T_o = 6 sec.) torsion instrument which operates at a gain near 900; 3. The Press-Ewing (T_o = 30 sec.) instrument (LP 30-90) which operates at a gain of about 2250. The instrumental responses for these three systems are given in Figure 1. Two examples of the tangential component of the low-gain WA are

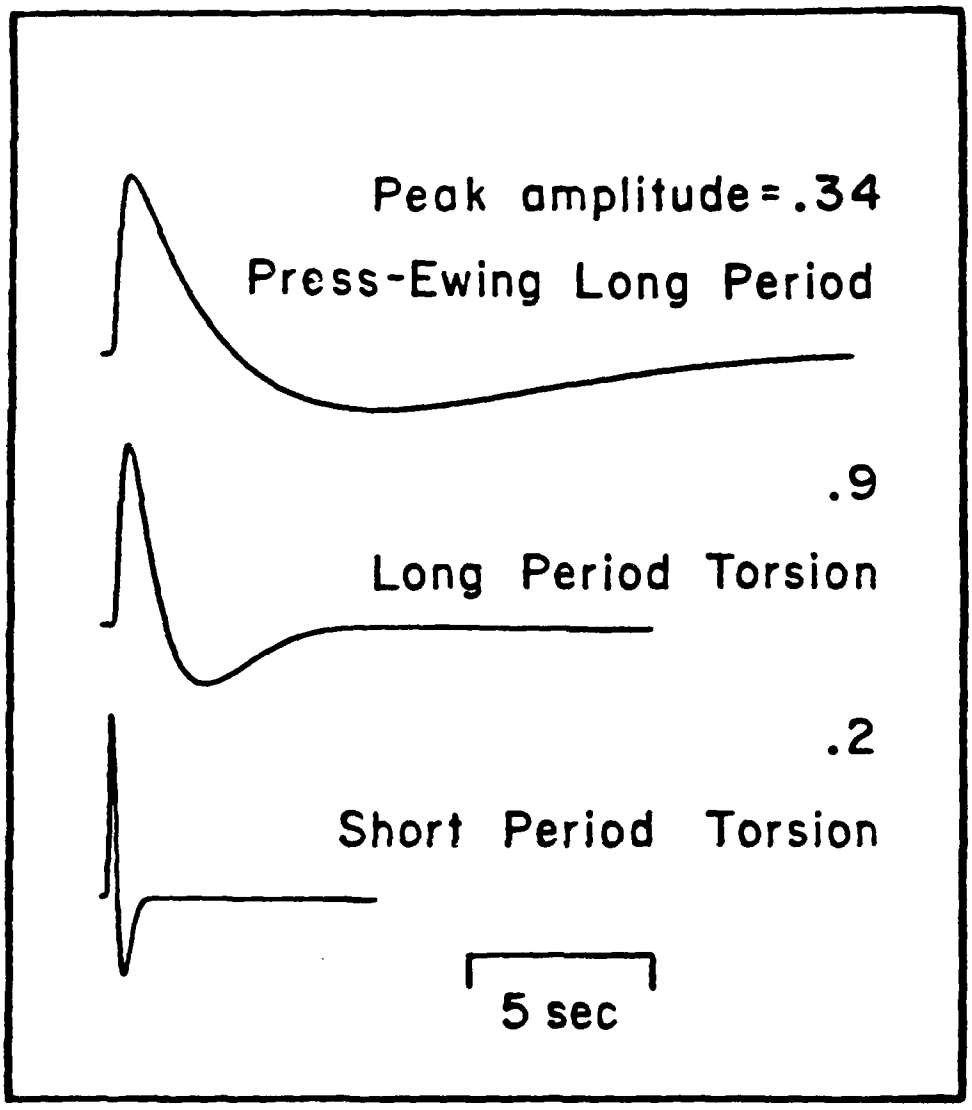

Figure 1. The instrument responses of the instruments recording the events used in this study.

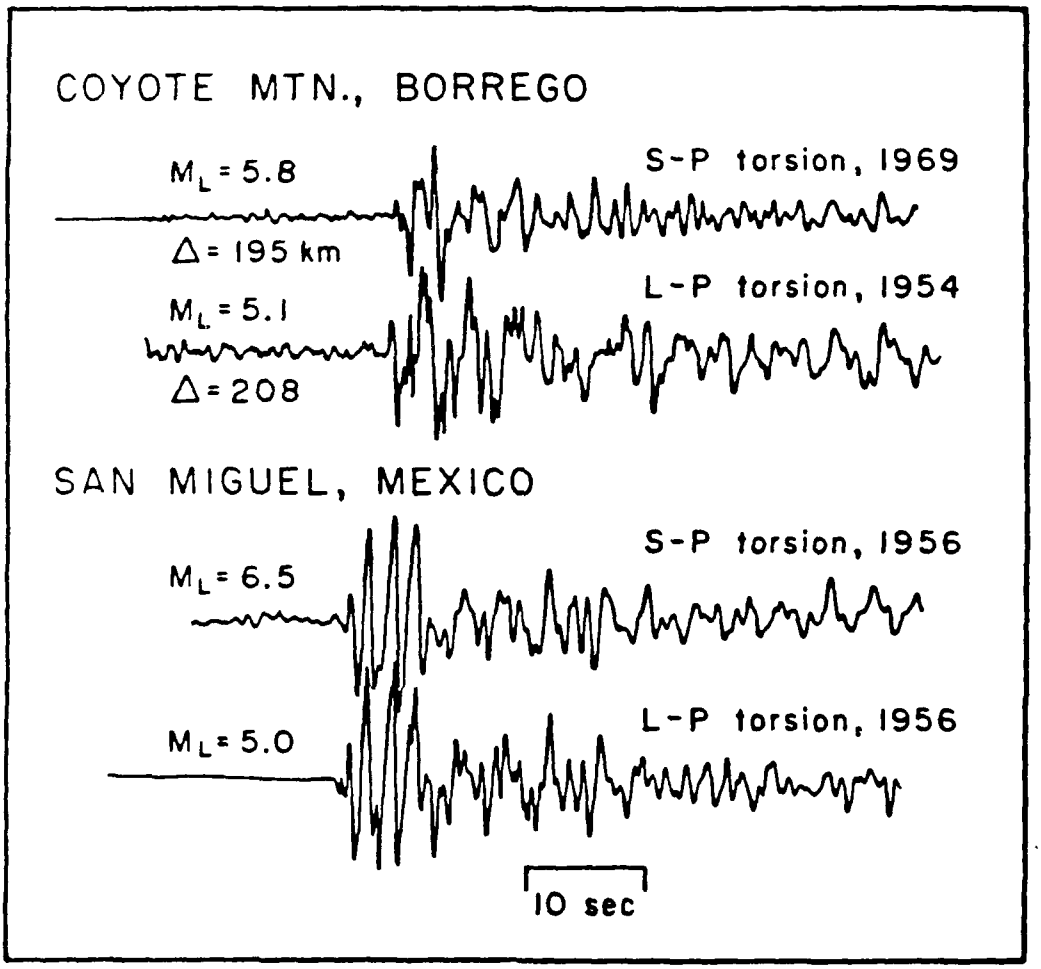

Figure 2. Comparison of aftershocks to main events on different Wood-Anderson (WA) torsion instruments. Top: 100X WA record of the Coyote Mountain event (filtered through a 0.5 sec. up and down triangle) and an aftershock of the 1954 Borrego Mountain earthquake recorded on the long-period WA instrument. Bottom: 100X WA record of the San Miguel earthquake and one of its aftershocks recorded on a high-gain (gain is about 900) long-period WA torsion instrument. (San Miguel records were provided by Joanne Yoshimura).

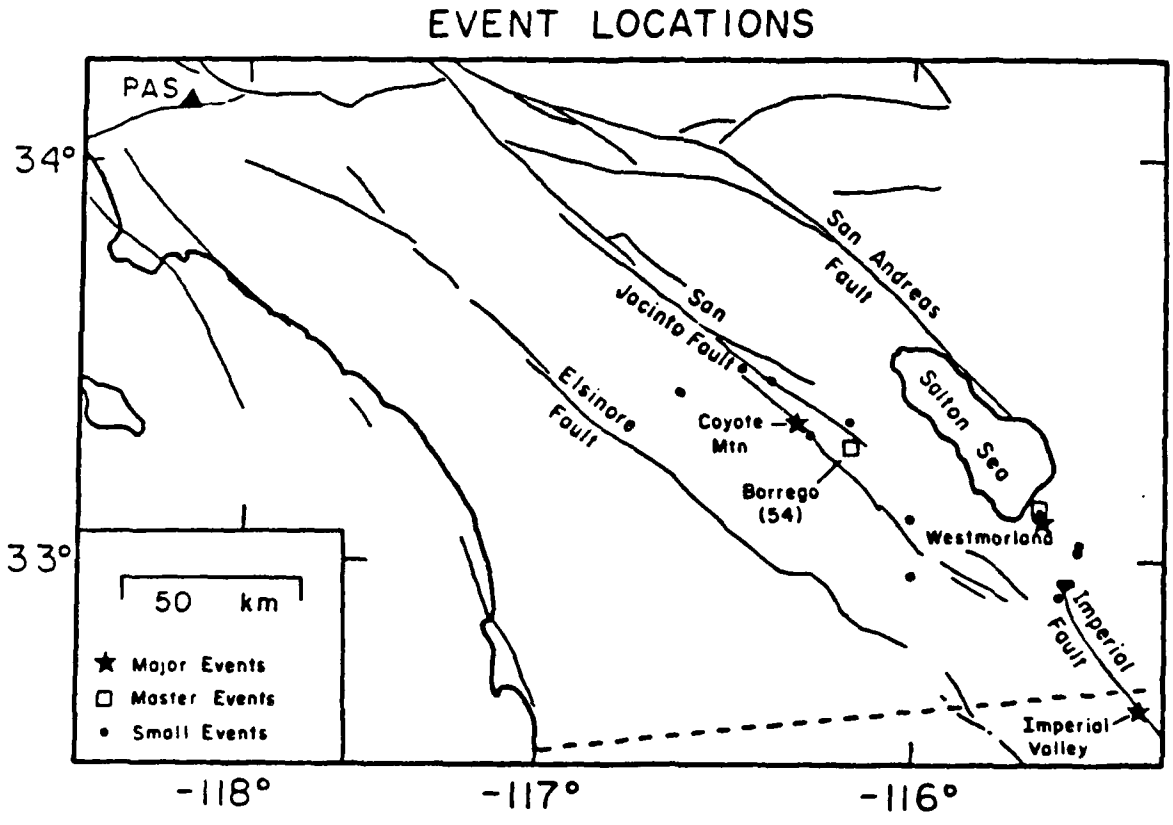

Figure 3. Map showing locations of Pasadena, PAS, and events used in this study.

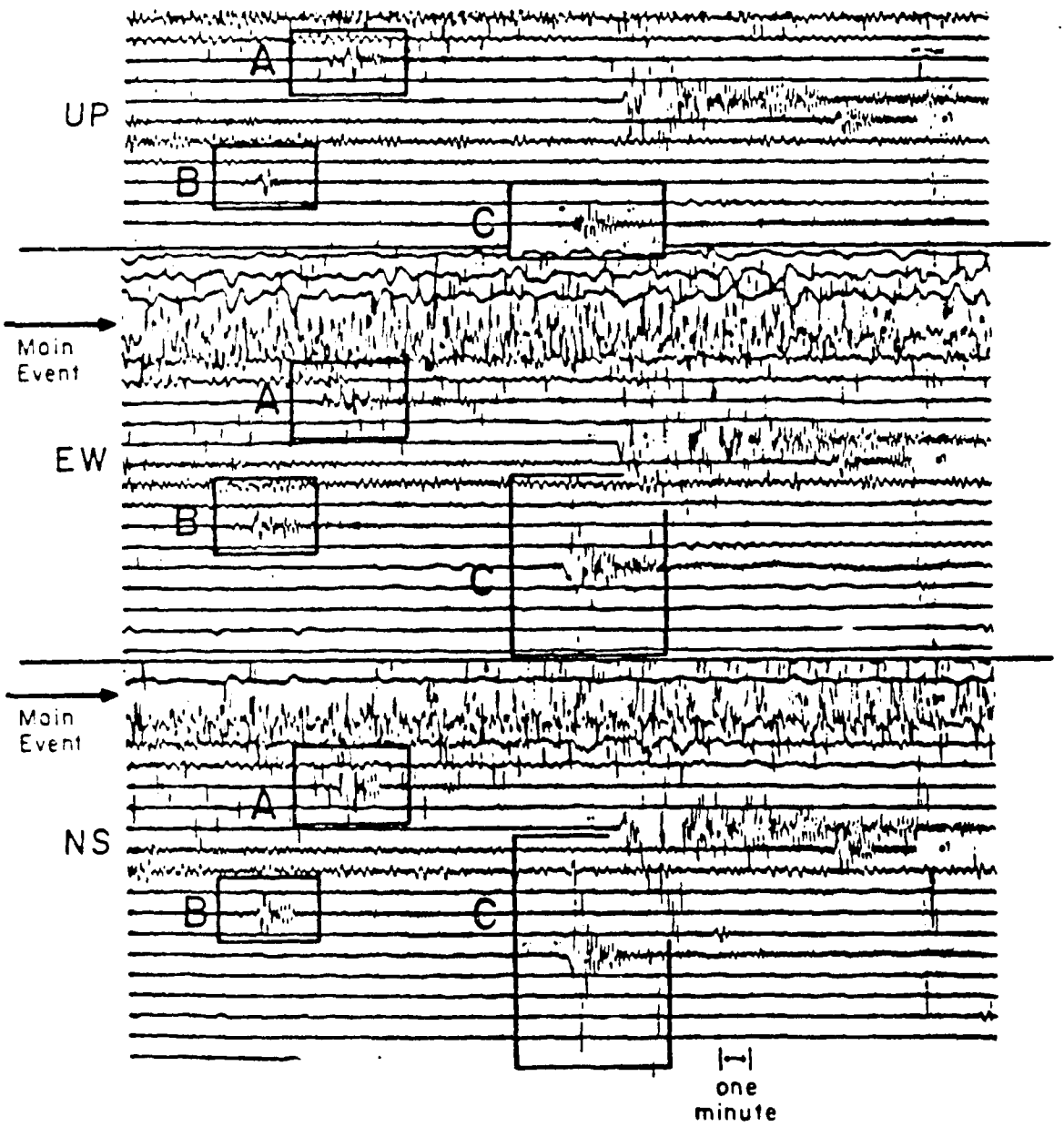

Figure 4. Three-components seismograms of the aftershock sequence recorded on the long-period Press-Ewing 30-90 instrument at Pasadena. Note the difference in waveforms and relative amplitudes of the three boxed aftershocks A, B, and C between components. The event locations are given in Table 1.

displayed in Figure 2 along with examples of aftershock tangential recordings on the long-period (T_o = 6 sec.) torsions.

In the lower comparison we display a magnitude 6.5 Northern Baja (Feb. 15, 1956) earthquake as recorded on the 100X WA and one of its aftershocks (magnitude =5.0) on the high gain long-period torsion. In this example we chose an aftershock that looks similar to the main event. Note that the main event is probably 100 times stronger at the longer periods but because of differences in instrumental response they appear similar. Apparently, a complete trade-off between shifts in corner-frequency of the source spectrum and instrument response has occurred. The upper two records are not so similar but these two events are located at different distances from Pasadena. The bottom event is actually an aftershock from an earlier event, the 1954 Borrego Mountain earthquake and the top event is the 1969 Coyote Mountain earthquake recorded on the 100X WA filtered through a 0.5 sec. up and down triangle. Figure 3 shows the location of all events used in this study. If we knew the mechanisms of these aftershocks we probably could make some good estimates of the faulting parameters of the main events by using the well-known empirical Green's function approach (Hartzell, 1978). This approach has proven very useful in strong-motion simulations of main events from their aftershocks by assuming that the aftershock and the main event have the same mechanisms. The strength of this procedure lies in eliminating the path effects by assuming they are included in the aftershock record automatically. The biggest short-coming of this method is having an aftershock with the same orientation as the main event at the appropriate depth and range.

Generally we do not know the mechanisms of many of these moderate aftershocks because they are too large for local arrays and too small for global networks. In addition, waveforms of different aftershocks are often so different, even if they are spatially close to each other, that it is not easy to determine which aftershock can be used as an empirical Green's function to simulate the main event. Examples of this catagory of events are the series of aftershocks of the 1979 Imperial Valley earthquakes recorded on LP 30-90 at Pasadena (Figure 4). We would like to call attention to the three aftershocks labelled A, B and C where motions for all three events are about the same size on the vertical (UP) component but distinctly different on the horizontals (EW and NS). Differences in waveforms are also apparent on all three components. Since the paths from the Imperial Valley to Pasadena are essentially the same for the three events we would conclude that the source characteristics (depths and faulting parameters such as strike, dip and rake) must be different. As we will discuss shortly, event A is probably a mid-depth normal dip-slip event, whereas event B is a shallow normal dip-slip event. Event C is a deep strike-slip event.

In order to study these seismograms in detail, we digitized and rotated the NS and EW components to obtain the tangential (**SH** waves) and vertical-radial (**P-SV** waves) as displayed in Figure 5. At these periods the motion appears to be well-behaved in that the **P** -waves are not apparent on the tangential component. Particle motion studies of the type discussed by Vidale (1986) conducted on these recordings indicate that the first 10 sec. of record is consistent with **P** -waves and diffracted **SV** -waves followed by Rayleigh motion. Similar analysis of filtered rotated torsion records indicates that separation of the **P-SV** and **SH** system occurs down to periods of about 1 second. Thus, it appears that two-dimensional models may prove effective in

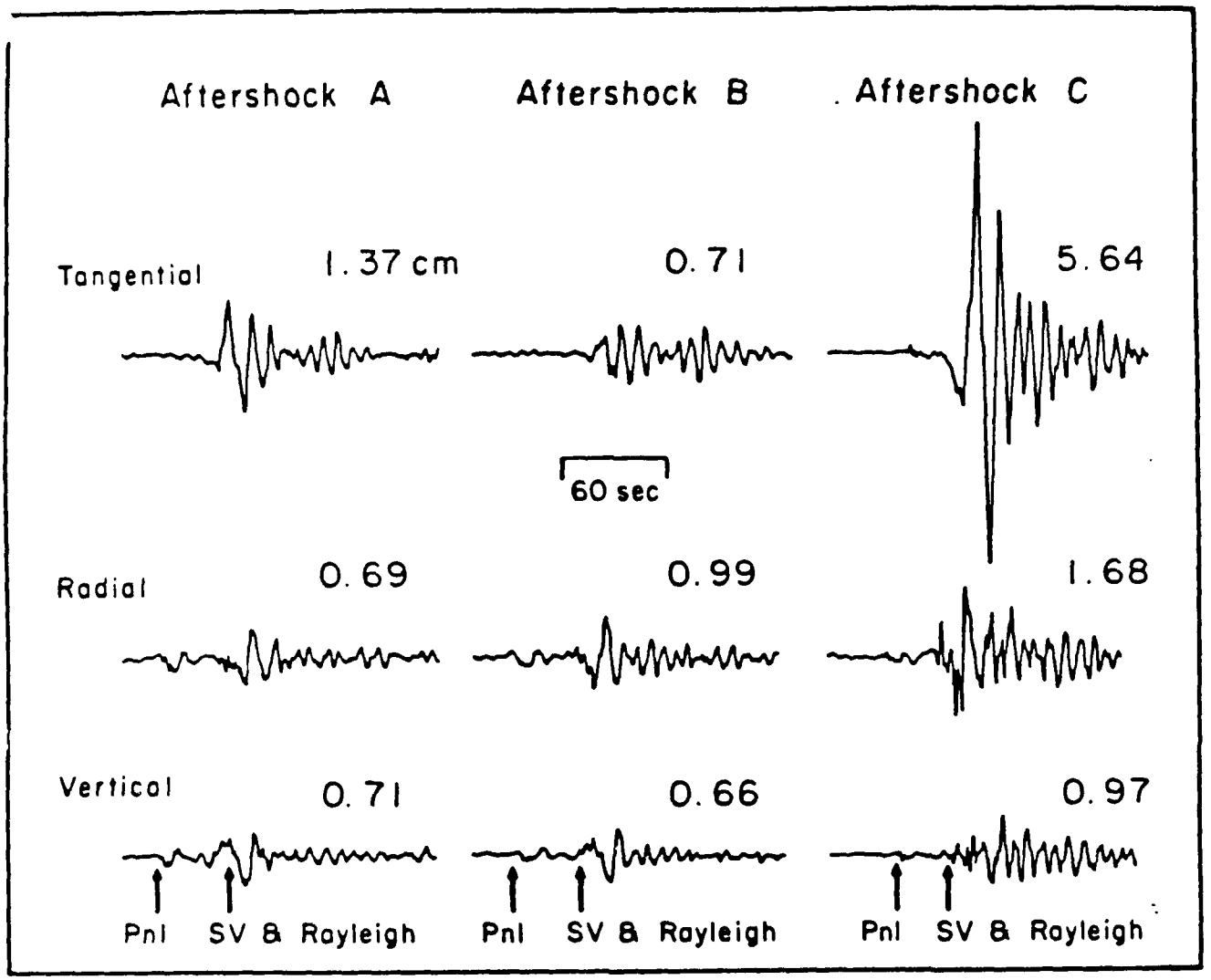

Figure 5. Rotated seismograms of the three aftershocks shown in Figure 4. Maximum amplitudes are given in mm.

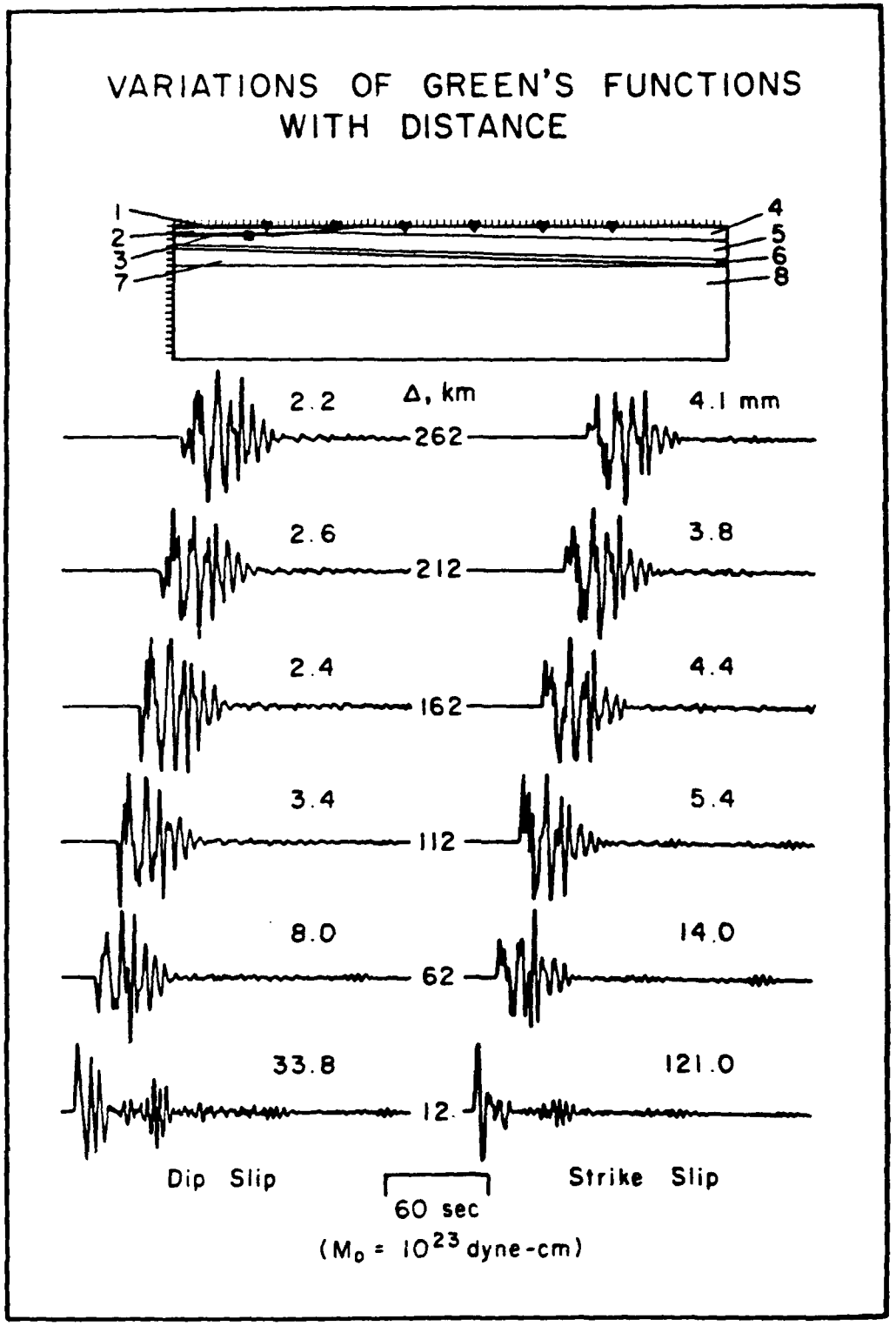

Figure 6. Preferred velocity model and the corresponding Green's functions generated with a source depth of 7 km at the location of the 1976 Brawley earthquake (Δ = 262 km). The stations are located at 50 km interval with the last station as the Pasadena station. Notice the rapid development of surface waves as soon as seismic waves leave the basin. Maximum amplitudes are given in mm $\times 10^{-2}$.

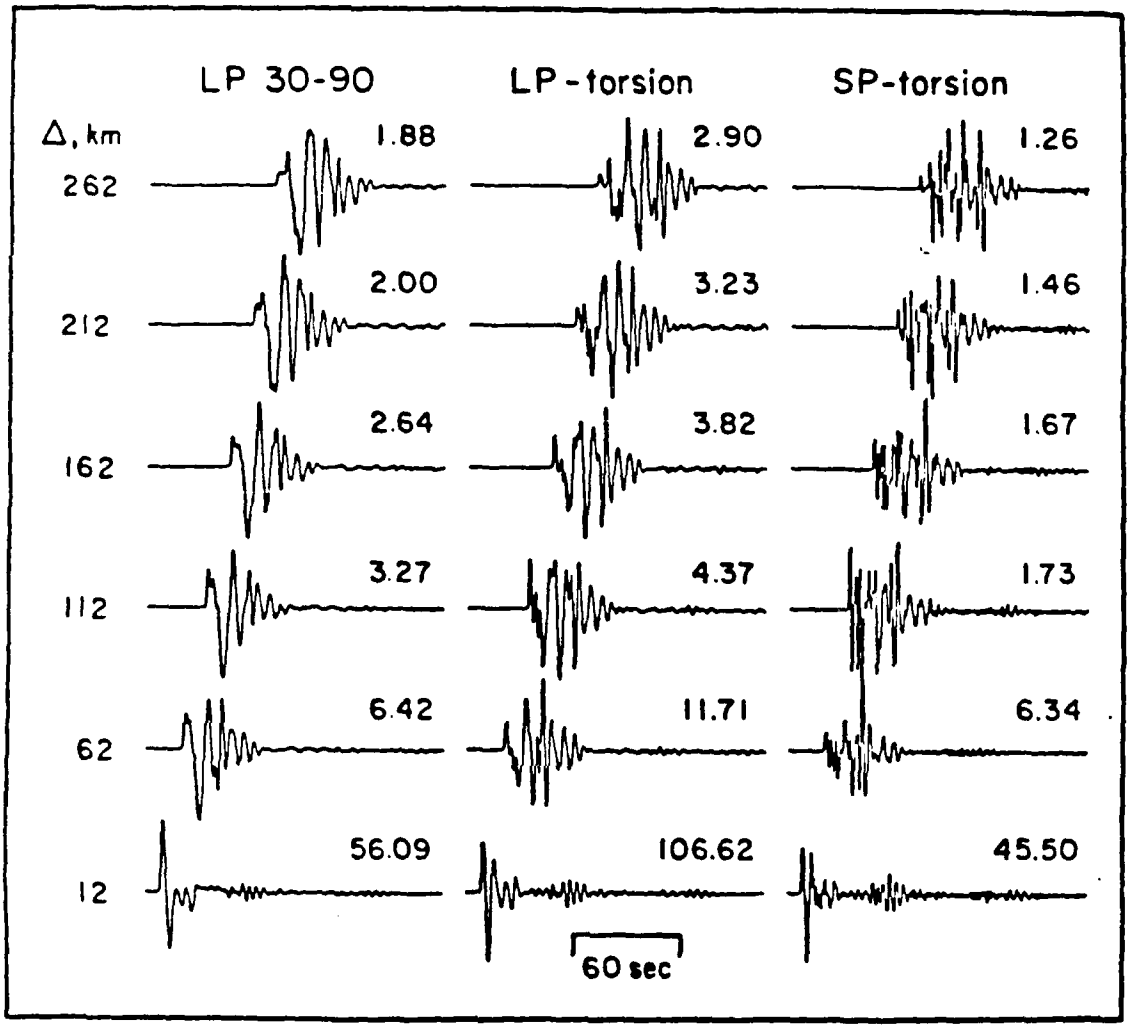

Figure 7. Comparison of the profile of Green's functions corresponding to a pure strike-slip source as recorded on the three instruments displayed earlier in Figure 1. Amplitudes are given in mm for a moment of $4\pi\rho \times 10^{25}$ *dyne-cm.*

removing the propagational distortions so that source retrieval is possible. For example, Helmberger and Vidale (1987) have modeled successful propagational features of 2-D structures at short distances.

In this study, we will derive a 2-D model appropriate for a cross-section from Imperial Valley to Pasadena using master events, known sources, and the forward modeling approach. The resulting Green's functions are then used to examine some of the more important events located in the section (Figure 3). We only considered the tangential motions in this pilot study because less computational effort is involved compared to solving a complete **P-SV** system recorded on the radial and vertical components.

Crustal Cross-section and Green's functions

Searching for suitable Green's functions by trial-and-error testing can be a time-consuming endeavor but the basic approach has proven effective in previous studies (Vidale *et al.* ,1985; Helmberger and Vidale, 1987). Two types of codes were employed, namely the generalized ray method (GRT) for laterally varying layers (Helmberger *et al.*, 1985) and a modified finite-difference (FD) technique (Vidale *et al.*, 1985). The first method is analytical and can be used effectively to adjust deeper smoothly varying structures for proper timing and critical angle positions. The truncation of basins, however, requires the more powerful numerical approach. Some of the details of forward modeling strategies for this situation will be discussed later but, first, we present in Figure 6 our best fitting model and corresponding Green's functions. The source is situated at mid-depth (7 km) in the Imperial Valley basin with responses given at 50 km intervals. Note the soft basin structure. This structure is responsible for the rapid development of surface waves which occurs within the first 50 km of propagation. The waveform appears to change relatively slowly in traversing the remaining path. Note the ringing waveforms for the dip-slip case versus the simpler larger amplitude pulse for the strike-slip orientation at the nearest range. This effect can be explained easily by the corresponding vertical radiation patterns (Vidale *et al.*, 1985).

Figure 7 shows the corresponding synthetics for the strike-slip case convolved with the instrument responses displayed in Figure 1. Amplitudes are given in mm for a moment of $4\pi\rho \times 10^{25}$ dyne-cm where ρ is the density at the source location.

Changing the source positions relative to the basin has the most dramatic effect as displayed in Figure 8. The relatively hard-rock path to Pasadena produces little waveform distortions. Shooting back into the basin produces a wave-train similar to the motions observed at El Centro for Borrego Mountain events (Helmberger and Vidale, 1987). The quick change in waveforms observed at Pasadena for small changes in source positions near the basin boundary is the primary reason for abandoning a flat-layered structure.

Long-Period Modeling

As in all forward modeling attempts, one starts with the best geophysical data available for constraining the initial model. Fortunately, considerable studies have been conducted in

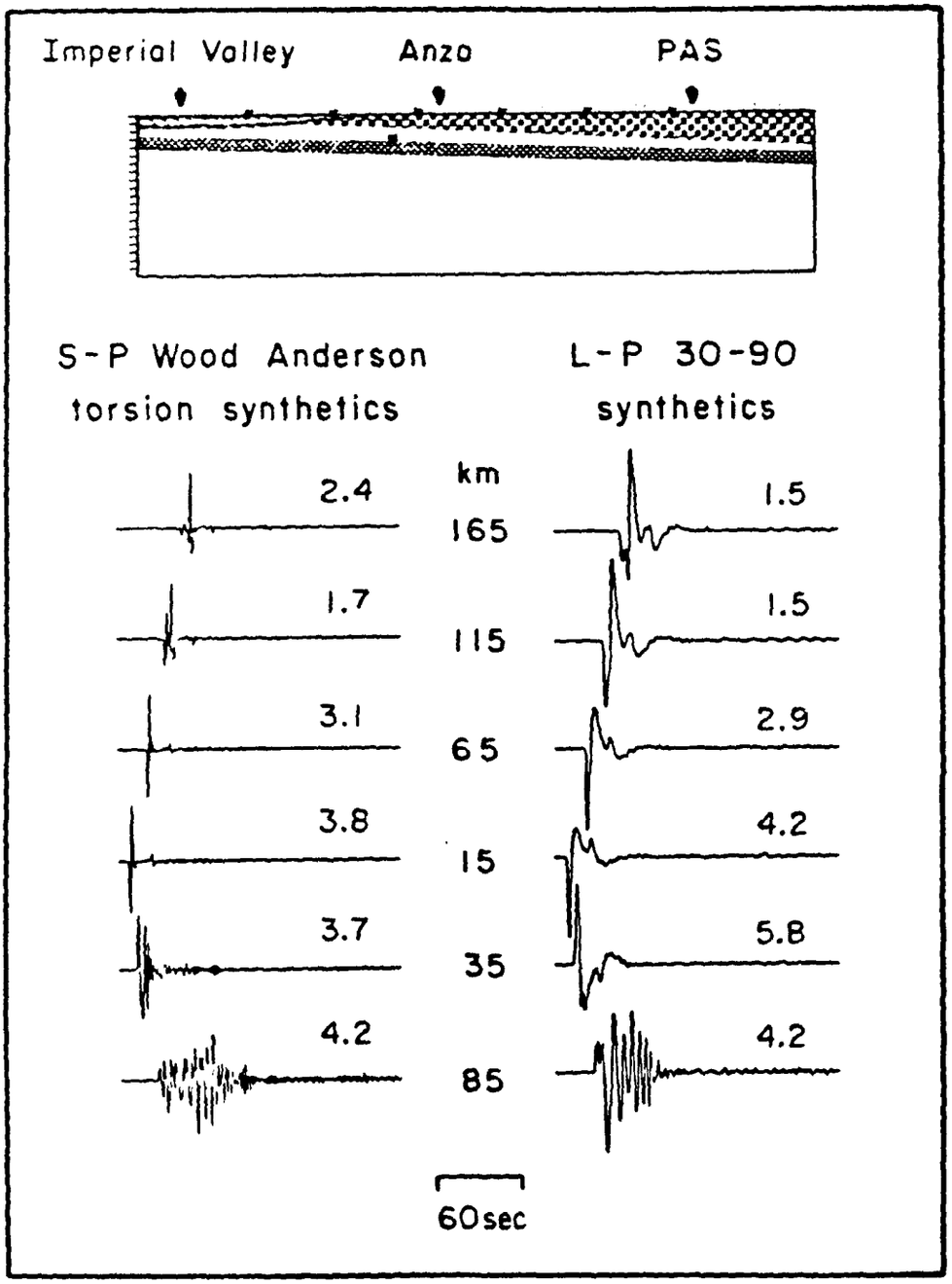

Figure 8. *Profile of Green's functions with the source now outside the basin. Little waveform distortion is observed along the path towards Pasadena (upper four traces) while very complicated waveforms develop rapidly in the basin (lower two traces), indicating the important effect of the basin edge on wave propagation along this profile.*

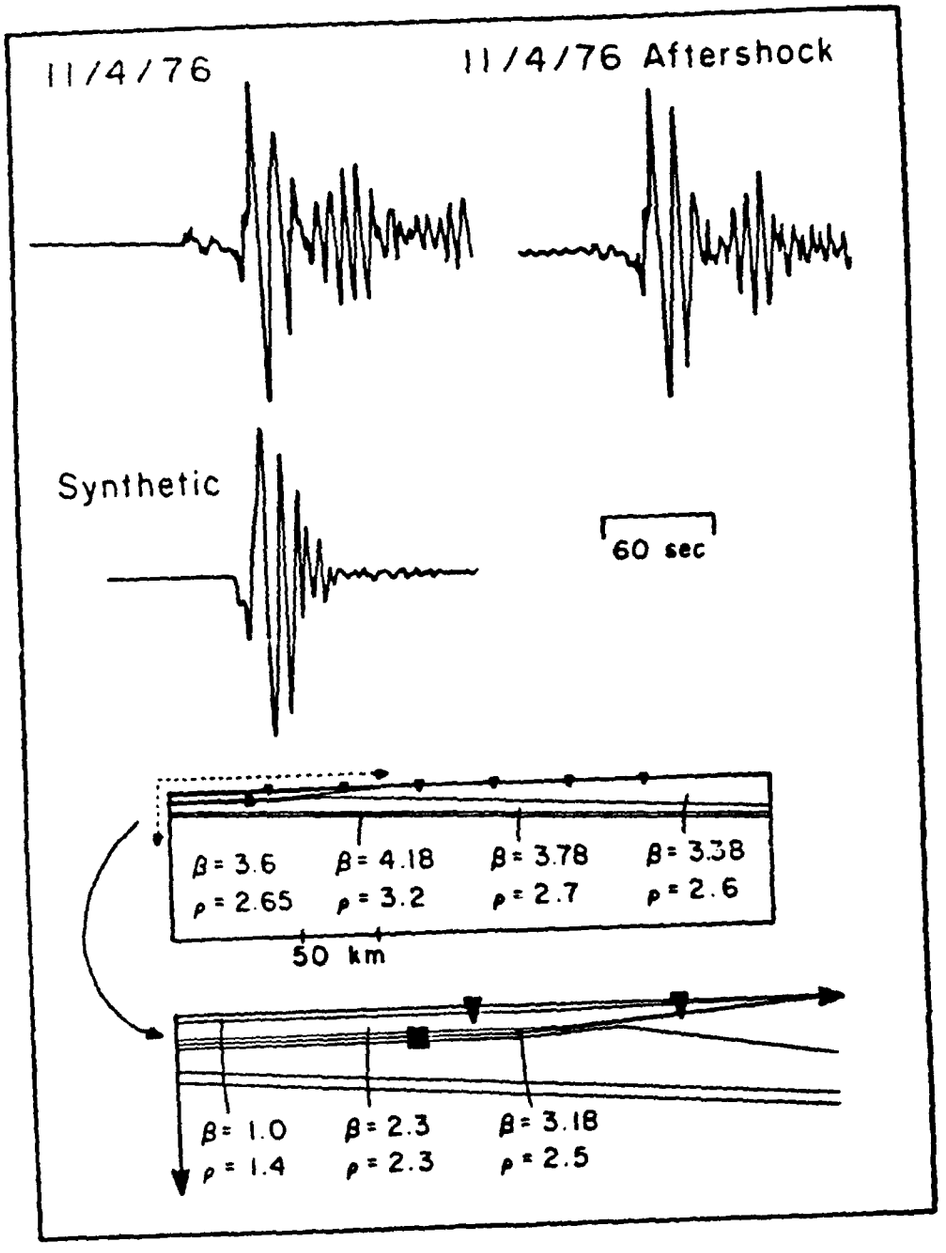

Figure 9. Tangential component of the Brawley earthquake and its aftershock as recorded on LP 30-90 *of the Pasadena station and the corresponding synthetic prediction. The mechanism used to generate the synthetic is obtained from Heaton and Helmberger (1978).*

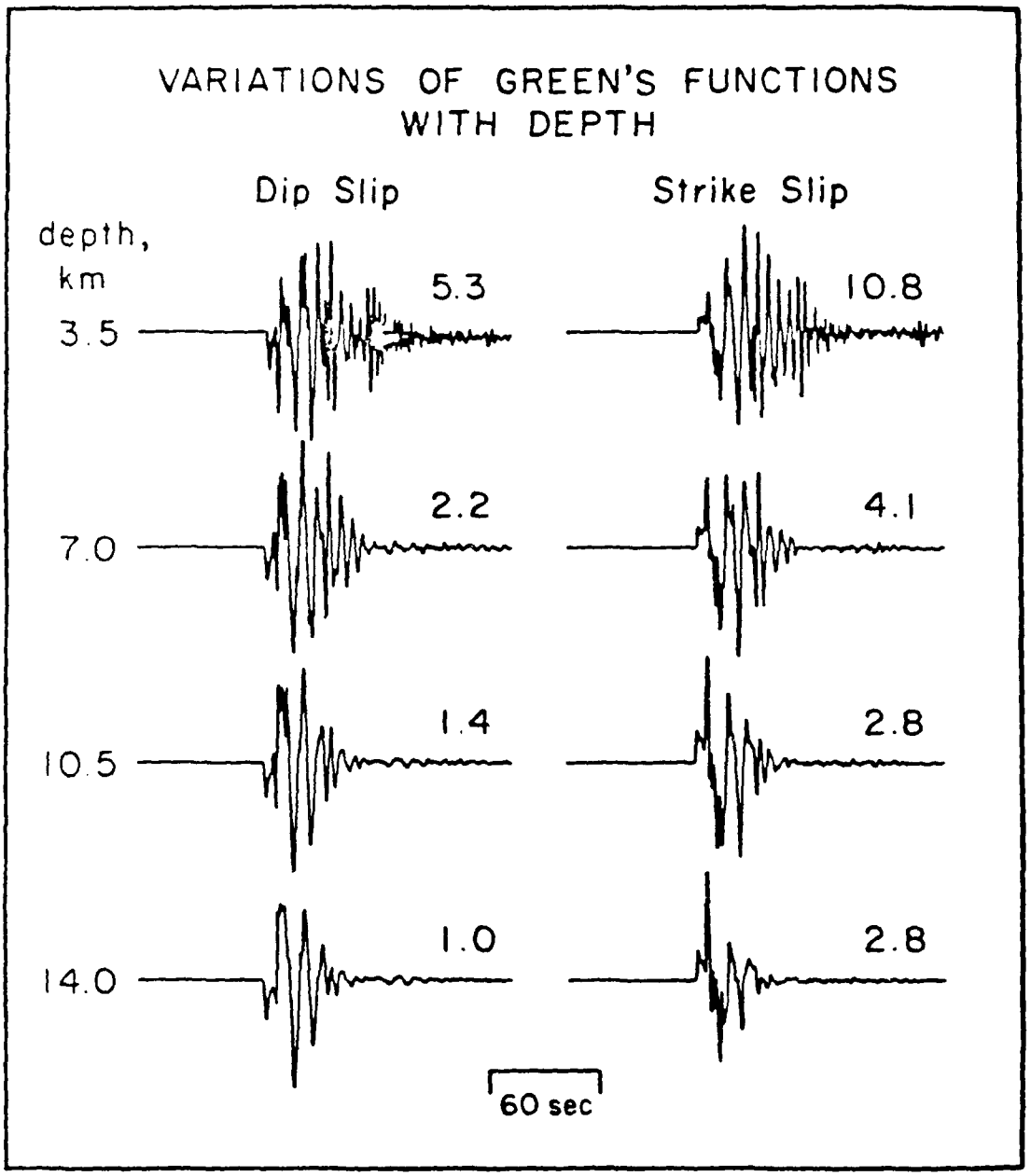

Figure 10. Sensitivity of Green's functions to depth. Sources are put in four different depths at the same epicentral location as the 1976 Brawley event: 3.5, 7.0, 10.5 and 14.0 km. In general, when the source is still in the basin, more surface waves are generated and with the source below the soft and slow sediments in the basin, the waveforms are simpler and energy drops off rapidly with time.

this region. For the Imperial Valley velocity profile, we used the model proposed by Fuis *et al.*(1982) and McMechan and Mooney (1980). Just outside the basin we used the results from Hamilton (1970) who investigated the Borrego Mountain aftershocks with controlled calibration shots. Hamilton's results suggest a thick crust-mantle transition zone. At Pasadena we adopted the model proposed by Hadley and Kanamori (1977, 1979) with a thick crust and relatively sharp Moho transition. These vertical profiles were assembled by allowing for a gentle dipping connecting structure and produce an initial cross-section from Imperial Valley to Pasadena.

Synthetics for this starting model were generated and compared with observed records for the various calibration events displayed in Figure 3. For example, in Figure 9 we give the comparison between predictions for the Brawley event and its aftershock. The source parameters for this event were determined earlier by Heaton and Helmberger (1978), and treated as known. This assumption allows us to perturb the various model parameters to bring about agreements in waveform and absolute timing. This procedure goes relatively fast for long-period modeling but becomes increasingly tedious at higher frequencies.

The best fitting model to date has a slow mantle velocity of 4.28 km/sec, a northwest-thinning Moho-crustal transition layer of 4.18 km/sec, a dipping crustal-Moho transition layer of 4.05 km/sec, a dipping lower crust of 3.78 km/sec that thins out to the northwest, and an upper crust of 3.38 km/sec that also dips northwest. The idealized Imperial Valley basin surface has two layers of very slow shear velocities of 1.0 km/sec and 2.34 km/sec, corresponding to what Fuis *et al.*(1982) described in their **P** -wave refraction profiles. A thin layer of 3 km/sec that thins out at the edge of the basin lies underneath the slow sediments. This model is able to predict the arrival time and the waveform of the first 40 seconds. The secondary arrival occuring about 60 sec. after the initial motion is present on many records and will be discussed later.

The moment required to match the amplitudes is 2.1×10^{23} dyne-cm which can be compared to 3.2×10^{23} dyne-cm found by Heaton and Helmberger (1978) using local strong-motion intermediate-period records. This seems like a reasonable difference since lack of correction for **Q** and scattered energy, instrumental gain, small changes in strike etc. could account for such a difference.

Finally, with the model adjusted to predict synthetics matching the master event, we can easily perform depth sensitivity studies as displayed in Figure 10. The synthetics are generated with the source at a distance of 262 km from Pasadena, so the source is inside the basin for depths of 3.5 and 7 km and below the basin for depths of 10.5 and 14 km. In both strike-slip and dip-slip mechanisms, absolute amplitudes decrease with depth. In addition, pure strike-slip mechanism results in higher amplitudes compared to a pure dip-slip mechanism, almost twice the amplitudes at all four depths. In general, we also expect to see a shallow source exciting more surface waves in both pure strike-slip and pure dip-slip, and a deeper source tends to show less complexity. These results are similar to those found in flat layered models. After reviewing mechanisms for events in this region from Fuis *et al.*1982; Heaton and Helmberger, 1978; Johnson and Hadley, 1976; Johnson and Hutton, 1982; Liu and Helmberger, 1985, a total of 21 possible orientations for each event was considered. The best fitting combinations are

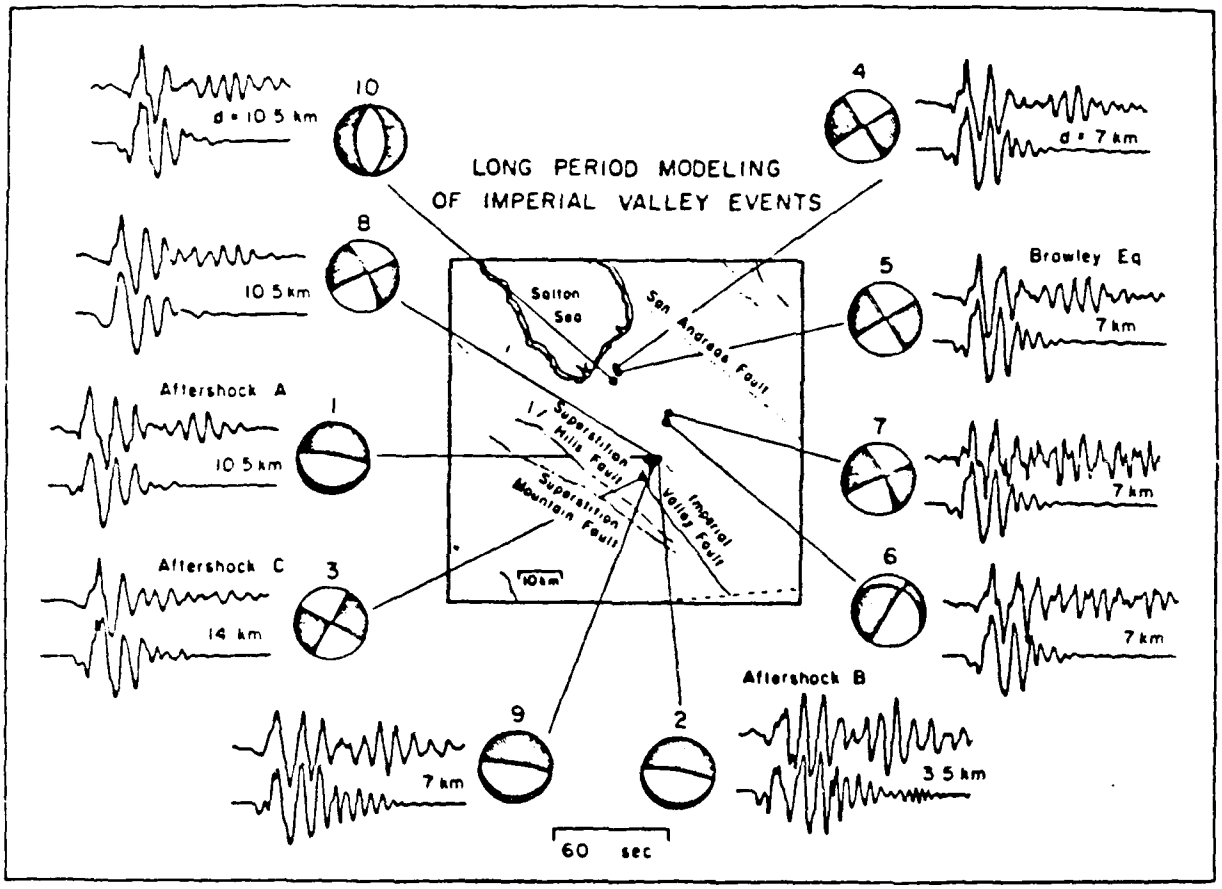

Figure 11. Long-period modeling of nine unknown aftershocks and small events in the Imperial Valley. Data shown are recorded on the **LP ≈ 30-90** *instrument. The modeled mechanisms are also shown. Results indicate that event "C" is a deep strike-slip event, event "B" a shallow dip-slip event and event "A" a mid-depth dip-slip event.*

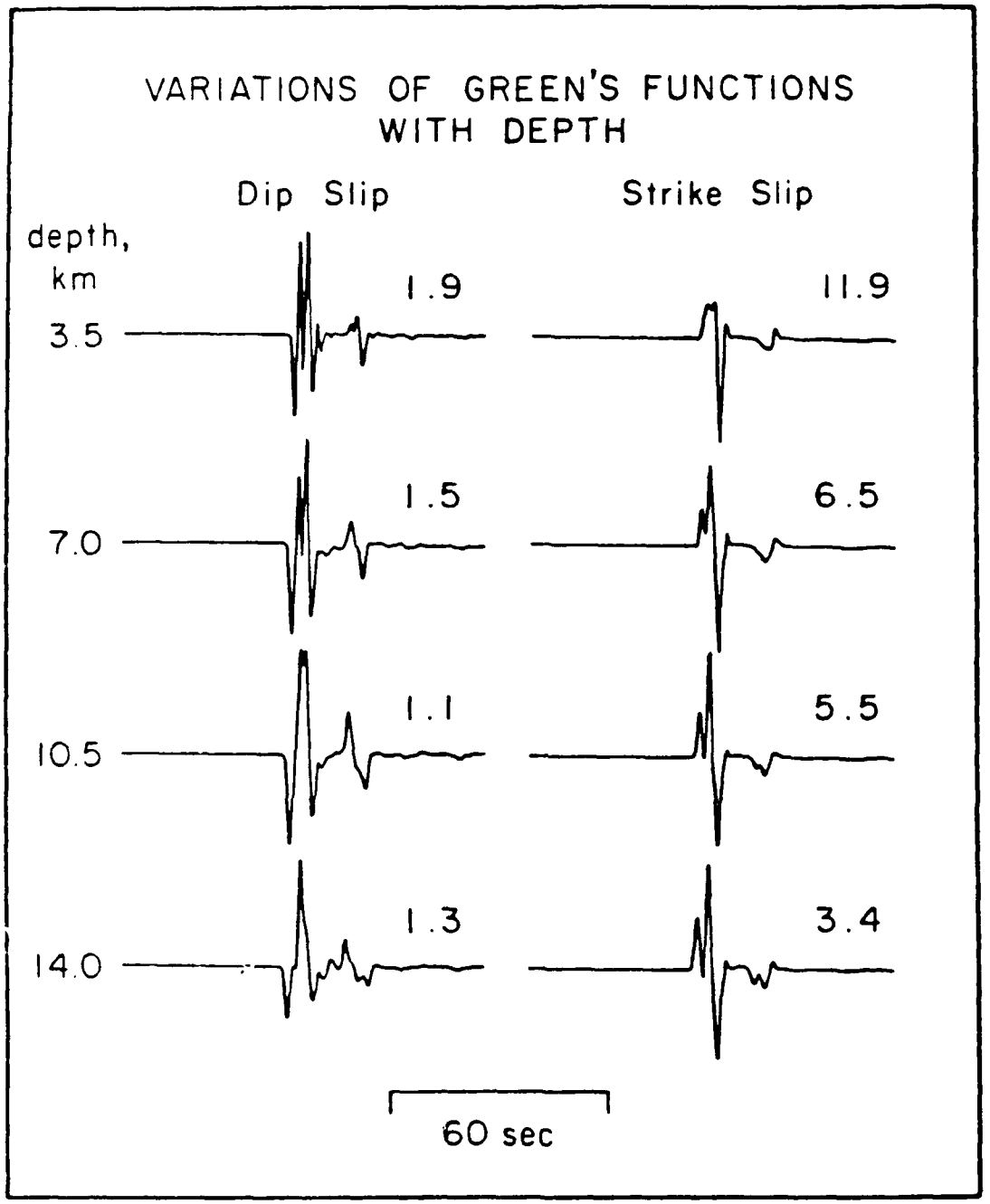

Figure 12. Sensitivity of Green's functions to depth with the source at Anza distance. The waveforms are simple compared to those displayed in Figure 10. There is not as much a difference in the complications of waveforms with depth as in the previous case.

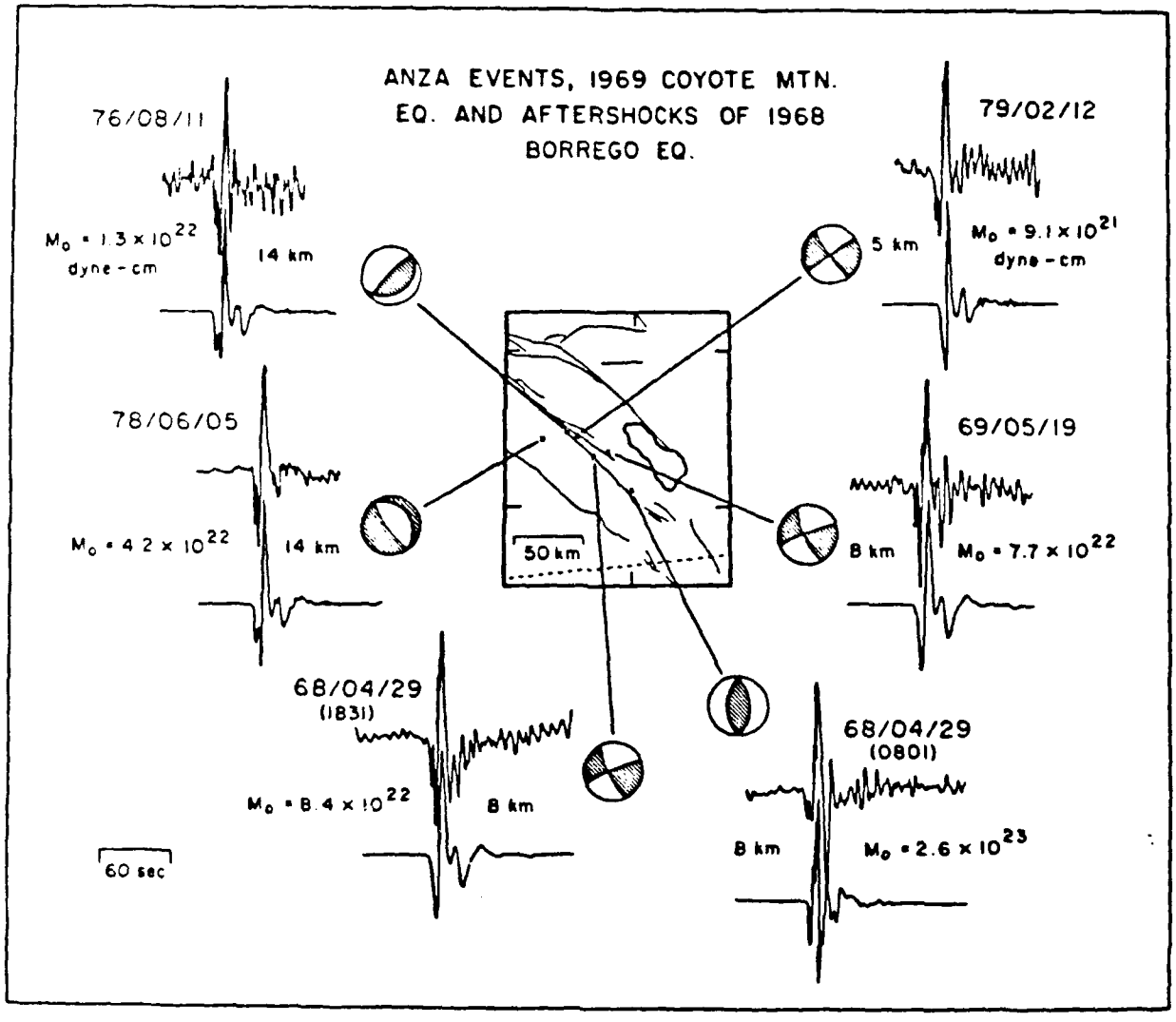

Figure 13. Long-period modeling of three Anza events and two aftershocks of the 1968 Borrego Mountain event and one of the 1969 Coyote Mountain aftershock. The corresponding focal mechanism is also shown.

displayed in Figure 11 with depths, magnitudes and moment estimates given, see Table 1 and 2. Note that event C as discussed earlier is modeled as a deep strike-slip while event B appears to be a shallow dip-slip.

For small events we expect source durations to be short compared to the 30-90 instrumental response, see Figure 1, and, therefore, we should be able to fit any observed long-period seismograms by a linear combination of the Green's functions displayed in Figure 10. A total of nine events with unknown source parameters, including the three aftershocks described earlier and the Brawley aftershock, were collected as a data set to which the Green's functions were applied. These events are listed in Table 1 where the locations and depths are given according to the Caltech catalog.

The sensitivity of Green's functions to depth for sources at Anza appears totally different from that in Imperial Valley. In general, the waveform is very simple for both strike-slip and dip-slip mechanisms, and it changes only slightly with depth (Figure 12). It appears that the deeper the event, the simpler the waveform it created. This feature proves useful in fixing the depths of events as did the amount of surface wave excitation for events in the Imperial Valley.

In order to test the derived crustal model for its accuracy outside the Imperial Valley sedimentary basin, we applied the same process to three events at Anza, an aftershock of the Coyote Mountain 1969 event and two aftershocks of the 1968 Borrego Mountain event, see Figure 13. The mechanisms used to model the Anza events were again collected from various studies (Sanders and Kanamori, 1984; Given, 1983) and adjustments made to fit the data. The fits between synthetics and data are reasonably good with results given in Table 3.

Most of the aftershocks in the Borrego region preferred mechanisms similar to their main events with results given in Table 4. The mechanisms for the main events are given by (Thatcher and Hamilton, 1973; Ebel and Helmberger, 1982; Burdick and Mellman, 1976 and Sanders *et al.*, 1986). The waveforms are relatively simple, as shown in Figure 13, compared to the Imperial Valley events in Figure 11, suggesting the complications of waveforms due to the existence of the basin.

Strong Motions from Imperial Valley Events

One of the primary objectives of this study was to provide Green's functions appropriate for strong motions in the frequency domain of 10 to 0.1 Hz. Unfortunately, we do not have broad-band data at these intensity levels so that we must rely on recordings from the 100X WA.

At 10 Hz the problem becomes extremely complex and the motions no longer separate into the **P-SV** and **SH** systems. Secondly, we no longer expect events of this magnitude to be as simple as events discussed earlier. Thus, it is difficult to assess the adequacy of our results since we can only compare predicted motions at Pasadena based on independently determined source studies from near-in data at Imperial Valley. Three component data may help resolve the source properties by providing more data, and this subject will be addressed in a later effort. At

this stage, we will limit ourselves to the 1979 Imperial Valley earthquake to serve as an example. The secondary energy arriving about 40 secs after the initial motion which accompanies many of the shallow events in the Valley will be discussed later.

1979 Imperial Valley Earthquake

Several inversions were done on the 1979 Imperial Valley mainshock. The general consensus of the rupture includes an initial 10 km deep epicenter that rupture northwestward along the Imperial Fault at a rate of 75% of the shear velocity, then rupture continued on at a shallower depth (Hartzell and Helmberger, 1982; Hartzell and Heaton, 1983; Olson and Aspel, 1982). Archuleta (1984) holds a slightly different conclusion on the rupture process, with an initial strike-slip source at about 8 km depth rupturing northwestward. Subsequent rupture occurred at two main locations, both at about 10 km depth, with a minor dip-slip rupture at about 30 km from the epicenter along the strike of the fault. The Hartzell and Helmberger's model (model HH1) and the Hartzell and Heaton's model (model HH2) are very similar, while Olson and Aspel's model (model OA) is a more continuous model, which can be simulated using nine segments of rupture. We attempt to model this 1979 mainshock by treating each rupture segment in each inversion model as an earthquake source. Using the same mechanism as inverted by the above workers in each segment, we combine our synthetics with the mechanisms and then add the segments up according to the corresponding delay time along the fault. Simulations of such strong motions appropriate for the Pasadena torsion are shown in Figure 14 with the corresponding inversion models.

A comparison of the filtered data with the synthetic predictions is displayed in Figure 15. The synthetic responses shown in Figure 14 require a time-derivative to compare with the corresponding WA record in displacement which tends to emphasize the high frequency tails such as in the Olsen-Apsel model. In general, all of these models display some merit although it appears that the two models on the left fit the waveform data somewhat better. The important point in this comparison is not which model fits better but that complex earthquakes (multiple-ruptures) can be distinguished from simple events. Thus, this type of regional data from historic events can be used to help delineate rupture patterns along important fault segments.

Discussion and Conclusion

Many of the events in the Imperial Valley data set have a secondary arrival that is about 60 sec late (Figure 11), which we have neglected. There are several possibilities for the secondary arrivals: (1). Source structural effects which includes three-dimensional scattering due to the Imperial Valley basin structure, (2). Source parameters effects which suggests double events or complicated faulting mechanisms, (3). Receiver structural effects which are local effects due to receiver being in or near a basin, (4). Path complications which suggest structural effects along the same path that are not in the present model.

Source structural effects would result in waves arriving at the receiver along different azimuths. We determined by complex polarization studies (Vidale, 1986) on the three components,

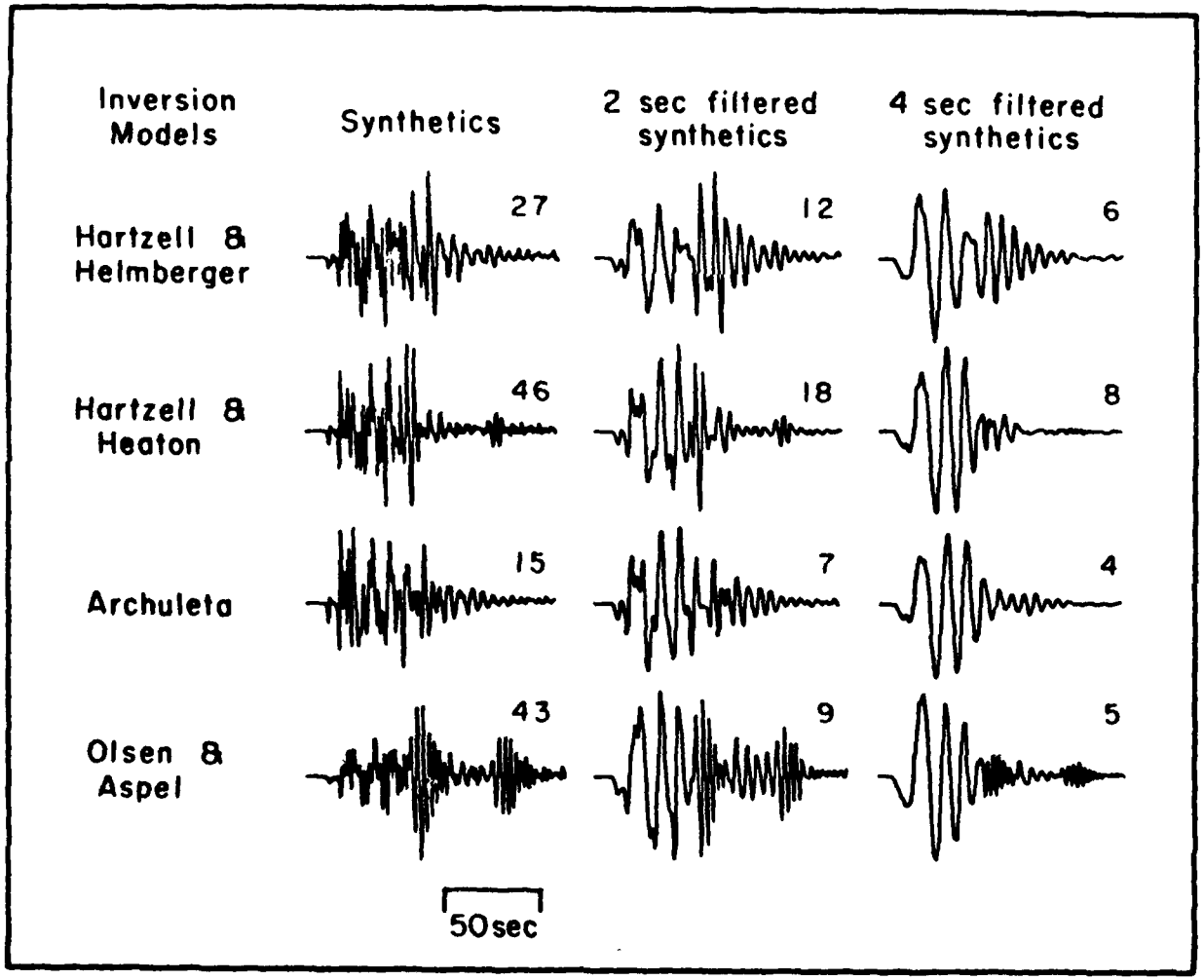

Figure 14. Simulations of strong motion of the 1979 Imperial Valley event using four inversion models (Hartzell and Helmberger, 1982; Hartzell and Heaton, 1983; Archuleta, 1982; and Olson and Aspel, 1982). Amplitudes are given in cm for a moment of 5.0 x 10^{25} dyne-cm.

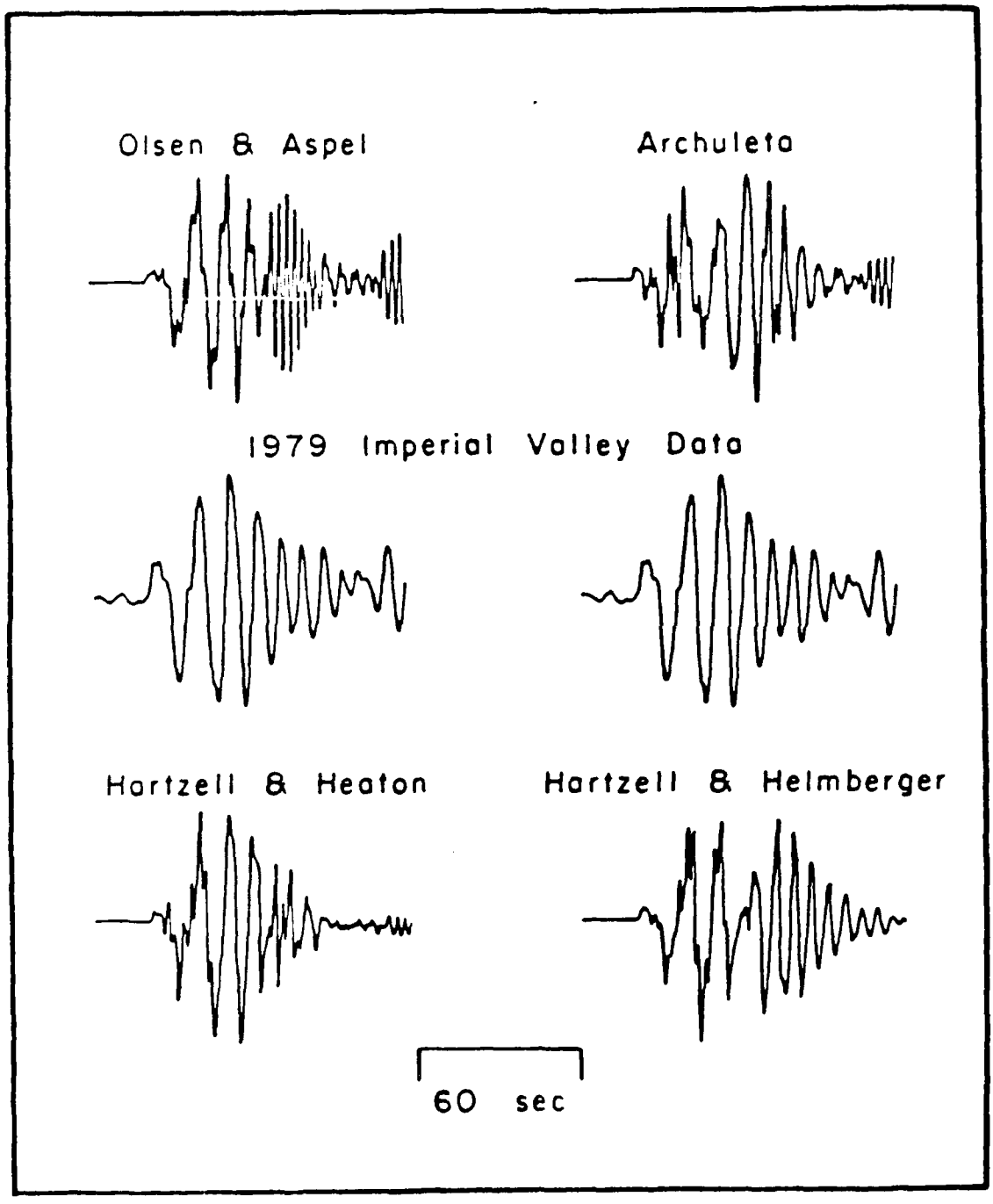

Figure 15. Comparison of 4-sec filtered tangential motion against predicted synthetics.

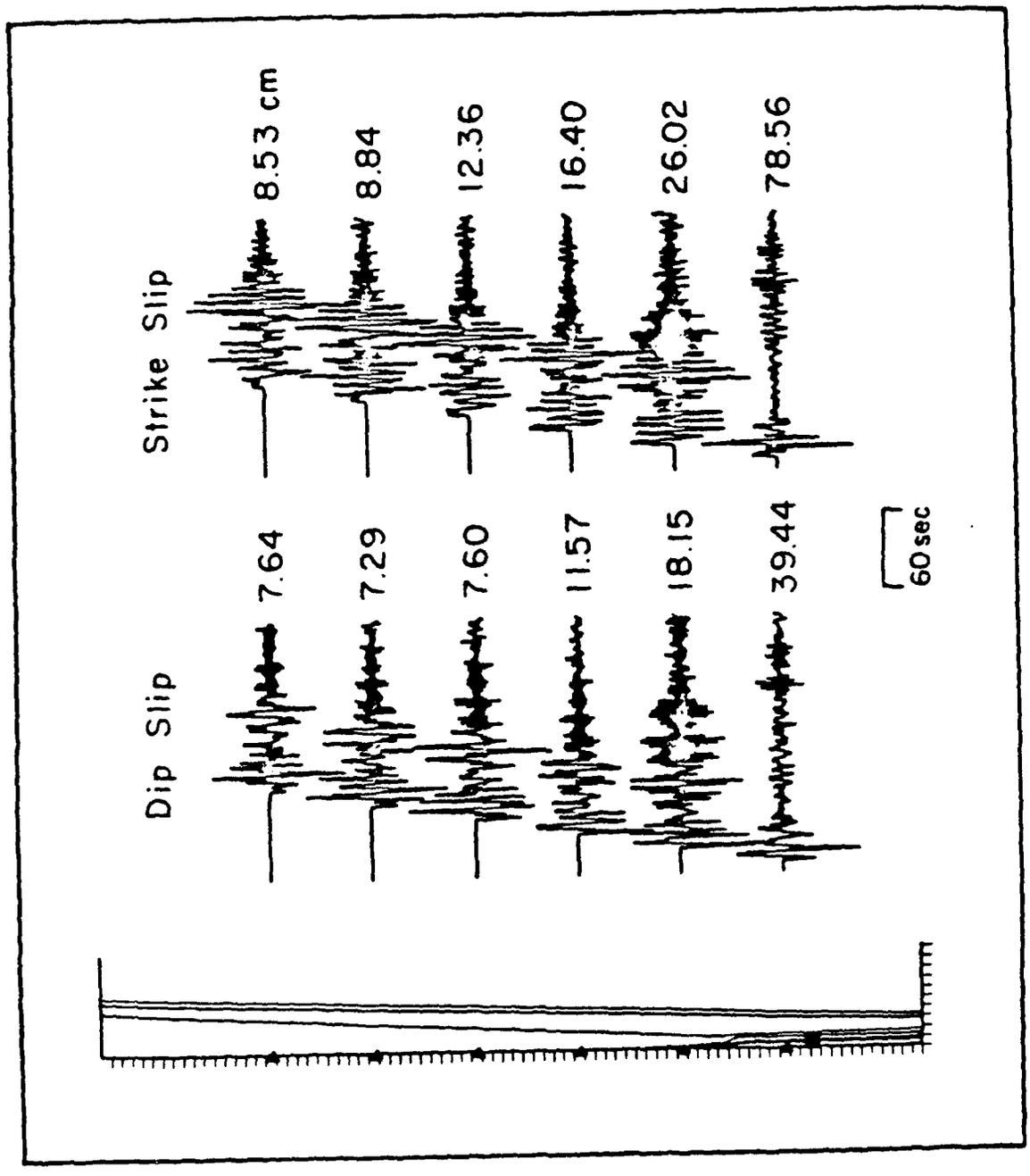

Figure 16. Numerical responses along a profile from IV to PAS for an idealized basin model. Note the sharp edge of the basin typical of faulted structures at the western edge of this particular basin.

that the late arrival was traveling along approximately the same azimuth as the main arrival. So we believe that this late arrival comes mainly from the same ray azimuth as the main arrival though there is a clockwise rotation after the first arrival at Pasadena. This effectively rules out possibility #1.

The three events we studied at Anza, the Borrego Mountain distance and the Coyote Mountain events show no secondary arrival at all. The arrivals have relatively simple waveforms. The hypothesis that the secondary arrivals on the Imperial Valley events are effects of the local receiver structure is then ruled out because of the absence of such arrival on the other records of events outside the basin.

We are now left with possibilities #2 and #4. It is fairly unreasonable to attribute double mechanisms to all events with secondary arrivals. However, shallow events have secondary arrivals while deeper events do not. The secondary arrival also has lower frequency than the main arrival as recorded on the long-period instrument and are not found in high frequency records. These features suggest that this secondary pulse has traveled as a trapped surface wave in the surface sediments to the edge of the basin and regenerates into a normal Love wave.

A number of numerical profiles with sources placed at various depths in a variety of basin models were generated to test the above hypothesis. When the source is situated in the sediments and when the basin ends sharply the secondary arrival becomes particularly strong as displayed in Figure 16. Basin models with gentle dipping edges do not show the secondary arrival and apparently scatter the surface waves at lower ray parameters, probably teleseismically as found in the study by Stead and Helmberger (1988).

The broad-band responses displayed in Figure 16 do not contain the instrument and suggest that the secondary arrival is not depleted in high frequency as observed. Thus, the observed secondary arrival has lost its high frequency by attenuation in the soft sediments or, perhaps, the source excitation has very low stress drop. This subject is best pursued with broad-band three component array data and will be addressed in a subsequent paper.

In conclusion, we have demonstrated the effectiveness of using events with known source mechanisms to derive a regional crustal model and make use of the model to retrieve source mechanisms for other events. This method is proven to be successful in predicting **SH** waveforms and arrival times of events at a different distance from the receiver. The method only requires prior knowledge about well studied events and the availability of three-components seismograms with well-recorded events of unknown sources. These requirements can be met easily since we have abundant stations with three-components seismograms that have recorded many regional events. As long as we have one master event to work with in the same area, source retrievals and strong motion simulations or predictions can be done.

We have also demonstrated the sensitivity of various Green's functions to depth and mechanisms. By applying the depth sensitivity of **SH** waveforms, we can now have an estimate of

the depth of an event in the Imperial Valley recorded at regional distance by the rate of drop-off of reverberations in the record. This provides a fairly powerful tool in detail modeling of an event since we can have an initial estimate of the depth range of the event. With such a detailed model, we now can simulate long period strong-motions of an earthquake with any source mechanism,location and magnitude along the profile from Imperial Valley to Pasadena.

REFERENCES

Archuleta, R. J., 1984. A faulting model for the 1979 Imperial Valley earthquake, J. Geophys. Res., **89**, 4559-4585.

Burdick, L. J. and G. K. Mellman, 1976. Inversion of the body waves of the Borrego Mountain earthquake to the source mechanism, Bull. Seism. Soc. Am., **66**, 1485-1499.

Ebel, J. E. and D. V. Helmberger, 1982. P-wave complexity and fault asperities: The Borrego Mountain, California, earthquake of 1968, Bull. Seism. Soc. Am., **72**, 413-437.

Fuis, G. S., W. D. Mooney, J. H. Healy, G.A. McMechan and W.J. Lutter, 1982. Crustal structure of the Imperial Valley region in the Imperial Valley, California earthquake of Oct. 15, 1979, U. S. Geol. Survey Prof. Paper, **1254**, 25-49.

Given, D. D., 1983. Seismicity and structure of the trifurcation in the San Jacinto fault zone, southern California, Master's Thesis, California State University, Los Angeles.

Hadley, D. and H. Kanamori, 1977. Seismic structure of the Transverse Ranges, California, Bull. Geol. Soc. Am., **88**, 1469-1478.

Hadley, D. and H. Kanamori, 1979. Regional S-wave structure for southern California from the analysis of teleseismic Rayleigh waves, Geophys. J. R. astr. Soc., **58**, 655-666.

Hamilton, R. M., 1970. Time-term analysis of explosion data from the vicinity of the Borrego Mountain, California, earthquake of 9 April, 1968, Bull. Seism. Soc. Am., **60**, 367-381.

Hartzell, S. T., 1978. Earthquake aftershocks as Green's functions, Geophys. Res. Letts., **5**, 1-4.

Hartzell, S. T. and D. V. Helmberger, 1982. Strong-motion modeling of the Imperial Valley earthquake of 1979, Bull. Seism. Soc. Am., **72**, 571-596.

Hartzell, S. T. and T. H. Heaton, 1983. Inversion of strong ground motion and teleseismic waveform data for the fault rupture history of the 1979 Imperial Valley, California, earthquake, Bull. Seism. Soc. Am., **73**, 1553-1583.

Heaton, T. H. and D. V. Helmberger, 1978. Predictability of strong ground motion in the Imperial Valley: Modeling the M 4.9, November 4, 1976 Brawley earthquake, Bull. Seism. Soc. Am., **68**, 31-48.

Helmberger, D. V., 1983. Theory and application of synthetic seismograms, earthquake: observations, theory and observations. Proceedings of the International School of Physics, Enrico Fermi Course LXXXV, H. Kanamori and E. Boschi, Editors, North-Holland, Amsterdam, 174-217.

Helmberger, D. V., G. Engen and S. Grand, 1985. Notes on wave propagation in laterally varying structure, J. Geophys., **58**, 82-91.

Helmberger, D. V. and J. E. Vidale, 1987. Modeling strong motions produced by earthquakes

with 2-D numerical codes, submitted to Bull. Seism. Soc. Am..

Johnson, C. E. and D. M. Hadley, 1976. Tectonic implications of the Brawley earthquake swarm, Imperial Valley, California, January 1975, Bull. Seism. Soc. Am., **66**, 1133-1144.

Johnson, C. E. and L. K. Hutton, 1982. Aftershocks and preearthquake seismicity, California earthquake of Oct. 15, 1979, U. S. Geol. Survey Prof. Paper, **1254**, 59-76.

Kanamori, H. and J. Regan, 1982. Long-period surface waves generated by the 1979 Imperial Valley earthquake, U.§. Geol. Surv. Profess. Paper **1254**, 55-58.

Liu H. L. and D. V. Helmberger, 1985. The 23:19 aftershock of the 15 October 1979 Imperial Valley earthquake: More evidence for an asperity, Bull. Seism. Soc. Am., **75**, 689-708.

McMechan, G. A. and W. D. Mooney, 1980. Asymptotic ray theory and synthetic seismograms for laterally varying structure: Theory and application to the Imperial Valley, California, Bull. Seism. Soc. Am., **70**, 2021-2036.

Olson, A. H. and R. J. Aspel, 1982. Finite faults and inverse theory with applications to the 1979 Imperial Valley earthquake, Bull. Seism. Soc. Am., **72**, 1969-2001.

Sanders, C. O. and H. Kanamori, 1984. A seismotectonic analysis of the Anza seismic gap, San Jacinto fault zone, southern California, J. Geophys. Res., **89**, 5873-5890.

Sanders, C. O., H. Magistrale and H. Kanamori, 1986. Rupture patterns and preshocks of large earthquakes in the southern San Jacinto fault zone, Bull. Seism. Soc. Am., **76**, 1187-1206.

Stead, R. J. and D. V. Helmberger, 1988. Numerical-analytical interfacing in two dimensions with applications to modeling NTS seismograms, in Special issue "Scattering and Attenuation of Seismic Waves", Pure and Appl. Geophys., (in press).

Thatcher, W. and R. M. Hamilton, 1973. Aftershocks and source characteristics of the 1969 Coyote Mountain earthquake, San Jacinto fault zone, California, Bull. Seism. Soc. Am., **63**,, 647-661.

Vidale, J., D. V. Helmberger, and R. W. Clayton, 1985. Finite-difference seismograms for **SH** waves, Bull. Seism. Soc. Am., **75**, 1765-1782.

Vidale, J., 1986. Complex polarization analysis of particle motion, Bull. Seism. Soc. Am., **76**, 1393-1405.

Table 1. List of earthquakes used in the Imperial Valley long period study

Event #	Date	Time	Latitude(N)	Longitude(W)	Depth(km)	Dip	Rake	Strike
1(A)	79-10-16	03:39:35.04	32° 56.92'	-115° 33.01'	5.14	10°	90°	99°
2(B)	79-10-16	09:36:41.89	32° 56.98'	-115° 31.41'	4.27	10°	90°	99°
3(C)	79-10-16	11:47:56.06	32° 54.81'	-115° 33.61'	5.09	90°	180°	119°
4	76-11-4	14:12:50.28	33° 07.41'	-115° 37.19'	2.71	90°	180°	328°
5*	76-11-4	10:41:37.54	33° 07.89'	-115° 37.40'	0.55	90°	180°	328°
6	79-10-16	23:16:32.18	33° 01.33'	-115° 30.37'	3.32	20°	180°	300°
7	79-10-17	22:45:33.82	33° 02.40'	-115° 30.02'	1.87	70°	180°	334°
8	79-10-16	03:10:47.83	32° 57.05'	-115° 32.10'	4.22	70°	180°	334°
9	79-10-16	05:49:10.97	32° 56.48'	-115° 32.31'	4.66	10°	90°	99°
10	81-4-25	07:03:14.12	33° 06.24'	-115° 37.69'	5.24	45°	-90°	0°

* Brawley Earthquake

Table 2. Imperial Valley moments obtained by fitting long-period and high-frequency SH and the corresponding M_L and depths compared to the catalogue value. M_0 are given in 10^{22} dyne-cm. Depths are given in km.

Event	M_o		M_L		Depth(km)	
	high frequency	long-period	*SH*	catalog	Modeled	catalog
1	10.5	15.3	4.5	4.6	10.5	5.14
2	0.6	2.4	3.3	4.1	3.5	4.27
3	12.3	39.2	4.6	4.8	12.25	5.09
4	-	6.3	4.5	4.4	7.0	2.71
5	21.3	30.0	4.8	5.1	7.0	0.55
6	-	6[illegible].0	5.2	5.0	7.0	3.32
7	-	4.1	4.4	4.7	7.0	1.87
8	16.8	62.1	4.7	4.6	10.5	4.22
9	21.6	9.38	4.8	5.1	7.0	4.66
10	-	6.1	4.5	3.9	10.5	5.24

Table 3. Summary of source mechanisms fitted for three Anza events in the same magnitude range of 4 to 5.

Event				Depth	Dip	Rake	Strike
Date	Time	Latitude(N)	Longitude(W)				
760811	15:24:55.42	33° 28.9'	-116° 30.62'	14.0	70°	-86°	45°
780605	16:03:03.72	33° 25.21'	-116° 41.61'	14.0	70°	-90°	152°
790212	04:48:42.26	33° 27.21'	-116° 25.44'	5.0	81°	0°	145°

•Depths are given in km. Strikes are measured clockwise from North.

Table 4. Summary of source mechanisms fitted for aftershocks of the 1942, 54, 68 Borrego Mountain and 1969 Coyote Mountain earthquakes.

Event					Dip	Rake	Strike
Date	Hrmn	Sec	Latitude(N)	Longitude(W)			
Oct 29,1942	1621	57.9	32° 58.0'	-116° 00.0'	80°	251°	163°
Oct 30,1942	0535	45.0	32° 58.0'	-116° 00.0'	70°	-86°	56°
Mar 23,1954	0414	50.0	33° 17.0'	-116° 11.0'	80°	251°	163°
Apr 9,1968	0800	38.5	33° 06.4'	-116° 00.4'	45°	90°	0°
Apr 9,1968	1831	38.5	33° 18.9'	-116° 18.3'	80°	251°	163°
May 19,1969	1440	33.0	33° 20.9'	-116° 11.3'	80°	251°	163°

*Depths of these events are all modeled at 8 km, except for one of the 1942 aftershocks (0535) which was modeled at 12 km depth. Strikes are measured clockwise from North.

CONTRACTORS (United States)

Professor Keiiti Aki
Center for Earth Sciences
University of Southern California
University Park
Los Angeles, CA 90089-0741

Professor Charles B. Archambeau
Cooperative Institute for Resch
in Environmental Sciences
University of Colorado
Boulder, CO 80309

Dr. Thomas C. Bache Jr.
Science Applications Int'l Corp.
10210 Campus Point Drive
San Diego, CA 92121 (2 copies)

Dr. Douglas R. Baumgardt
Signal Analysis & Systems Div.
ENSCO, Inc.
5400 Port Royal Road
Springfield, VA 22151-2388

Dr. S. Bratt
Science Applications Int'l Corp.
10210 Campus Point Drive
San Diego, CA 92121

Dr. Lawrence J. Burdick
Woodward-Clyde Consultants
P.O. Box 93245
Pasadena, CA 91109-3245 (2 copies)

Professor Robert W. Clayton
Seismological Laboratory/Div. of
Geological & Planetary Sciences
California Institute of Technology
Pasadena, CA 91125

Dr. Vernon F. Cormier
Department of Geology & Geophysics
U-45, Room 207
The University of Connecticut
Storrs, Connecticut 06268

Dr. Zoltan A. Der
ENSCO, Inc.
5400 Port Royal Road
Springfield, VA 22151-2388

Professor John Ferguson
Center for Lithospheric Studies
The University of Texas at Dallas
P.O. Box 830688
Richardson, TX 75083-0688

Professor Stanley Flatte'
Applied Sciences Building
University of California, Santa Cruz
Santa Cruz, CA 95064

Professor Steven Grand
Department of Geology
245 Natural History Building
1301 West Green Street
Urbana, IL 61801

Professor Roy Greenfield
Geosciences Department
403 Deike Building
The Pennsylvania State University
University Park, PA 16802

Professor David G. Harkrider
Seismological Laboratory
Div of Geological & Planetary Sciences
California Institute of Technology
Pasadena, CA 91125

Professor Donald V. Helmberger
Seismological Laboratory
Div of Geological & Planetary Sciences
California Institute of Technology
Pasadena, CA 91125

Professor Eugene Herrin
Institute for the Study of Earth
& Man/Geophysical Laboratory
Southern Methodist University
Dallas, TX 75275

Professor Robert B. Herrmann
Department of Earth & Atmospheric
Sciences
Saint Louis University
Saint Louis, MO 63156

Professor Lane R. Johnson
Seismographic Station
University of California
Berkeley, CA 94720

Professor Thomas H. Jordan
Department of Earth, Atmospheric
and Planetary Sciences
Mass Institute of Technology
Cambridge, MA 02139

Dr. Alan Kafka
Department of Geology &
Geophysics
Boston College
Chestnut Hill, MA 02167

Professor Leon Knopoff
University of California
Institute of Geophysics
& Planetary Physics
Los Angeles, CA 90024

Professor Charles A. Langston
Geosciences Department
403 Deike Building
The Pennsylvania State University
University Park, PA 16802

Professor Thorne Lay
Department of Geological Sciences
1006 C.C. Little Building
University of Michigan
Ann Harbor, MI 48109-1063

Dr. Randolph Martin III
New England Research, Inc.
P.O. Box 857
Norwich, VT 05055

Dr. Gary McCartor
Mission Research Corp.
735 State Street
P.O. Drawer 719
Santa Barbara, CA 93102 (2 copies)

Professor Thomas V. McEvilly
Seismographic Station
University of California
Berkeley, CA 94720

Dr. Keith L. McLaughlin
S-CUBED,
A Division of Maxwell Laboratory
P.O. Box 1620
La Jolla, CA 92038-1620

Professor William Menke
Lamont-Doherty Geological Observatory
of Columbia University
Palisades, NY 10964

Professor Brian J. Mitchell
Department of Earth & Atmospheric
Sciences
Saint Louis University
Saint Louis, MO 63156

Mr. Jack Murphy
S-CUBED
A Division of Maxwell Laboratory
11800 Sunrise Valley Drive
Suite 1212
Reston, VA 22091 (2 copies)

Professor J. A. Orcutt
Institute of Geophysics and Planetary
Physics, A-205
Scripps Institute of Oceanography
Univ. of California, San Diego
La Jolla, CA 92093

Professor Keith Priestley
University of Nevada
Mackay School of Mines
Reno, NV 89557

Wilmer Rivers
Teledyne Geotech
314 Montgomery Street
Alexandria, VA 22314

Professor Charles G. Sammis
Center for Earth Sciences
University of Southern California
University Park
Los Angeles, CA 90089-0741

Dr. Jeffrey L. Stevens
S-CUBED,
A Division of Maxwell Laboratory
P.O. Box 1620
La Jolla, CA 92038-1620

Professor Brian Stump
Institute for the Study of Earth & Man
Geophysical Laboratory
Southern Methodist University
Dallas, TX 75275

Professor Ta-liang Teng
Center for Earth Sciences
University of Southern California
University Park
Los Angeles, CA 90089-0741

Professor M. Nafi Toksoz
Earth Resources Lab
Dept of Earth, Atmospheric and
Planetary Sciences
Massachusetts Institute of Technology
42 Carleton Street
Cambridge, MA 02142

Professor Terry C. Wallace
Department of Geosciences
Building #11
University of Arizona
Tucson, AZ 85721

Weidlinger Associates
ATTN: Dr. Gregory Wojcik
620 Hansen Way, Suite 100
Palo Alto, CA 94304

Professor Francis T. Wu
Department of Geological Sciences
State University of new York
At Binghamton
Vestal, NY 13901

OTHERS (United States)

Dr. Monem Abdel-Gawad
Rockwell Internat'l Science Center
1049 Camino Dos Rios
Thousand Oaks, CA 91360

Professor Shelton S. Alexander
Geosciences Department
403 Deike Building
The Pennsylvania State University
University Park, PA 16802

Dr. Ralph Archuleta
Department of Geological Sciences
Univ. of California at Santa Barbara
Santa Barbara, CA

Dr. Muawia Barazangi
Geological Sciences
Cornell University
Ithaca, NY 14853

J. Barker
Department of Geological Sciences
State University of New York at Binghamton
Vestal, NY 13901

Mr. William J. Best
907 Westwood Drive
Vienna, VA 22180

Dr. N. Biswas
Geophysical Institute
University of Alaska
Fairbanks, AK 99701

Dr. G. A. Bollinger
Department of Geological Sciences
Virginia Polytechnical Institute
21044 Derring Hall
Blacksburg, VA 24061

Dr. James Bulau
Rockwell Int'l Science Center
1049 Camino Dos Rios
P.O. Box 1085
Thousand Oaks, CA 91360

Mr. Roy Burger
1221 Serry Rd.
Schenectady, NY 12309

Dr. Robert Burridge
Schlumberger-Doll Resch Ctr.
Old Quarry Road
Ridgefield, CT 06877

Science Horizons, Inc.
ATTN: Dr. Theodore Cherry
710 Encinitas Blvd., Suite 101
Encinitas, CA 92024 (2 copies)

Professor Jon F. Claerbout
Professor Amos Nur
Dept. of Geophysics
Stanford University
Stanford, CA 94305 (2 copies)

Dr. Anton W. Dainty
AFGL/LWH
Hanscom AFB, MA 01731

Dr. Steven Day
Dept. of Geological Sciences
San Diego State U.
San Diego, CA 92182

Professor Adam Dziewonski
Hoffman Laboratory
Harvard University
20 Oxford St.
Cambridge, MA 02138

Professor John Ebel
Dept of Geology & Geophysics
Boston College
Chestnut Hill, MA 02167

Dr. Alexander Florence
SRI International
333 Ravenswood Avenue
Menlo Park, CA 94025-3493

Dr. Donald Forsyth
Dept. of Geological Sciences
Brown University
Providence, RI 02912

Dr. Anthony Gangi
Texas A&M University
Department of Geophysics
College Station, TX 77843

Dr. Freeman Gilbert
Institute of Geophysics & Planetary Physics
Univ. of California, San Diego
P.O. Box 109
La Jolla, CA 92037

Mr. Edward Giller
Pacific Seirra Research Corp.
1401 Wilson Boulevard
Arlington, VA 22209

Dr. Jeffrey W. Given
Sierra Geophysics
11255 Kirkland Way
Kirkland, WA 98033

Dr. Henry L. Gray
Associate Dean of Dedman College
Department of Statistical Sciences
Southern Methodist University
Dallas, TX 75275

Rong Song Jih
Teledyne Geotech
314 Montgomery Street
Alexandria, Virginia 22314

Professor F.K. Lamb
University of Illinois at
Urbana-Champaign
Department of Physics
1110 West Green Street
Urbana, IL 61801

Dr. Arthur Lerner-Lam
Lamont-Doherty Geological Observatory
of Columbia University
Palisades, NY 10964

Dr. L. Timothy Long
School of Geophysical Sciences
Georgia Institute of Technology
Atlanta, GA 30332

Dr. Peter Malin
University of California at Santa Barbara
Institute for Central Studies
Santa Barbara, CA 93106

Dr. George R. Mellman
Sierra Geophysics
11255 Kirkland Way
Kirkland, WA 98033

Dr. Bernard Minster
Institute of Geophysics and Planetary
Physics, A-205
Scripps Institute of Oceanography
Univ. of California, San Diego
La Jolla, CA 92093

Professor John Nabelek
College of Oceanography
Oregon State University
Corvallis, OR 97331

Dr. Geza Nagy
U. California, San Diego
Dept of Ames, M.S. B-010
La Jolla, CA 92093

Dr. Jack Oliver
Department of Geology
Cornell University
Ithaca, NY 14850

Dr. Robert Phinney/Dr. F.A. Dahlen
Dept of Geological
Geophysical Sci. University
Princeton University
Princeton, NJ 08540 (2 copies)

RADIX Systems, Inc.
Attn: Dr. Jay Pulli
2 Taft Court, Suite 203
Rockville, Maryland 20850

Professor Paul G. Richards
Lamont-Doherty Geological
Observatory of Columbia Univ.
Palisades, NY 10964

Dr. Norton Rimer
S-CUBED
A Division of Maxwell Laboratory
P.O. 1620
La Jolla, CA 92038-1620

Professor Larry J. Ruff
Department of Geological Sciences
1006 C.C. Little Building
University of Michigan
Ann Arbor, MI 48109-1063

Dr. Alan S. Ryall, Jr.
Center of Seismic Studies
1300 North 17th Street
Suite 1450
Arlington, VA 22209-2308 (4 copies)

Dr. Richard Sailor
TASC Inc.
55 Walkers Brook Drive
Reading, MA 01867

Thomas J. Sereno, Jr.
Service Application Int'l Corp.
10210 Campus Point Drive
San Diego, CA 92121

Dr. David G. Simpson
Lamont-Doherty Geological Observ.
of Columbia University
Palisades, NY 10964

Dr. Bob Smith
Department of Geophysics
University of Utah
1400 East 2nd South
Salt Lake City, UT 84112

Dr. S. W. Smith
Geophysics Program
University of Washington
Seattle, WA 98195

Dr. Stewart Smith
IRIS Inc.
1616 N. Fort Myer Drive
Suite 1440
Arlington, VA 22209

Rondout Associates
ATTN: Dr. George Sutton,
Dr. Jerry Carter, Dr. Paul Pomeroy
P.O. Box 224
Stone Ridge, NY 12484 (4 copies)

Dr. L. Sykes
Lamont Doherty Geological Observ.
Columbia University
Palisades, NY 10964

Dr. Pradeep Talwani
Department of Geological Sciences
University of South Carolina
Columbia, SC 29208

Dr. R. B. Tittmann
Rockwell International Science Center
1049 Camino Dos Rios
P.O. Box 1085
Thousand Oaks, CA 91360

Professor John H. Woodhouse
Hoffman Laboratory
Harvard University
20 Oxford St.
Cambridge, MA 02138

Dr. Gregory B. Young
ENSCO, Inc.
5400 Port Royal Road
Springfield, VA 22151-2388

OTHERS (FOREIGN)

Dr. Peter Basham
Earth Physics Branch
Geological Survey of Canada
1 Observatory Crescent
Ottawa, Ontario
CANADA K1A 0Y3

Dr. Eduard Berg
Institute of Geophysics
University of Hawaii
Honolulu, HI 96822

Dr. Michel Bouchon - Universite
Scientifique et Medicale de Grenob
Lab de Geophysique - Interne et
Tectonophysique - I.R.I.G.M-B.P.
38402 St. Martin D'Heres
Cedex FRANCE

Dr. Hilmar Bungum/NTNF/NORSAR
P.O. Box 51
Norwegian Council of Science,
Industry and Research, NORSAR
N-2007 Kjeller, NORWAY

Dr. Michel Campillo
I.R.I.G.M.-B.P. 68
38402 St. Martin D'Heres
Cedex, FRANCE

Dr. Kin-Yip Chun
Geophysics Division
Physics Department
University of Toronto
Ontario, CANADA M5S 1A7

Dr. Alan Douglas
Ministry of Defense
Blacknest, Brimpton,
Reading RG7-4RS
UNITED KINGDOM

Dr. Manfred Henger
Fed. Inst. For Geosciences & Nat'l Res.
Postfach 510153
D-3000 Hannover 51
FEDERAL REPUBLIC OF GERMANY

Dr. E. Husebye
NTNF/NORSAR
P.O. Box 51
N-2007 Kjeller, NORWAY

Ms. Eva Johannisson
Senior Research Officer
National Defense Research Inst.
P.O. Box 27322
S-102 54 Stockholm
SWEDEN

Tormod Kvaerna
NTNF/NORSAR
P.O. Box 51
N-2007 Kjeller, NORWAY

Mr. Peter Marshall, Procurement
Executive, Ministry of Defense
Blacknest, Brimpton,
Reading FG7-4RS
UNITED KINGDOM (3 copies)

Dr. Ben Menaheim
Weizman Institute of Science
Rehovot, ISRAEL 951729

Dr. Svein Mykkeltveit
NTNF/NORSAR
P.O. Box 51
N-2007 Kjeller, NORWAY (3 copies)

Dr. Robert North
Geophysics Division
Geological Survey of Canada
1 Observatory crescent
Ottawa, Ontario
CANADA, K1A 0Y3

Dr. Frode Ringdal
NTNF/NORSAR
P.O. Box 51
N-2007 Kjeller, NORWAY

Dr. Jorg Schlittenhardt
Federal Inst. for Geosciences & Nat'l Res.
Postfach 510153
D-3000 Hannover 51
FEDERAL REPUBLIC OF GERMANY

University of Hawaii
Institute of Geophysics
ATTN: Dr. Daniel Walker
Honolulu, HI 96822

FOREIGN CONTRACTORS

Dr. Ramon Cabre, S.J.
c/o Mr. Ralph Buck
Economic Consular
American Embassy
APO Miami, Florida 34032

Professor Peter Harjes
Institute for Geophysik
Ruhr University/Bochum
P.O. Box 102148 4630 Bochum 1
FEDERAL REPUBLIC OF GERMANY

Professor Brian L.N. Kennett
Research School of Earth Sciences
Institute of Advanced Studies
G.P.O. Box 4
Canberra 2601
AUSTRALIA

Dr. B. Massinon
Societe Radiomana
27, Rue Claude Bernard
75005, Paris, FRANCE (2 copies)

Dr. Pierre Mechler
Societe Radiomana
27, Rue Claude Bernard
75005 Paris, FRANCE

Dr. Ralph Alewine III
DARPA/NMRO
1400 Wilson Boulevard
Arlington, VA 22209-2308

Dr. Peter Basham
Geological Survey of Canada
1 Observatory Creseut
Ottowa, Ontario
CANADA K1A 0Y3

Dr. Robert Blandford
DARPA/NMRO
1400 Wilson Boulevard
Arlington, VA 22209-2308

Sandia National Laboratory
ATTN: Dr. H. B. Durham
Albuquerque, NM 87185

Dr. Jack Evernden
USGS-Earthquake Studies
345 Middlefield Road
Menlo Park, CA 94025

U.S. Geological Survey
ATTN. Dr. T. Hanks
Nat'l Earthquake Resch Center
345 Middlefield Road
Menlo Park, CA 94025

Dr. James Hannon
Lawrence Livermore Nat'l Lab.
P.O. Box 808
Livermore, CA 94550

U.S. Arms Control & Disarm. Agency
ATTN: Dick Morrow
Washington, D.C. 20451

Paul Johnson
ESS-4, Mail Stop J979
Los Alamos National Laboratory
Los Alamos, NM 87545

Ms. Ann Kerr
DARPA/NMRO
1400 Wilson Boulevard
Arlington, VA 22209-2308

Dr. Max Koontz
US Dept of Energy/DP 331
Forrestal Building
1000 Independence Ave.
Washington, D.C. 20585

Dr. W. H. K. Lee
USGS
Office of Earthquakes, Volcanoes,
& Engineering
Branch of Seismology
345 Middlefield Rd
Menlo Park, CA 94025

Dr. William Leith
USGS
Mail Stop 928
Reston, VA 22092

Dr. Richard Lewis
Dir. Earthquake Engineering and
Geophysics
U.S. Army Corps of Engineers
Box 631
Vicksburg, MS 39180

Dr. Robert Masse'
Box 25046, Mail Stop 967
Denver Federal Center
Denver, Colorado 80225

R. Morrow
ACDA/VI
Room 5741
320 21st Street N.W.
Washington, D.C. 20451

Dr. Keith K. Nakanishi
Lawrence Livermore National Laboratory
P.O. Box 808, L-205
Livermore, CA 94550 (2 copies)

Dr. Carl Newton
Los Alamos National Lab.
P.O. Box 1663
Mail Stop C335, Group E553
Los Alamos, NM 87545

Dr. Kenneth H. Olsen
Los Alamos Scientific Lab.
Post Office Box 1663
Los Alamos, NM 87545

Howard J. Patton
Lawrence Livermore National Laboratory
P.O. Box 808, L-205
Livermore, CA 94550

Mr. Chris Paine
Office of Senator Kennedy
SR 315
United States Senate
Washington, D.C. 20510

AFOSR/NP
ATTN: Colonel Jerry J. Perrizo
Bldg 410
Bolling AFB, Wash D.C. 20332-6448

HQ AFTAC/TT
Attn: Dr. Frank F. Pilotte
Patrick AFB, Florida 32925-6001

Mr. Jack Rachlin
USGS - Geology, Rm 3 C136
Mail Stop 928 National Center
Reston, VA 22092

Robert Reinke
AFWL/NTESG
Kirtland AFB, NM 87117-6008

HQ AFTAC/TGR
Attn: Dr. George H. Rothe
Patrick AFB, Florida 32925-6001

Donald L. Springer
Lawrence Livermore National Laboratory
P.O. Box 808, L-205
Livermore, CA 94550

Dr. Lawrence Turnbull
OSWR/NED
Central Intelligence Agency
CIA, Room 5G48
Washington, D.C. 20505

Dr. Thomas Weaver
Los Alamos Scientific Laboratory
Los Almos, NM 97544

AFGL/SULL
Research Library
Hanscom AFB, MA 01731-5000 (2 copies)

Secretary of the Air Force (SAFRD)
Washington, DC 20330
Office of the Secretary Defense
DDR & E
Washington, DC 20330

HQ DNA
ATTN: Technical Library
Washington, DC 20305

Director, Technical Information
DARPA
1400 Wilson Blvd.
Arlington, VA 22209

AFGL/XO
Hanscom AFB, MA 01731-5000

AFGL/LW
Hanscom AFB, MA 01731-5000

DARPA/PM
1400 Wilson Boulevard
Arlington, VA 22209

Defense Technical
Information Center
Cameron Station
Alexandria, VA 22314
(5 copies)

Defense Intelligence Agency
Directorate for Scientific &
Technical Intelligence
Washington, D.C. 20301

Defense Nuclear Agency/SPSS
ATTN: Dr. Michael Shore
6801 Telegraph Road
Alexandria, VA 22310

AFTAC/CA (STINFO)
Patrick AFB, FL 32925-6001

Dr. Gregory van der Vink
Congress of the United States
Office of Technology Assessment
Washington, D.C. 20510